University of Stavanger

**Faculty of Science and Technology**

# MASTER'S THESIS

| | |
|---|---|
| Study program/Specialization:<br><br>Petroleum Geosciences Engineering | Spring, 2018<br><br>Open |
| Author:<br><br>Mathias Tomasgaard | |

Faculty supervisor: Nestor Cardozo

External supervisor: Lothar Schulte

Title of thesis:

Time dependent signal of a chalk field: The South Arne Field, Danish North Sea

Credits (ECTS): 30

| | |
|---|---|
| Keywords:<br><br>Time-lapse seismic<br>Rock physics<br>Reservoir compaction<br>Fault reactivation<br>AVO<br>Coloured inversion | Pages: 105<br><br>Stavanger, June 5, 2018 |

# Time dependent signal of a chalk field: The South Arne Field, Danish North Sea

by

Mathias Tomasgaard

MSc Thesis

Presented to the Faculty of Science and Technology

University of Stavanger

2018

# Acknowledgements

We are very grateful to Schlumberger for providing the software Petrel, and to Aker BP for the dataset.

I would like to thank my first supervisor Lothar Schulte for excellent guidance through various challenges that I encountered during this thesis. I am also grateful to my second supervisor, Nestor Cardozo, for proofreading and pointing out conflicting arguments. In addition, I would like to thank fellow students for valuable discussions on numerous topics.

I appreciate the support from family and friends, helping me to relax while working on this thesis. A special thanks to my girlfriend, for her outstanding support and patience!

# *Time dependent signal of a chalk field: The South Arne Field, Danish North Sea*

Mathias Tomasgaard[1], Nestor Cardozo[1], Lothar Schulte[2]

1: Department of Energy Resources, University of Stavanger, 4036 Stavanger, Norway
2: Schlumberger SIS, Risabergveien 3, 4068 Stavanger, Norway

## Abstract

Time-lapse seismic analysis is applied to a producing chalk field, with the aim to understand the field time-varying behaviour with respect to reservoir structure and fluid migration. The study area is the South Arne field in the Danish Central Graben (North Sea). The field lies in an elongated anticline, and the reservoir consists of fractured chalk of the Tor and Ekofisk formations. The reservoir is highly heterogeneous, with varying reservoir quality (i.e., porosity and water saturation).

The time-lapse study includes the interpretation of rock physics properties in order to explain how and why the seismic response changes with production. The analysis of the reservoir structure is largely based on seismic time-shift data to detect reservoir compaction, and difference in amplitude response of faults in order to analyse possible fault reactivation. Seismic amplitudes, AVO (amplitude variation with offset) response, and coloured inversion results are analysed to detect fluid movements.

A significant amount of production-induced compaction is observed for a limited part of the reservoir, which correlates strongly with high porosity and low water saturation, and the location of several production and injection wells. Based on the rock physics analysis, this part of the reservoir is less stiff than the surrounding reservoir formations, which explains why it is subject to compaction. This may also explain the observation that faults in this part of the reservoir are highly reactivated.

The observed changes in seismic response with production time include reduction in amplitudes, decrease in AVO response, and hardening effect from the coloured inversion. These effects are caused by changes in fluid saturation and by compaction. The changes in seismic response are strongly correlated with the compaction, which indicates that the time-lapse seismic response is more sensitive to the reduction in porosity caused by compaction than to fluid changes. This is supported by the well data, which show that the acoustic impedance of the reservoirs is more influenced by porosity than water saturation. Nevertheless, based on the hardening effects, the oil accumulations seem to be separated by partially sealing faults, causing the fluids to move differentially for the different fault blocks.

# Table of contents

# List of tables

# List of figures

# 1. Introduction

Time-lapse seismic, or 4D seismic, is 3D seismic acquired at different times. It is typically used for reservoir monitoring, based on the fact that acoustic impedance is dependent on fluid saturation, pressure, and temperature. Consequently, changes in these properties should influence the seismic data, allowing to interpret the effect of hydrocarbon production and fluid movement within the reservoir.

The structure of a reservoir is often affected by hydrocarbon production, and these changes should be detectable with the help of time-lapse seismic data. Typical effects are reservoir compaction and fault reactivation. These changes could influence the performance of the reservoir, and it is therefore crucial to understand the mechanisms causing this behaviour.

Rock physics creates the bridge between geology and geophysical data, and it provides detailed information about several properties of the reservoir rocks. By studying rock physics together with seismic data, it is possible to interpret variations in the reservoir rocks (e.g., lithology, porosity, and fluid saturation) based on vertical and lateral changes in the seismic signal. When conducting time-lapse studies, rock physics helps gaining a deeper understanding of how hydrocarbon production affects the reservoir.

AVO (amplitude variations with offset) describes how seismic amplitudes vary with offset (i.e., distance between source and receiver), and this analysis may extract crucial information from the seismic data. Hydrocarbon bearing formations have a different AVO response than water saturated rocks. Based on this, AVO can be used to delineate the hydrocarbon zones in a reservoir and identify fluid contacts. Combining AVO techniques with time-lapse seismic is thus helpful in identifying fluid movement.

Seismic inversion is the process of transforming seismic data representing acoustic contrasts between different layers to actual properties of the layers. Seismic data have relatively low resolution, and lack low and high frequencies. Thus, seismic data do not provide the detailed information that is available in well data. Seismic inversion combines seismic and well data to obtain accurate impedance values of the subsurface.

## 1.1 Objectives

The main aim of this study is to detect, describe, and understand the time-varying behaviour of a producing reservoir. This objective can be further subdivided into two questions. The first question is: *What is controlling the reservoir compaction and possible fault reactivation?* To answer this question, the changes in elevation of key seismic reflectors between the different surveys is considered together with changes in continuity of seismic reflectors. The second question is: *How do the fluids migrate within the reservoir and what is controlling this movement?* This is investigated by studying changes in seismic amplitudes between the different seismic surveys.

## 1.2 Study area

The study area is the South Arne oil field, located in the Central Graben in the North Sea (Figure 1.1). More specifically, it is located in the Danish Central Graben, which is bound to the northeast by the Ringkøbing-Fryn High, to the northwest by the border between Denmark and Norway, and to the southwest by the borders between Denmark and the United Kingdom and between Denmark and Germany.

The South Arne field was discovered in 1969, and production started in 1999. It is producing with several horizontal production and water injector wells. The field consists of a chalk reservoir and is located in an anticline, measuring 12 km by 3 km (Christensen et al., 2006; Garcia and MacBeth, 2013; Lüthje et al., 2013). It lies in the Arne-Elin Graben, just south of the North-Arne field, which is located in a salt structure.

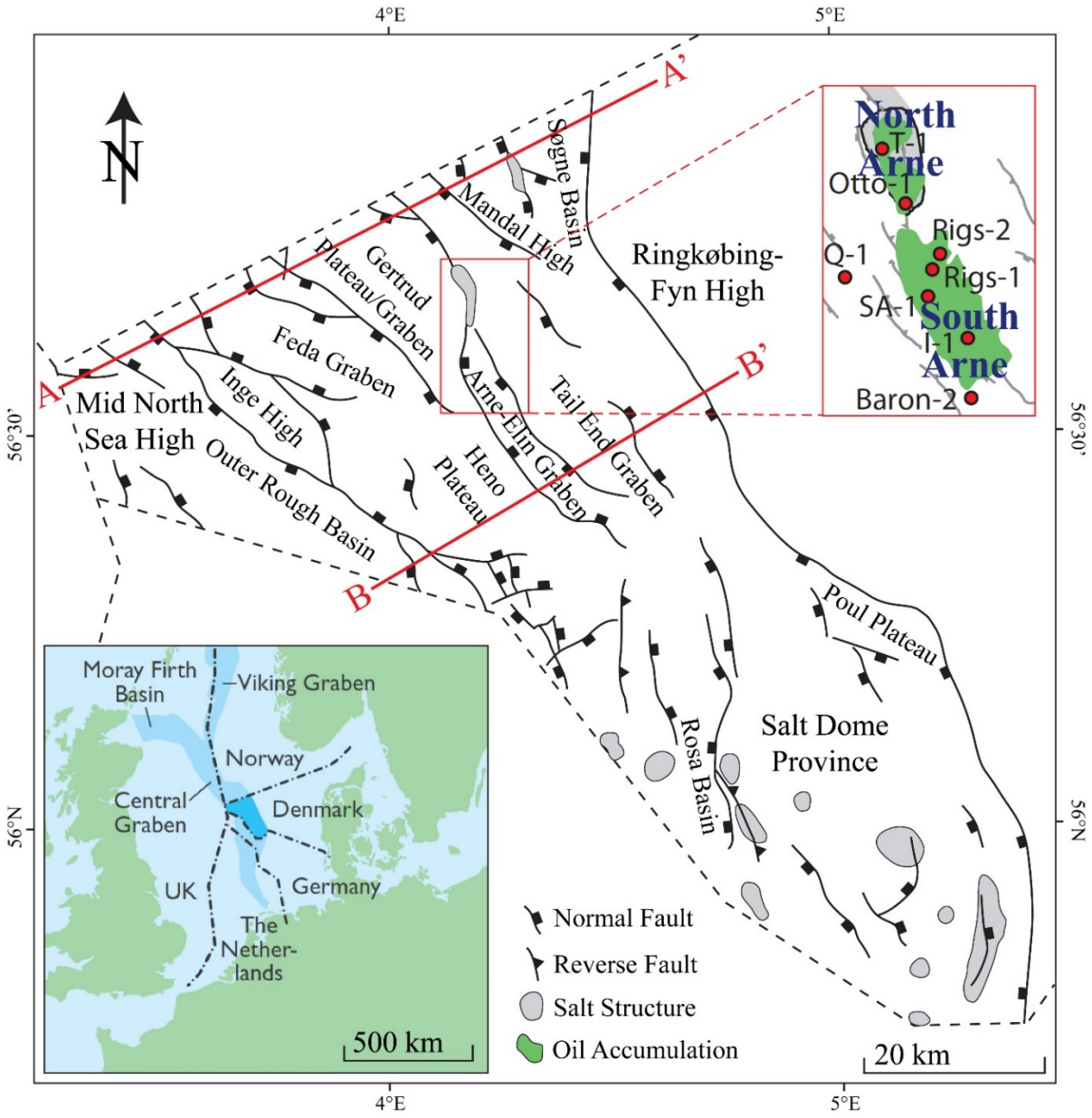


***Figure 1.1**: The study area is the South Arne field, located in the Danish Central Graben. Modified after Andsbjerg and Dybkjaer (2003) and Lindgreen et al. (2012).*

# 2. Geological setting

This chapter gives a brief discussion on the regional geology and the geology of the South Arne field, including previous work done on the field.

## 2.1 Regional geology and structural evolution

The North Sea has a relatively complex geological history, which has caused the development of different tectonic provinces and sedimentary basins (Figure 1.1 and Figure 2.1). The evolution of the North Sea can be divided into five main events, comprising the Caledonian geosyncline during the Cambrian-Silurian; the Variscan geosyncline during the Devonian-Carboniferous; an intracratonic stage during the Permian-Triassic; rifting during the Jurassic-Cretaceous; and post-rifting during the Cenozoic (Ziegler, 1975).

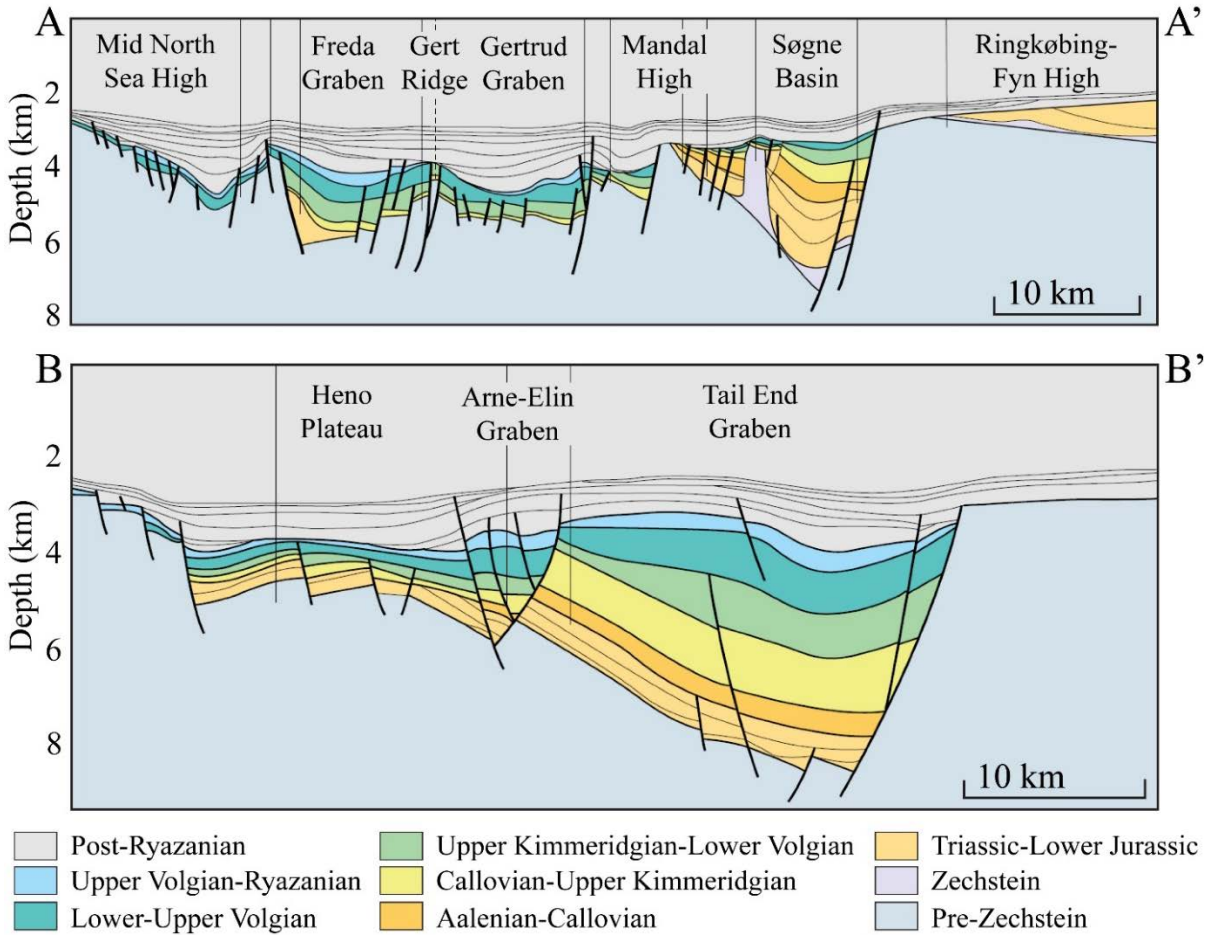


***Figure 2.1**: Cross-sections demonstrating the geology of the northern part of the Danish Central Graben. Locations of the sections are shown in Figure 1.1. Modified after Møller and Rasmussen (2003).*

### 2.1.1 Carboniferous-Permian

During the Carboniferous-Permian, the North Sea was influenced by major rifting events and extensive volcanism. The extension caused the deposition of reddish eolian and fluvial sandstones of the Rotliegend Gp (Figure 2.2) (Halland et al., 2011). Two main basins were established, and thick evaporate layers of the Zechstein Gp were deposited during sea-level lowstands.

### 2.1.2 Triassic

The extension continued and became more dominant in the Triassic, with major N-S and NE-SW rifting. During this period, coarse fluvial sediments were deposited along the margins of the basin, and finer-grained fluvial and lake sediments were deposited towards the centre of the basin (Halland et al., 2011). Towards the end of the Triassic, and extensive marine transgression occurred.

### 2.1.3 Jurassic

The Jurassic was highly influenced by the appearance of a volcanic dome at the triple junction between the Central Graben, the Viking Graben, and the Moray Firth Basin. Uplift and erosion was caused by the growth of the dome and was followed by rifting (Halland et al., 2011). This event is also believed to be responsible for the deltaic systems causing the deposition of sand, shale, and coal. These deltaic deposits are observed in the Brent Gp (northern North Sea and Horda platform) and the Vestland Gp (Norwegian-Danish Basin and Stord Basin).

A very important extensional phase occurred during the Late Jurassic-Early Cretaceous. This event is associated with major faulting, causing the rotated fault blocks typically observed in the North Sea (Figure 2.1) (Halland et al., 2011). The block faulting caused local uplift which resulted in severe erosion and sediment supply. Thick sequences of shale were deposited in this period, and when this deposition occurred in restricted basins, the shales developed to become the very important source rocks of the Draupne and Mandal fms.

### 2.1.4 Cretaceous

After major rifting during the Late Jurassic-Early Cretaceous, the North Sea was affected by thermal subsidence. Chalk layers of the Hod and Tor fms were deposited in the south, and deposition to the north was dominated by shaly, siliciclastic lithologies (Halland et al., 2011).

### 2.1.5 Cenozoic

The deposition of chalk continued until Early Paleogene, now as the Ekofisk Fm. Inversion tectonics affected the North Sea during the Cenozoic, and this caused the uplift of the basin margins (Halland et al., 2011). Consequently, submarine fan systems were developed, transporting sandy sediments from the Shetland Platform towards the east. The effect of these fans are sandy intervals within the Rogaland and Hordaland groups.

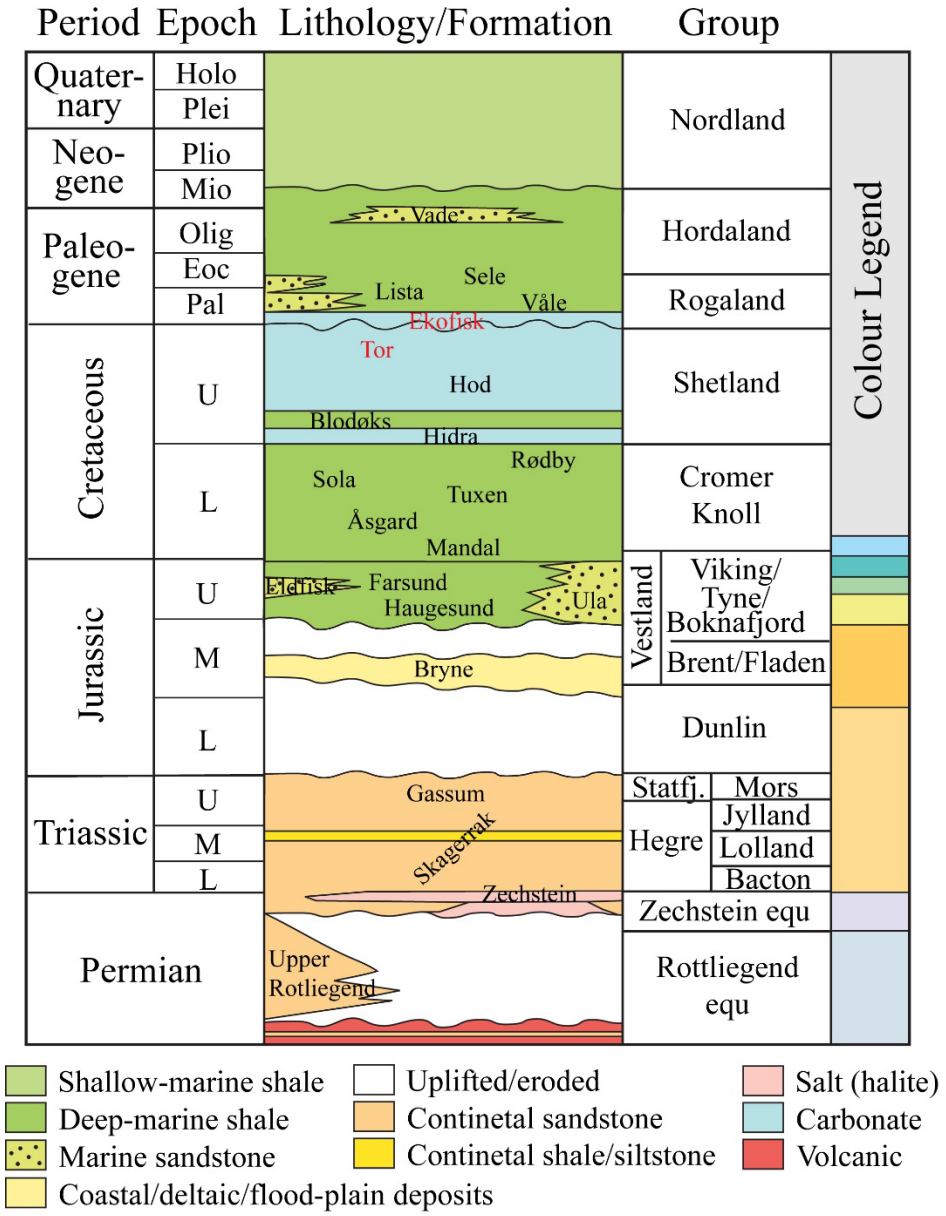


***Figure 2.2**: General stratigraphic column of the southern North Sea. Note the colour legend to the right, making it possible to correlate with the cross-sections in Figure 2.1. Modified after Halland et al. (2011).*

### 2.1.6 Arne-Elin Graben

The South Arne field is located in the Arne-Elin Graben, which has a complex geological evolution (Figure 1.1 and Figure 2.1). It has been interpreted mainly as a NNW-SSE trending transpressional feature and positive flower structures have been identified on seismic data.

The displacement history of the Arne-Elin Graben was investigated by Clausen et al. (1996). They concluded that left lateral movements alternating between transpression and transtension dominated the Late Jurassic-Early Cretaceous, whereas right lateral transpressional movements have been identified during the Late Cretaceous-Paleogene. This means that there was a reversal of the structural evolution from being mainly extensional (i.e., transtension) during the

Late Jurassic-Early Cretaceous to transpressional with opposite lateral displacements during the Late Cretaceous-Paleogene. This change in displacement is related to inversion of the structure, and is responsible for the uplift of the area (Korstgård et al., 1993).

## 2.2 South Arne field

As described above, the South Arne field is located in an elongated anticlinal structure, creating the trap for the hydrocarbon accumulation (Figure 2.3) (Christensen et al., 2006; Garcia and MacBeth, 2013; Lüthje et al., 2013). The anticline is linked to the tectonic inversion that affected the Arne-Elin Graben. A graben-like structure, created by post-depositional faulting, is located in the northern part of the field (Mackertich and Goulding, 1999). The graben strikes in the same direction as the anticline (i.e., NNW-SSE), but a second set of faults striking WNW-ESE also affect the entire field (Herwanger et al., 2010).

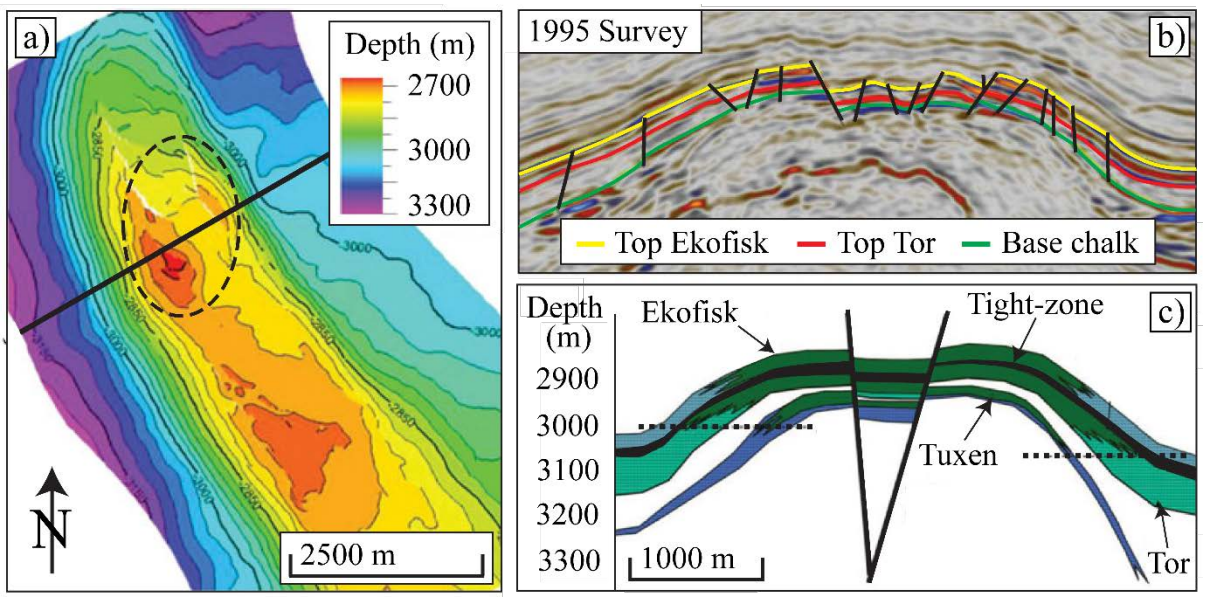


***Figure 2.3**: Structural map of the top reservoir reflector (a), seismic section (b), and schematic cross section of the reservoir (c). Location of the seismic section and the cross section is shown with the black line in a). The dotted lines in c) represent the approximate depths of the oil-water contacts in the Tor Fm. The dotted ellipse in a) illustrates the area of highest reservoir quality. Modified after Garcia and MacBeth (2013).*

The reservoir of the South Arne field consists of Maastrichtian to Danian chalk of the Tor and Ekofisk fms, with the Tuxen Fm acting as a secondary reservoir. The chalk is highly fractured, increasing the porosity and permeability of the reservoirs. The depth of the field is between 2700- 2940 m (Christensen et al., 2006). The Tor and Ekofisk fms are separated by a tight-zone (black band in Figure 2.3c), representing an interval with very low porosity and permeability (Garcia and MacBeth, 2013). Some connectivity between the two formations is present, due to faults and fractures.

The properties of the reservoir rocks are highly varying throughout the field and they correlate strongly with the morphology of the structure (Table 2.1) (Lüthje et al., 2013). The highest quality reservoir rocks are located in the Tor Fm on the crest of northern part of the anticline (Figure 2.3a). This area yields high porosity chalk with high oil saturation, which is partly

explained by overpressure and early hydrocarbon invasion (Vejbæk et al., 2005). Some very thin reservoir layers have been identified on the crest of the structure, and the thickness is generally increasing towards the flanks and away from the structure. Porosity and permeability is, however, decreasing significantly away from the axis of the anticline (Mackertich and Goulding, 1999). The oil-water contact is not at the same elevation over the field. Generally, the oil-water contact lies deeper than the base of the reservoir over the crest of the field, and the oil extends deeper on the eastern flank than on the western flank (Figure 2.3c) (Garcia and MacBeth, 2013).

***Table 2.1**: General reservoir properties. Modified after Lüthje et al. (2013).*

| Reservoir rock | Porosity (%) | Sw (%) | Thickness (m) |
|---|---|---|---|
| Tor Crest | 42-48 | <10 | 0-50 |
| Tor Flank | 15-25 | 25-100 | 50-100 |
| Ekofisk Crest | 30-45 | 10-100 | 25-50 |
| Ekofisk Flank | 15-30 | 50-100 | 50-75 |

### 2.2.1 Previous work

Several studies have been conducted on the South Arne field, and an overview of these studies is given by this section.

Mackertich and Goulding (1999) summarised the exploration and appraisal of the field, and identified the location of the highest reservoir quality as discussed above.

Japsen et al. (2004) and Japsen et al. (2005) showed that the sonic log measures the flushed zone (i.e., the area close to the wellbore, where the reservoir fluids are displaced by the mud filtrate), and cannot be trusted. They suggested that the best procedure to estimate the acoustic properties of the reservoir is to use a modified upper Hashin-Shtrikman model based on porosity and water saturation of the virgin zone (i.e., the area not affected by the mud filtrate).

Vejbæk et al. (2005) discussed the effects of variations in degree of compaction (i.e., different porosities) and fluid content on the seismic response (reflectivity and AVO effect) pre-production. They concluded that the reflectivity can be correlated with the porosity, and that the acoustic impedance is primarily dependent on porosity variations rather than hydrocarbon saturation. Although fluid saturation has an effect on the seismic response, it was established that the sensitivity to fluid changes decreases with increasing compaction. Christensen et al. (2006) showed that seismic inversion for acoustic impedance is able to identify vertical and lateral changes in porosity. They also found that production-induced compaction is mainly controlled by porosity.

Fabricius et al. (2007) discussed how the elastic moduli are influenced by contact-cementation in addition to the porosity. Their study was focused on two wells close to each other (Rigs-1 and Rigs-2). They concluded that Rigs-1 encountered lower porosity due to higher degree of pore-filling cementation and higher water saturation due to high content of smectite.

Time-lapse AVO inversion and rock physics analyses were conducted by Herwanger et al. (2010) to monitor fluid pathways. They identified a heterogeneous sweep of the reservoir,

caused by the water injection. The influence of faults on the drainage pattern was also discussed, and they concluded that the drainage is fault controlled on the SW flank. Time-lapse interpretation was also done by Garcia and MacBeth (2013), who found that a lack of pressure support across faults confirms compartmentalization of the Tor Fm. They also showed that there is a moderate connectivity between the Tor and Ekofisk fms. Lüthje et al. (2013) also concluded that the fluid flow is controlled by faults.

The fault network of the South Arne field was discussed by Astratti et al. (2014), and they found that two fracture sets affect the chalk reservoir, influencing the oil production. These two fracture sets were formed during different times and have the same WNW-ESE orientation. The oldest fracture set was formed during or just after the deposition of the chalk, and it was triggered by the growth of the structure. The youngest fracture set was formed by the continuous oblique inversion of the structure and partial reactivation of pre-existing faults. Astratti et al. (2014) also studied the effect of production on the faults, and they concluded that changes in the seismic fault pattern between the 1995 and 2005 surveys could indicate the development of new faults as well as fault reactivation.

# 3. Theory

Several geophysical methods are applied in this study, and it is crucial to have an understanding of the theoretical concepts behind these methods. In this chapter, the main theories are discussed, with an emphasis on their importance for this study. The actual implementation of these techniques is discussed in chapter 5.

## 3.1 Reservoir behaviour

Several reservoir parameters might change as a hydrocarbon field is producing. The main effects are alterations in fluid saturation, pressure, and temperature, in addition to the structural changes that might occur.

### 3.1.1 Fluid saturation, pressure, and temperature

Perhaps the most obvious effect of hydrocarbon production is that the fluid saturation in the reservoir is altered. Typically, the fluid contacts move upwards as the reservoir is depleted, and the hydrocarbon saturation decreases. Faults and fractures can cause reservoir compartmentalization, where the hydrocarbon accumulation is separated into individual blocks of different fluid contacts and pressures. This complicates the movement of hydrocarbons during production, as the reservoir is unconnected and the hydrocarbons of the different blocks move independently of each other.

The pore pressure in a reservoir is very important for the performance of the field. Figure 3.1 illustrates the typical behaviour of a field with production, and it shows how important the reservoir pressure is for the production rate. As a reservoir is depleted, the pore pressure is decreased. This decrease in reservoir pressure, can also alter the fluid saturation by allowing gas to escape from the solution. The pore pressure in a reservoir can also increase, typically with the help of water injection. The temperature of a reservoir is highly dependent on pressure, and generally, the temperature decreases with pressure decrease.

### 3.1.2 Stress and strain

The structural changes in a reservoir are explained by stress and strain. Consequently, these terms need to be defined before discussing compaction and faulting.

Stress is a symmetric second order tensor consisting of six different tractions. A traction is defined as the ratio of the force applied on a medium to the area on which the force is applied. The stress acting on a plane can always be subdivided into two components – one that is acting perpendicular to the area it is affecting (i.e., normal stress ($\sigma_{ii}$)) and one that is acting parallel to the area (i.e., shear stress ($\sigma_{ij}$)).

Strain represents the changes in shape and dimensions of a medium that is affected by stresses, and it is defined as the relative change in shape and/or size. Strains are also divided into normal strain ($\in_{ii}$) and shear strain ($\in_{ij}$).

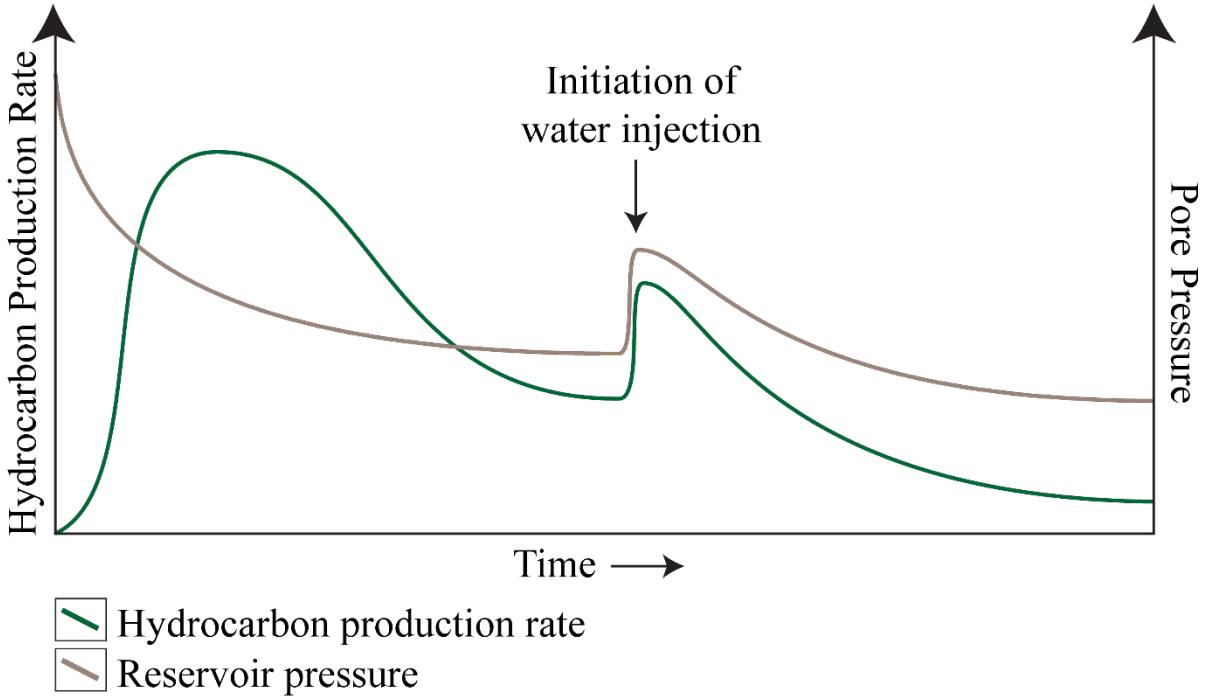


***Figure 3.1**: Schematic representation of a common behaviour of hydrocarbon production rate and reservoir pressure with production time. Note the increase in both production rate and pressure as a secondary oil recovery process is initiated.*

### 3.1.3 Compaction

The structural changes in a producing reservoir are mainly compaction and fault reactivation. Compaction can occur as a result of two different processes: decrease in pore pressure, which can cause compaction due to lack of pressure support, and chemical reactions between the rock matrix and the water that displaces oil, which can weaken the rock framework (Landrø, 2015).

The process of reservoir compaction is illustrated in Figure 3.2 as porosity loss due to changes in pressure. The actual process that leads to compaction is an increase in effective stress (Settari, 2002). Effective stress ($\sigma_{eff}$) is the difference between the applied stress ($\sigma$) and the pore pressure ($P_p$) (i.e., $\sigma_{eff} = \sigma - P_p$). This means that a decrease in pore pressure will increase the effective stress in a reservoir, which may cause compaction.

Note that in Figure 3.2 there is a distinct difference in the slope of the curve corresponding to a change in the type of deformation. The point at which this change occurs corresponds to the pre-consolidation stress (i.e., the maximum effective stress experienced by a rock). This marks where the rock goes from elastic deformation (i.e., the deformation is reversible by unloading) to plastic deformation (i.e., the deformation is permanent and irreversible), and significant compaction occurs (Chan and Zoback, 2002).

The result of reservoir compaction is a reduction in porosity and permeability, and these processes can cause severe operating problems. Another result of reservoir compaction that can affect the field is that the overburden is stretched and, in some cases, the seafloor or land surface can subside. These effects are strongly dependent on the stiffness of the rocks (Landrø, 2015).

Although the effects of reservoir compaction are generally negative for the behaviour of a producing field, compaction has also been recognized to act as an important driving mechanism in some fields, by contributing to maintain the high pressure in the reservoir (Settari, 2002).

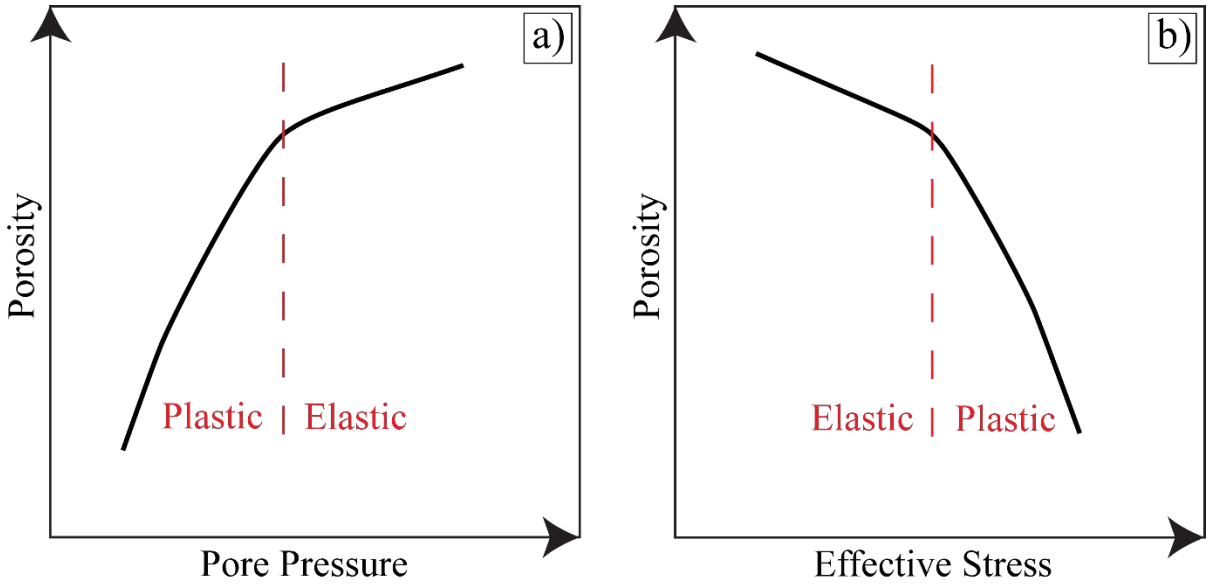


***Figure 3.2**: Porosity (i.e., compaction) as a function of pore pressure (a) and effective stress (b). As the pore pressure of a rock in the elastic regime is decreased, the porosity decreases slowly. It decreases sharply when the rock behaviour changes from elastic to plastic. The point at which this change occurs corresponds to the pre-consolidation stress. This means that significant compaction can occur when the rock responds plastically to the effective stress. Modified after Settari (2002).*

### 3.1.4 Production-induced faulting and fault reactivation

Fault reactivation is a process where slip movement occurs along already existing fault planes. Faults and fractures represent planes of weakness in the rocks. For new faults to form, a large amount of stress build-up is necessary, compared to reactivation of existing faults (Fossen, 2010). Because of this, fault reactivation is more likely to occur than the creation of new faults.

Also for faulting and fault reactivation, the pore pressure plays an important part. Changes in pore pressure alter the stress of the reservoir, and both increase and decrease in pore pressure may induce faulting.

As discussed above, the effective stress is dependent on pore pressure, and an increase in pore pressure will reduce the effective stress. In order to understand why this may cause faulting, the different stress components need to be discussed (Figure 3.3a). In a normal fault regime, the maximum principal stress is the vertical stress ($\sigma_v$), and the minimum principal stress is the minimum horizontal stress ($\sigma_3$). These stress components may further be subdivided into effective normal ($\sigma_n$) and shear stress ($\sigma_s$), acting on the fault plane. These stress components determine if a rock is in a state of active faulting or if it is stable. This is determined by the coefficient of friction ($\mu$), which is given by the amount of shear stress required to have faulting divided by the normal stress acting on the fault plane (i.e., $\mu = \sigma_s/\sigma_n$). The effect of pore pressure is that it counteracts the effective normal stress acting on the fault plane (i.e., increasing the pore pressure causes a reduction in effective normal stress), and if the pore pressure is sufficiently increased, the shear stress might be large enough to cause faulting

(Fossen, 2010). In simpler terms, increasing the pore pressure reduces the normal stress on the fault, which may cause the fault to slip.

The process by which pore pressure reduction can cause faulting is different from the effect of increasing the pore pressure. Intuitively, pore pressure decrease would reduce the probability of faulting, due to the increase in effective normal stress. Nevertheless, faulting may occur as a result of reducing the pore pressure, and this is explained by the effect of pore pressure on the differential stress (i.e., the difference between the maximum and minimum principal stresses, $\sigma_v - \sigma_3$). A pore pressure decrease reduces the minimum horizontal stress; however, the vertical stress is close to unaffected by changes in fluid pressure (Streit and Hillis, 2002). This means that the differential stress is increased by decreasing the pore pressure, and this effect might cause faulting.

Figure 3.3b shows possible stress paths of a reservoir that is produced, causing reduction in pore pressure. The stress paths ($A$) are determined by the relationship between changes in pore pressure ($P_p$) and minimum principal stress ($\sigma_3$) (i.e., $A = \Delta\sigma_3/\Delta P_p$) (Chan and Zoback, 2002). The slope of the failure line (red line) is determined by the coefficient of friction. If $A$ is larger than the slope of the failure line, faulting will occur.

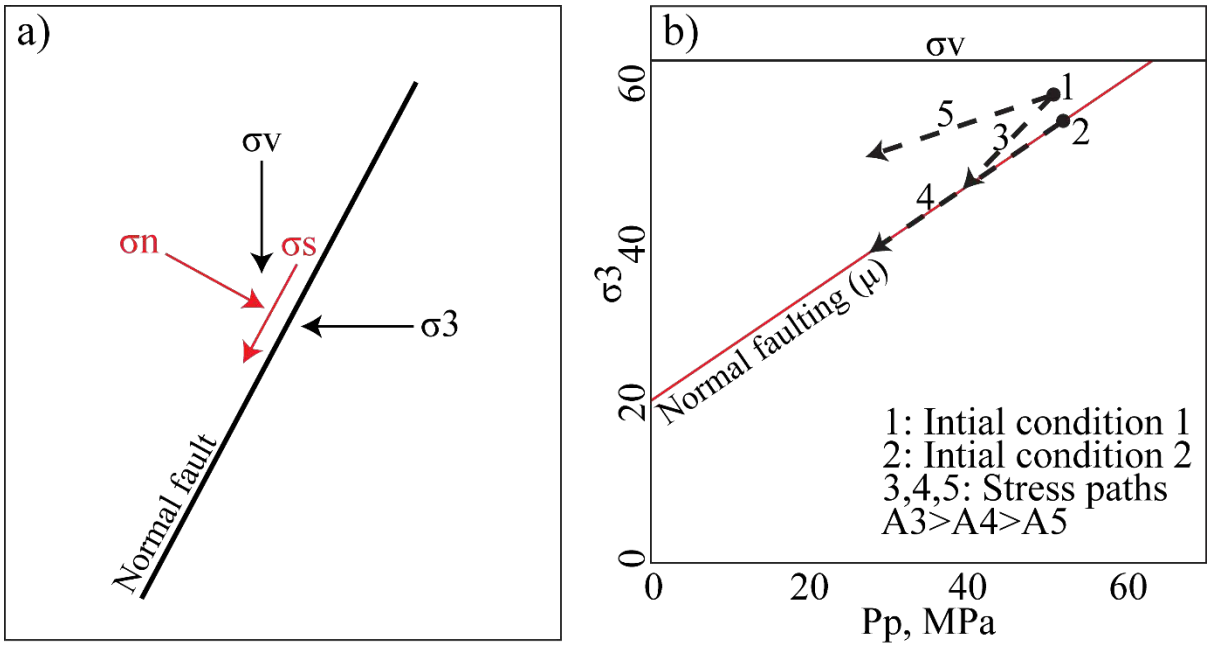


***Figure 3.3**: a) Schematic representation of the different stresses in a normal fault regime – the maximum and minimum horizontal stresses are denoted by $\sigma_v$ and $\sigma_3$, and the effective normal and shear stresses acting on the fault plane are represented as $\sigma_n$ and $\sigma_s$. b) Representation of how the minimum principal stress ($\sigma_3$) reacts to reduction in pore pressure ($P_p$) for different stress paths (i.e., different values of A). The horizontal line represents the vertical stress ($\sigma_v$), which is expected to be unaffected by production. The red line represents the failure line for a given coefficient of friction ($\mu$), where faulting occurs. Two initial reservoir conditions are represented – one where the rocks are in a state of active faulting (2) and another where they are not (1). Modified after Zoback and Zinke (2002).*

The value of $A$ is dependent on the stiffness of the rock. It determines the deformation that occurs as the pore pressure drops – if $A$ is large, faulting is more likely to occur in addition to compaction, and for low values of $A$, compaction will be the dominant mechanism (Chan and Zoback, 2002). This is expressed in Figure 3.3b as different stress paths. Path three has a large

*A* value, and if the reservoir is depleted along this line, normal faulting will eventually happen as the stress path reaches the failure line. If depletion continuous, the reservoir deformation will follow the failure line (i.e., stress path four). For lower values of *A* (e.g., stress path five), the reservoir deformation will move away from the failure line, and faulting will be unlikely.

Note that two different initial reservoir conditions are presented in Figure 3.3b. These different conditions indicate the stress state of different parts of the reservoir in the Valhall field prior to production (Zoback and Zinke, 2002). The crest of the field was initially in a state of active normal faulting (initial condition two), and the flanks were more stable (initial condition one). As the reservoir was produced, the crest of the field followed stress path four, and the flanks followed paths three and four. This indicates that production led to continued faulting on the crest of the field, and faulting was induced by production on the flanks.

## 3.2 Rock physics

Rock physics is used to create the bridge between geology and geophysical data. By applying rock physics, typically based on well data, and comparing with seismic data, a greater understanding of the seismic signal is obtained. Vertical and lateral changes in the seismic signal allows the interpretation of variability in the reservoir rocks (e.g., lithology, porosity, and fluid saturation) by including rock physics.

### 3.2.1 Elastic properties

Elastic properties are measurements of the rock resistance to deformation and are given by different relationships between stresses and strains. High values of the elastic properties indicate that the rock has large stiffness, i.e., large stresses are needed to deform the rock. Figure 3.4 shows a schematic representation of some important elastic properties that are discussed below, and their equations are given in Table 3.1

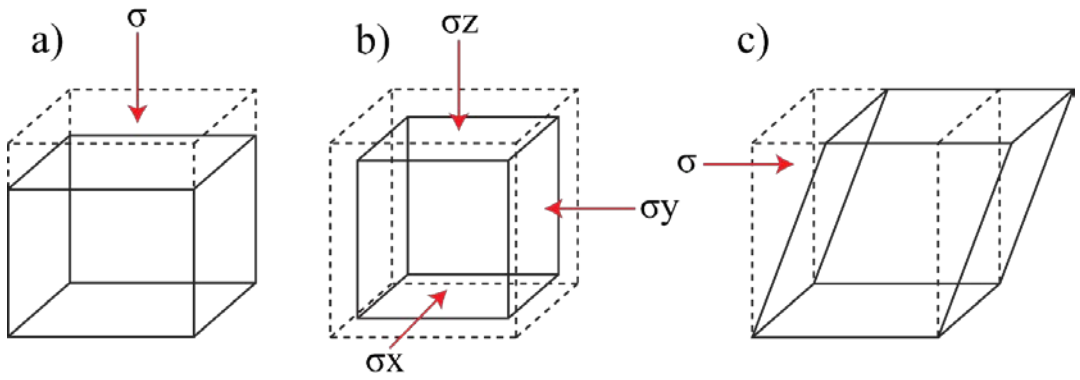


***Figure 3.4**: Elastic properties of rocks are described by their relationship between stress and strain. The red arrows indicate stresses affecting the medium in a xyz coordinate system. The dotted lines illustrate the original size and shape of the medium and the solid lines show how it has been deformed by the stresses. The difference in shape and size of the medium in its original and deformed state represents the strain. The figure demonstrates the main concept of a) Young's modulus, b) bulk modulus, and c) shear modulus.*

Young's modulus ($E$), also called elastic modulus or modulus of elasticity, describes the stress-strain relationship in a unidirectional stress state (i.e., stress in one direction and all other stress components are zero) (Figure 3.4a). This means that it is a measure of the amount of stress compared to amount of strain in the same direction experienced by a rock.

The bulk modulus ($K$), also called incompressibility, is a measure of the relationship between hydrostatic stress ($P = (\sigma_{xx} + \sigma_{yy} + \sigma_{zz})/3$) and volumetric strain ($\epsilon_V = \epsilon_{xx} + \epsilon_{yy} + \epsilon_{zz}$) (Figure 3.4b). In contrast to Young's modulus, it includes stress and strain in all directions, and represents thus the rocks resistance to changes in volume.

The shear modulus ($G$) describes a relationship between shear stress and shear strain, and it represents the rocks resistance to shear deformations (Figure 3.4c). One interesting feature about the shear modulus is that it is zero for fluids, and thus it is independent of the fluid saturation of a rock.

### 3.2.2 Seismic waves and rock impedance

There are two types of seismic waves that need to be discussed – P-waves (compressional/primary waves) and S-waves (shear/secondary waves) (Figure 3.5). They are both body waves, and the fundamental difference between these waves is the particle displacement as the waves propagate through the medium. For P-waves, the particle displacement is parallel to the propagation direction, and for S-waves, the particle displacement is perpendicular to the propagation direction. The previously discussed elastic properties can be found if the P- and S-wave velocity and density are known (Table 3.1). This means that they can be calculated based on P-sonic, S-sonic and density measurements from well logs.

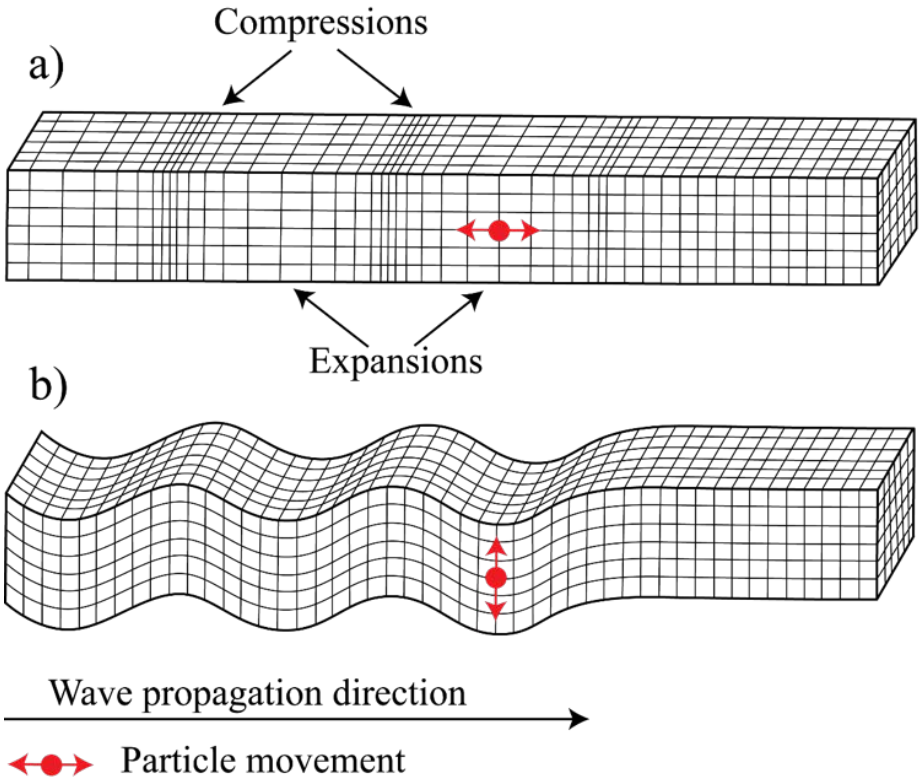


***Figure 3.5**: a) P-waves displace the particles parallel to the direction of wave propagation. b) S-waves displace the particles perpendicular to the direction of wave propagation.*

As S-waves cannot travel through water, marine seismic data are produced from P-waves propagating through the earth. When the waves hit a boundary of two layers of different acoustic impedance (AI), some of the wave energy is reflected and this reflection is recorded as a seismic signal. Theoretically, the earth can be regarded as a model of different acoustic impedance layers (Figure 3.6). Based on this, the reflection coefficient (RC) of a vertically traveling wave can be calculated from the relative difference in acoustic impedance between the layers (Table 3.1). The seismic trace of a vertically propagating wave can be regarded as a convolution of the reflection coefficients and the seismic wavelet plus noise.

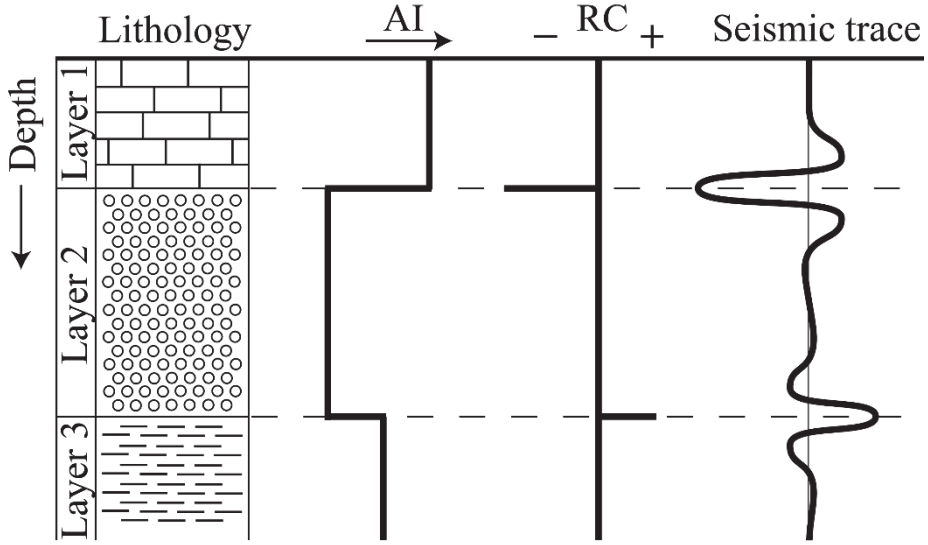


***Figure 3.6**: Illustration of how seismic traces are generated based on different layers of the earth.*

Acoustic impedance is dependent on several factors, such as lithology, porosity, and fluid saturation. Understanding the dependency of acoustic impedance on these factors is crucial when interpreting seismic data, as it helps to recognize what influences the interpreted seismic signals. For instance, an increase in porosity and hydrocarbon saturation, results in a decreasing acoustic impedance (Figure 3.7). This means that a high-porosity gas saturated rock will typically be very soft (low acoustic impedance).

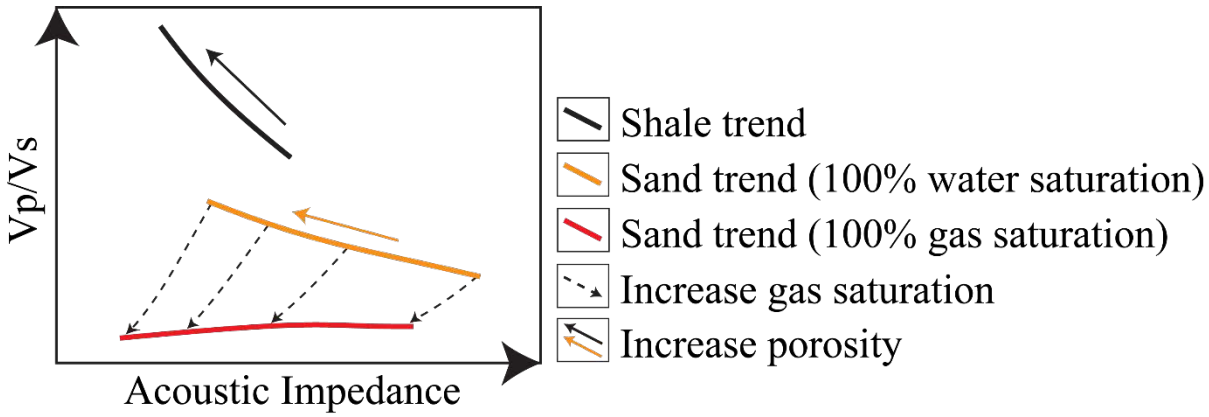


***Figure 3.7**: Typical sand and shale trends in an acoustic impedance-Vp/Vs cross-plot. Solid arrows indicate the effect of porosity, and dotted arrows show how a rock with a given porosity is affected by gas saturation. Modified after Ødegaard and Avseth (2004).*

***Table 3.1**: Equations of some rock properties that are important for this study. Note that all parameters can be determined based on P-wave velocity ($V_p$), S-wave velocity ($V_s$), and density ($\rho$).*

| Property | Equation |
|---|---|
| Young's modulus | $E = \frac{\sigma_{ii}}{\epsilon_{ii}} = \rho V_s^2 \left( \frac{3V_p^2 - 4V_s^2}{V_p^2 - V_s^2} \right)$ |
| Bulk modulus | $K = \frac{-P}{\epsilon_V} = \rho \left( V_p^2 - \frac{4}{3} V_s^2 \right)$ |
| Shear modulus | $G = \frac{1}{2} \frac{\sigma_{ij}}{\epsilon_{ij}} = \rho V_s^2, \qquad i \neq j$ |
| P-wave velocity | $V_p = \sqrt{\frac{K + \frac{4}{3} G}{\rho}}$ |
| S-wave velocity | $V_s = \sqrt{\frac{G}{\rho}}$ |
| Acoustic impedance | $AI = V_p \rho$ |
| Shear impedance | $SI = V_s \rho$ |
| Reflection coefficient | $RC = \frac{AI_2 - AI_1}{AI_2 + AI_1}$ |
| Symbols | $\sigma$: stress<br>$\epsilon$: strain<br>$P$: hydrostatic stress<br>$\epsilon_V$: volumetric strain<br>$\rho$: density |

The velocity of P-waves compared to the velocity of S-waves (i.e., Vp/Vs ratio) can provide important information about the fluid saturation of a rock. This is because S-waves cannot travel through fluids and the S-wave velocity of a rock is thus independent of fluid saturation (excluding the effect of fluid saturation on the density of the rock). On the other hand, P-wave velocity is highly dependent on fluid saturation, which is discussed below. This means that if the same rock at two locations has very different ratios of P- and S-wave velocities, it can have different fluid saturations. The Vp/Vs ratio can also be affected by other factors – typical trends

are an increase in Vp/Vs ratio with porosity, and a decrease with increasing hydrocarbon saturation (Figure 3.7). The effect of hydrocarbon saturation is larger for high porosity rocks.

When combining acoustic impedance and Vp/Vs ratio in a cross-plot, as displayed in Figure 3.7, it may be possible to identify reservoir rocks against non-reservoir rocks. Vp/Vs ratio and acoustic impedance is also closely related to AVO effects, which are discussed below.

## 3.3 Seismic data and AVO

As discussed, marine seismic data is produced from P-waves propagating through the earth. When the waves hit layers of different acoustic impedance, some of the wave energy is reflected, and this reflected energy is recorded as a seismic signal (Figure 3.8).

Seismic data are gathered using different offsets, and conventional seismic data is created by stacking the seismic traces of each common midpoint (CMP) (i.e., the middle point on the surface between the source and receiver that is shared by several source-receiver pairs) after dynamic and static corrections resulting ultimately in full stack seismic. However, important information about fluids and lithology can be obtained from studying the variations in seismic amplitudes as a function of offset (AVO). AVO analysis is commonly based on angle stacks. These are seismic partial stacks that consists of seismic traces that are stacked together based on their angle of incidence

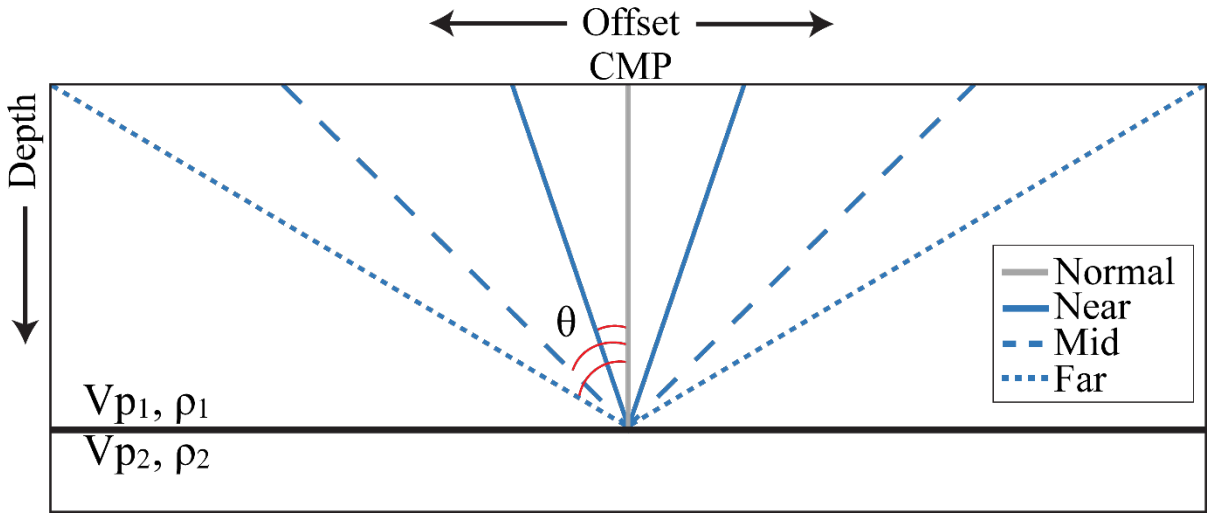


***Figure 3.8**: Schematic overview of how seismic waves are reflected when hitting a boundary between two geological layers of different acoustic impedance. Note how a different offset (near, mid, and far) corresponds to a different angle of incidence, θ (i.e., the angle that the seismic wave makes with respect to perpendicular to the interface).*

### 3.3.1 Seismic velocity

Seismic velocity is dependent on numerous factors, such as lithology, density, porosity, burial depth, fluid saturation, pressure, and temperature. As this study aims to detect and understand how the seismic data respond to hydrocarbon production, the effects of fluid saturation, pressure, and temperature on seismic velocity need to be discussed (Figure 3.9).

Seismic velocity generally decreases when the rocks are saturated with hydrocarbons. This relationship can be explained by looking at the equation for P-wave velocity (Table 3.1). It is dependent on bulk modulus, shear modulus, and density. As the shear modulus is not affected by fluid saturation, the influence of fluids on the seismic velocity is caused by differences in bulk modulus and density. Fluid saturation affects the bulk modulus much more compared to the density, and the bulk modulus is therefore the main contributor to changes in velocity with fluid saturation. This also explains why the S-wave velocity is not much affected by changes in fluid saturation, as it is only dependent on the shear modulus and density. An increase in oil saturation causes a gradual decrease in P-wave velocity; however, only a small amount of gas is required to decrease the velocity dramatically (Figure 3.9a).

The pressure that affects the seismic velocity is the effective pressure (i.e., the difference between the confining pressure and pore pressure – similar to the effective stress discussed above) (Sheriff and Geldart, 1995). As illustrated in Figure 3.9b, seismic velocity does not change with external pressure as long as the effective pressure is kept constant; however, the velocity is altered when changing the effective pressure. As discussed above, the effective pressure typically increases with a reduction in pore pressure, and this can cause compaction. This process can stiffen the elastic mineral frame by closing small cracks, which is believed to be the main reason for the increase in seismic velocity (David and Zimmermann, 2012)

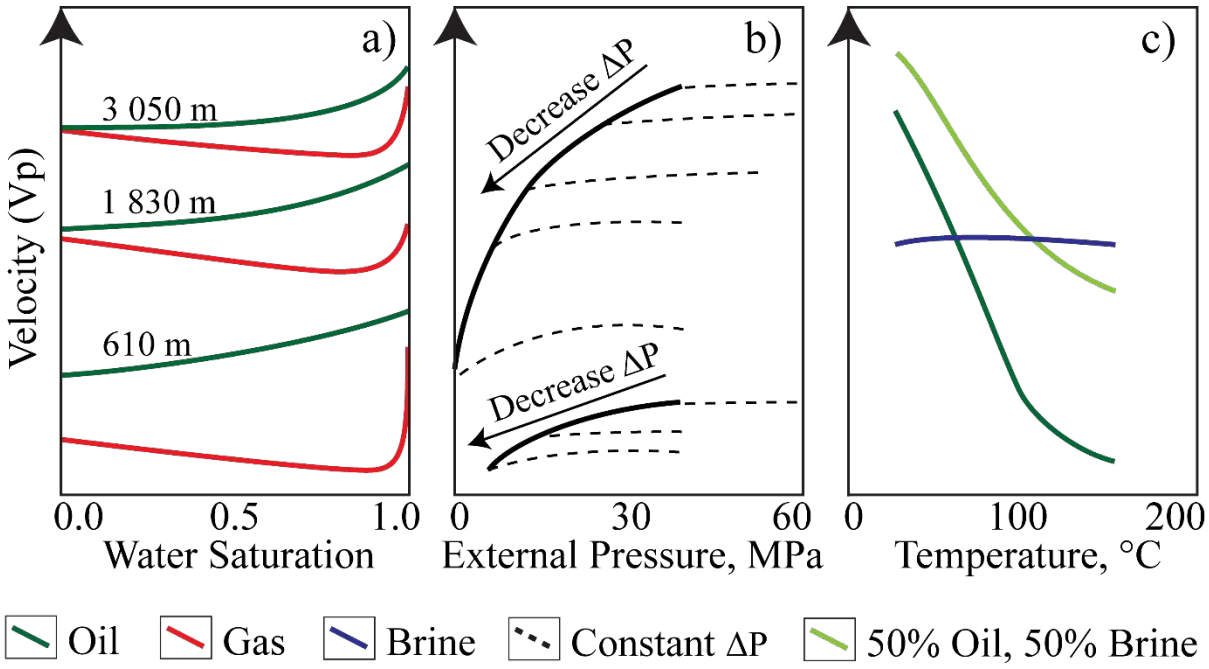


***Figure 3.9**: a) Effect of oil/water and gas/water saturations on the seismic velocity of a rock buried at different depths. Modified after Domenico (1974). b) Effect of effective pressure (ΔP) on seismic velocity of two different rock samples. Modified after Hicks and Berry (1956). c) Effect of temperature on seismic velocity of a rock saturated with different fluid combinations. Modified after Tosaya et al. (1987).*

The effect of temperature on seismic velocity is highly dependent on fluid saturation. As shown in Figure 3.9c, changing the temperature does not affect a brine saturated rock considerably. On the other hand, if the rock is saturated with oil, the velocity is strongly influenced by temperature, where increasing the temperature reduces the velocity (Wang and Nur, 1988).

This is the background for using time-lapse seismic to monitor reservoirs that are produced with thermal recovery (i.e., hydrocarbon production helped by heating the reservoir) (Sheriff and Geldart, 1995).

From what has been discussed above, it is obvious that hydrocarbon production will affect seismic velocities. The main contributors are changes in fluid saturation (i.e., increase in water saturation) and pressure (i.e., decrease in pore pressure), and these should both increase the seismic velocity.

As this study is applied to a compacting reservoir, this effect on seismic velocity also needs to be discussed. Variations in seismic velocity caused by compaction can mostly be attributed to the effect of changes in porosity. Velocity is highly dependent on porosity, where a decrease in porosity typically causes an increase in velocity. This dependency is displayed in Figure 3.10, which shows data from Han et al. (1986), Yin et al. (1988) and Hamilton (1956), plotted together with the Reuss and Voigt bounds. The Voigt bound represents the upper limit for the effective modulus, and it is found by assuming a uniform strain field. The Reuss bound represents the lower limit and is found by assuming a uniform stress field. Mathematically, the Voigt ($M_V$) and Reuss ($M_R$) averages represent different ways of summing the modulus of different components ($M_i$) and their volume fraction ($f_i$):

$$M_V = \sum f_i M_i \ , \qquad \frac{1}{M_R} = \sum f_i \frac{1}{M_i}$$

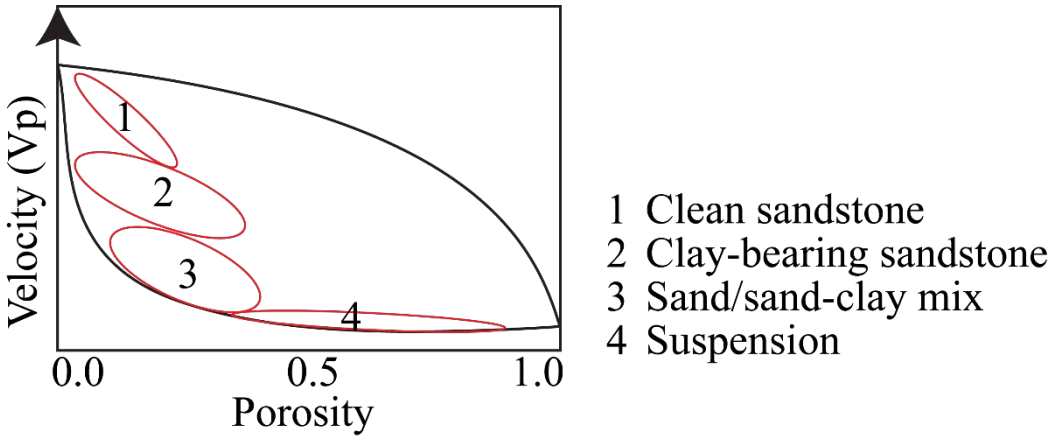


***Figure 3.10**: The relationship between porosity and seismic velocity, illustrated using the Reuss (lower) and Voigt (upper) bounds plotted together with data from Han et al. (1986) (1 and 2), Yin et al. (1988) (3), and Hamilton (1956) (4). Modified after Marion (1990).*

### 3.3.2 Approximations of the reflection coefficient – AVO

In order to understand why certain AVO effects can be used as hydrocarbon indicators, the equations describing how seismic waves are reflected at a boundary between two different geological layers need to be discussed. This is given by the Zoeppritz (1919) equations. However, these equations are complicated and difficult to use for practical purposes. Because of this, several authors have derived approximations to the equations (e.g., Aki and Richards, 1980; Fatti et al., 1994; Shuey, 1985; Smith and Gidlow, 1987; Wang, 1999), making it easier to understand how and why the seismic amplitudes are varying with offset. The approximations have been proven to be accurate in estimating typical AVO responses (Figure 3.11). The

mismatch between the approximations and the Zoeppritz equations are shown in Table 3.2 as RMS error for different intervals of incident angle. Minor mismatches are shown for the Shuey's approximation for medium-high incident angles (θ>20°) and for the Aki-Richards three-term approximation for high angles (θ>30°) (Booth et al., 2016). The mismatches are however small and insignificant for typical AVO analysis.

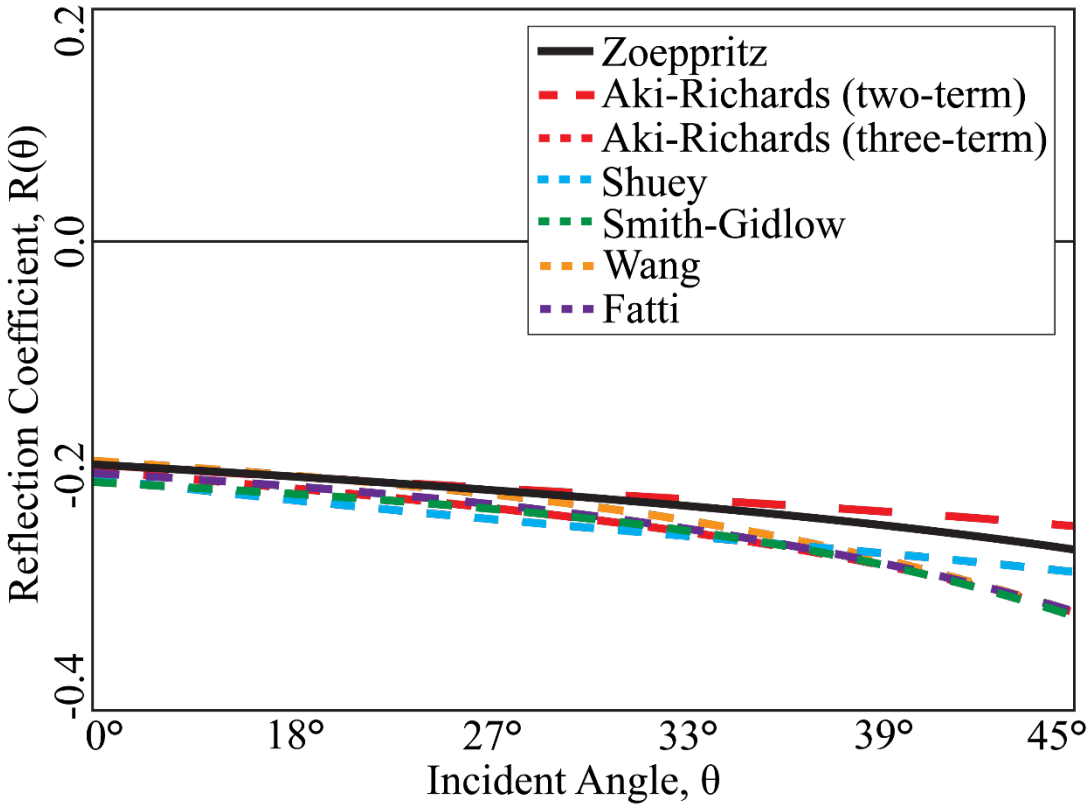


***Figure 3.11**: Reflection coefficient as a function of incident angle (θ) for a shale-gas-sand boundary, plotted using the Zoeppritz (1919) equations and several approximations. Modified from Booth et al. (2016).*

***Table 3.2**: The mismatch between different approximations and the Zoeppritz (1919) equations for the reflection shown in Figure 3.11. It is expressed as the RMS error for different intervals of incident angle. Modified after Booth et al. (2016).*

| Approximation | RMS error θ≤20° | RMS error θ≤30° | RMS error θ≤45° |
|---|---|---|---|
| Aki-Richards (two-term) | 0.0-0.1 | 0.0-0.1 | 0.0-0.1 |
| Aki-Richards (three-term) | 0.0-0.1 | 0.0-0.1 | 0.1-0.2 |
| Shuey | 0.0-0.1 | 0.1-0.2 | 0.1-0.2 |
| Fatti | 0.0-0.1 | 0.0-0.1 | 0.0-0.1 |

For this study, the approximation by Shuey (1985) is applied. Shuey introduced three parameters called intercept (A), gradient (B) and curvature (C), based on Aki and Richard's approximation. The equation describing this is:

$$R(\theta) \approx A + Bsin^2\theta + Csin^2\theta tan^2\theta$$

The intercept represents the reflection coefficient at zero offset (i.e., $R(\theta = 0) \approx A$), the gradient describes how the reflection coefficients are changing with incident angle (i.e., the

slope of the curve in the $R(\theta) - \theta$ domain), and the curvature is important when the incident angle is approaching the critical angle (i.e., the incident angle at which a refracted seismic wave travels along the interface between two layers). For restricted incident angles (i.e., $\theta < 30°$), the curvature is often neglected, leading to the two-term equation where the reflection coefficients are given by the incident angle, intercept, and gradient.

### 3.3.3 Intercept and gradient

The intercept ($A$) is dependent on the P-wave velocity and density of the layers above and below a boundary. The equations for the intercept and gradient are based on the parameters defined in Table 3.1. The equation for the intercept is:

$$A = \frac{1}{2}\left(\frac{\Delta V_p}{V_p} + \frac{\Delta \rho}{\rho}\right)$$

The gradient ($B$) takes into account the S-wave velocity in addition to the P-wave velocity and density, and it is given by:

$$B = \frac{1}{2}\frac{\Delta V_p}{V_p} - 4k^2\frac{\Delta V_s}{V_s} - 2k^2\frac{\Delta \rho}{\rho}, \qquad k = \frac{V_s}{V_p}$$

From the expressions of the intercept and gradient, it is clear that the intercept is closely related to acoustic impedance and the gradient is linked to the Vp/Vs ratio. This means that the intercept is a measure of the relative difference in acoustic impedance across an interface between two layers, and the gradient is related to the relative difference in Vp/Vs ratio. As explained in chapter 3.2.2, these properties can be used to identify hydrocarbons, which explains why the AVO response of a seismic reflector is commonly used as a hydrocarbon indicator.

Rutherford and Williams (1989) introduced the three AVO classes, 1, 2, and 3, based on a shale/gas sand interface (Figure 3.12). These classes are characterized by different features – class 1 has a positive intercept and negative gradient, class 2 has a weak positive or negative intercept and a negative gradient, and class 3 has a large negative intercept and a negative gradient. Class 4 was introduced by Castagna and Swan (1997), and it is characterized by a large negative intercept and a positive gradient. This AVO response is often similar to the background trend, making it difficult to identify.

Figure 3.12 shows the four AVO classes and how they are related when plotted in the different domains. Table 3.3 summarizes the characteristics of the different classes. This shows how the intercept and gradient are related to the relative difference in acoustic impedance and Vp/Vs ratio of the two layers above and below an interface. The most common hydrocarbon indicator in AVO analysis is a class 3 response – this class is related to reservoir rocks of very low acoustic impedance and Vp/Vs ratio compared to the overlying formation.

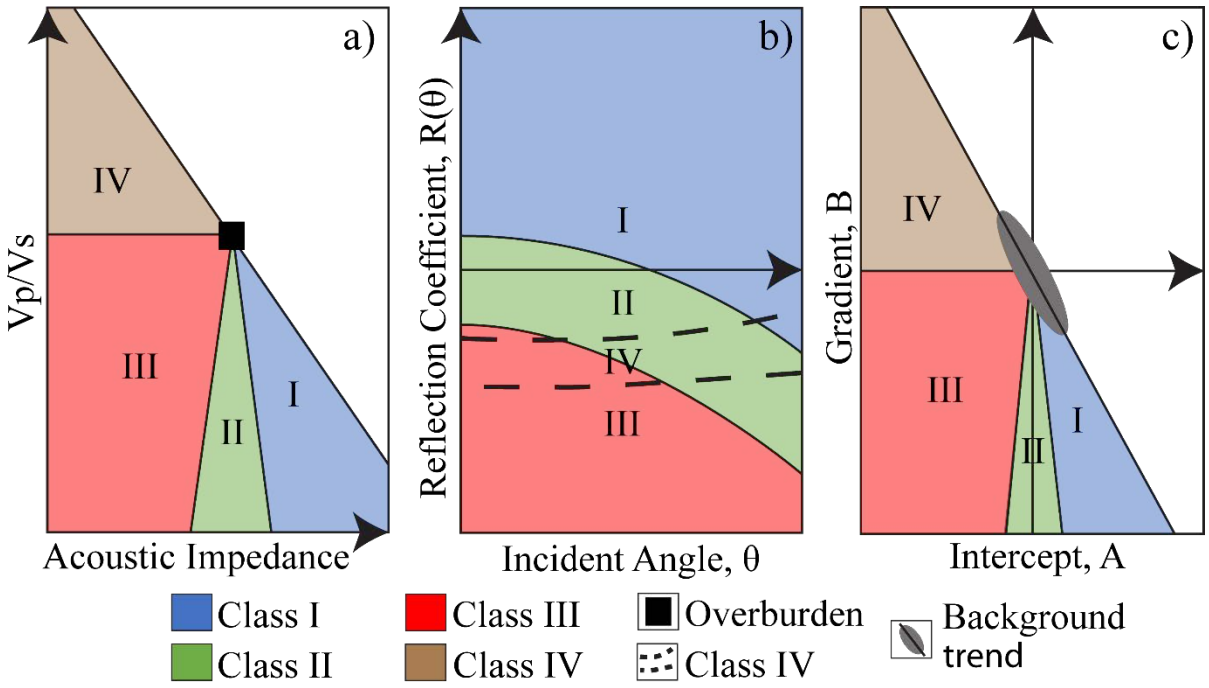


***Figure 3.12**: a) Cross-plot illustrating how the different AVO classes are related to relative changes in acoustic impedance and Vp/Vs ratio across an interface (i.e., the difference between the layers above (black square) and below a boundary). b) The AVO classes are plotted as reflection coefficient vs incident angle. c) An intercept-gradient cross-plot of the AVO classes.*

***Table 3.3**: Characteristics of the different AVO classes and how they are related to rock physics (i.e., how acoustic impedance and Vp/Vs ratio changes across on interface).*

| Class | Change in AI | Change in $V_P/V_S$ | Intercept, A | Gradient, B | A*B |
|---|---|---|---|---|---|
| 1 | Increase | Decrease | + | - | - |
| 2 | Increase/decrease | Decrease | +/- | - | +/- |
| 3 | Decrease | Decrease | - | - | + |
| 4 | Decrease | Increase | - | + | - |

## 3.4 Coloured inversion

The general idea of seismic inversion is to transform seismic data representing contrasts between different layers to actual properties of the layers. This was previously a time-consuming technique that was only applied by experts. The method known as coloured inversion was introduced by Lancaster and Whitcombe (2000), and it allows relatively quick and accurate inversion of seismic traces.

### 3.4.1 Band-limited trace integration

A fundamental problem with seismic inversion is that the seismic data are band-limited, and lack high and low frequencies. This means that seismic data lack information about the earth impedance that is available in well data. Information about the absolute impedance values are found in the low frequencies (below seismic frequency band), and the high frequencies (above

seismic frequency band) provide more details. As this is not captured in the seismic data, an integrated seismic trace delivers a smooth form of the impedance.

Figure 3.13 illustrates how a band-limited integrated trace is related to impedance and seismic data. Note that the layers change on the zero-crossing (i.e., where the amplitude of the seismic trace is zero) on the band-limited impedance trace, whereas the seismic trace is zero-phase (i.e., symmetrical wavelet about zero time). This is due to a -90° phase rotation of the seismic data, when generating the impedance trace. Also, note that the band-limited impedance approaches zero where there is no seismic signal, meaning that the impedance of the entire layers are not properly captured. This is a result of the lack of the low frequency components in the seismic data.

### 3.4.2 Operator

Coloured inversion is a combination of trace integration with a shaping of the amplitude spectrum. The idea is to generate a band-limited model of the impedance of the earth. This is done by obtaining the relative impedance from the seismic data with an amplitude spectrum similar to the well log data within the seismic frequency band (Simm and Bacon, 2014).

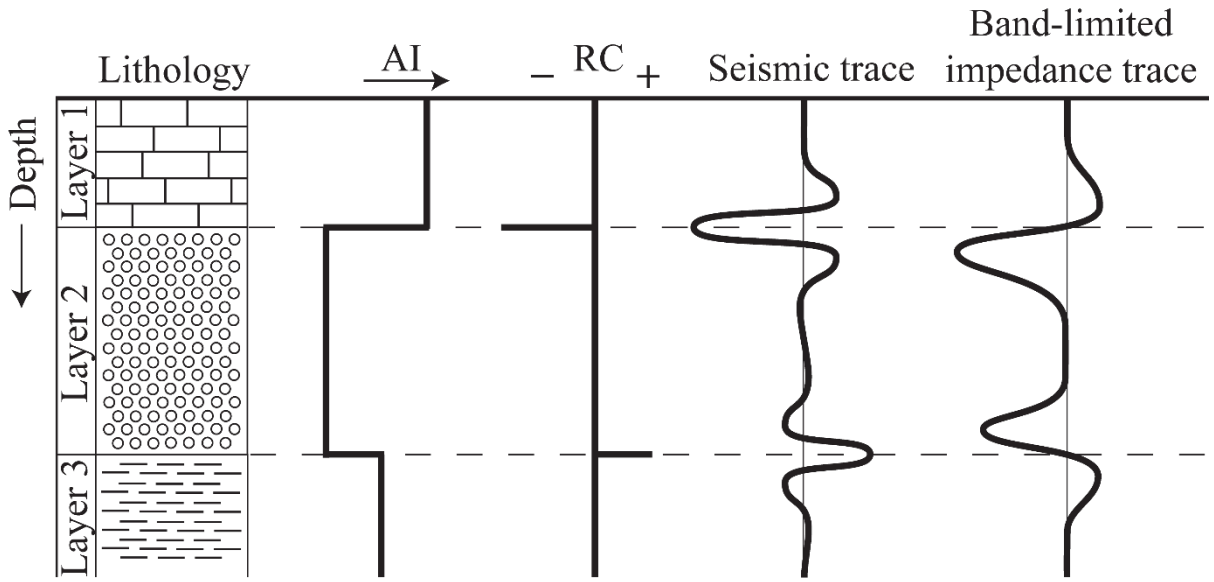


***Figure 3.13**: Schematic illustration of how band-limited impedance relates to seismic data.*

In practical terms, the coloured inversion process is conducted by convolving the seismic data with an operator (Figure 3.14). The operator has a constant phase of -90°, which is based on the assumption that the seismic data are zero-phase. The acoustic impedance spectrum of the earth is reasonably constant at reservoir scale and can be estimated by a best-fit line obtained from well log data. The operator is designed such that it maps the amplitude spectrum of the mean seismic response to follow this trend (Lancaster and Whitcombe, 2000). In addition, a band-pass filter is applied based on the seismic band-with, in order to obtain the band-limited inverted result.

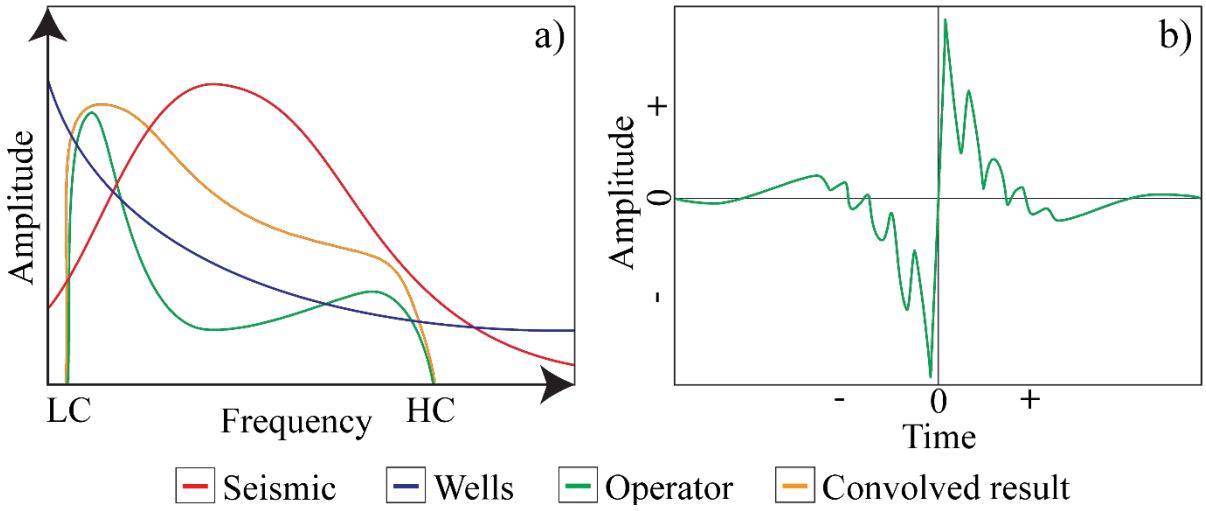


***Figure 3.14**: a) Schematic representation of the amplitude spectrum of a seismic cube, average well data, an operator, and a convolved result (i.e., the coloured inversion result). Note that the seismic lacks low and high frequencies compared to the well data. The frequency ranges of the operator and the convolved result are determined by a band-pass filter, here illustrated as high and low frequency cut-offs (i.e., LC and HC). b) An illustration of an operator displayed in time. Modified after Lancaster and Whitcombe (2000).*

## 3.5 Time-lapse seismic

Time-lapse seismic is typically used for reservoir monitoring, where it is expected that the 3D seismic cubes acquired at different times are able to identify changes in reservoir structure and fluid migration. In order to detect these effects in seismic data, it is important that the seismic acquisition and processing does not induce too much noise in the data. The issues related to the repeatability of the seismic data are linked to several factors. Typical problems include variations in the following parameters (Landrø, 2015):

- Position of source and receiver
- Weather conditions
- Water temperature
- Tidal effects
- Noise from activity in the area (e.g., rigs and vessels)
- Acquisition system (e.g., vessels, cables, and sources)
- Shot generated noise

With the exception of the weather conditions, the variations in these factors can be minimized by proper planning and performance of the acquisition. If this is done appropriately, the different seismic cubes will have the same amplitude and frequency range, and they will be well aligned horizontally and vertically. In such case, the time-lapse seismic interpretation can be trusted.

### 3.5.1 Compaction

When studying time-lapse seismic, compaction is identified by analysing time-shift data (i.e., difference in elevation of the same seismic reflectors between the different surveys). An overview of what happens when a reservoir is compacted is given in Figure 3.15a. Compaction causes a stretching of the overburden – this means that the thickness of the layers in the

overburden increases (i.e., Zf>Zi, where i and f represent initial and final time points before and after compaction), whereas the thickness of the reservoir decreases (i.e., Zf<Zi). In other words, the actual depth of the overburden and top reservoir reflectors increases. This is indicated as elevation difference by the vertical red lines in Figure 3.15a. Another, more complex consequence, is the change in velocity – the stretching of the overburden decreases the velocity (i.e., Vf<Vi) and the reservoir compaction increases the velocity (i.e., Vf>Vi). This means that the overburden and top reservoir reflectors appear to be located at a deeper elevation, due to the decrease in velocity of the overburden (Landrø, 2015).

The time-shift is thus a function of change in thickness and velocity. The relative change in seismic travel time ($t$) for a layer with thickness, $z$, and velocity, $v$, is given by (Landrø and Stammeijer, 2004):

$$\frac{\Delta t}{t} = \frac{\Delta z}{z} - \frac{\Delta v}{v}$$

Based on this, a major challenge of the analysis of time-shift data is to distinguish between thickness and velocity changes. Hatchell et al. (2005) and Røste et al. (2005) suggest to use the R-factor to relate relative velocity changes to relative thickness changes. Combining this factor with the equation above allows separating thickness and velocity changes:

$$\frac{\Delta t}{t} = (1+R)\frac{\Delta z}{z} = -\left(\frac{1+R}{R}\right)\frac{\Delta v}{v}, \qquad R = -\frac{\Delta v/v}{\Delta z/z}$$

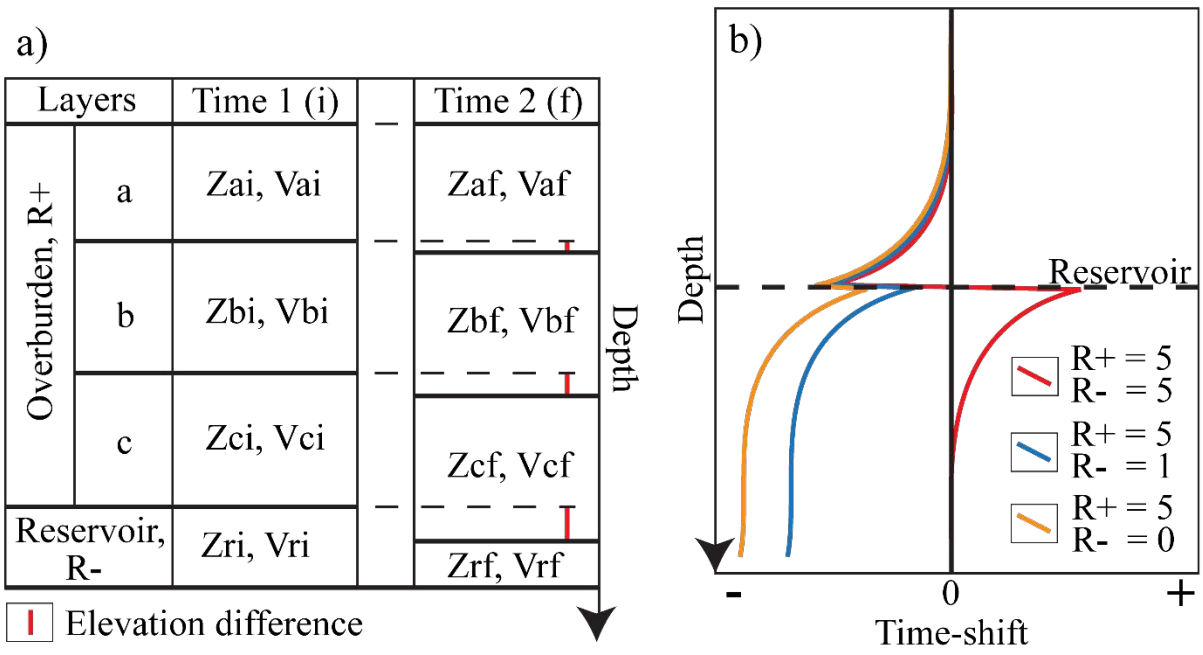


***Figure 3.15**: a) Schematic overview of how compaction affects the thickness and velocity of the reservoir and the overburden. Z denotes the thickness of the different layers, and V the velocity, for the initial (i) and final (f) times. b) The effect of a compacting reservoir on time-shift data, plotted for different $R^-$-values, keeping the $R^+$-value constant. Negative time-shift indicates that the depth of the reflectors increases with time and positive time-shift indicates that the depth decreases. Modified after Hatchell and Bourne (2005).*

It is evident from these equations that a positive time-shift indicates that the reflectors are shifted downwards with time. However, in the software used for this study (Petrel), the time

axis is of type elevation, which means that it decreases with depth. Consequently, in this study, a negative time-shift indicates downwards shift of the seismic reflectors.

The velocity response to changes in seismic layer thickness varies greatly for different lithologies. This means that the R-factor is strongly dependent on the properties of the rocks, and it is of special importance to distinguish between compacting and extending formations. This led to the introduction of $R^+$ (i.e., extending rocks, Zf>Zi) and $R^-$ (i.e., compacting rocks, Zf<Zi). Hatchell and Bourne (2005) show that the seismic velocity is more sensitive to extending rocks than to compaction. They modelled the time-shift of a compacting reservoir and found that in order to observe a negative time-shift below the reservoir, which is commonly observed in compacting reservoirs, $R^+$ needs to be significantly larger than $R^-$ (Figure 3.15b).

Figure 3.16 shows two examples of time-lapse analysis based on time-shift data. The time-shift of the top reservoir at the Ekofisk field is displayed in figure a), showing a significant downward movement of the reflector. The time-shift of the Valhall field is displayed in a cross section in figure b). It is clear that the negative time-shift continuous through the reservoir and below. As discussed above, this is commonly observed in compacting reservoirs, and it is an indication that the seismic velocity is more sensitive to the stretched overburden, than to the compacting reservoir (i.e., $R^+>R^-$).

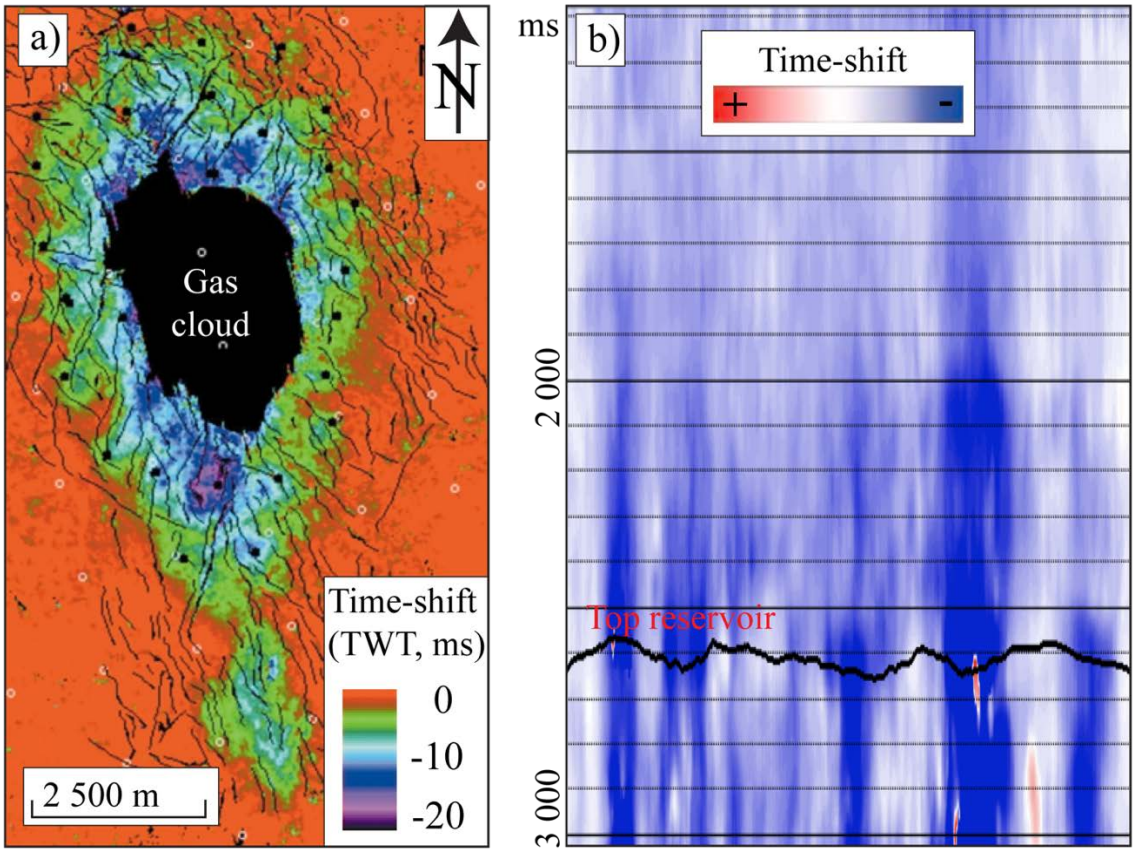


***Figure 3.16**: a) Time-shift of the top reservoir reflector on the Ekofisk field in the North Sea. Modified after Guilbot and Smith (2002). b) Time-shift in a seismic section across the Valhall oil field, also in the North Sea. Modified after Hatchell et al. (2005).*

### 3.5.2 Fault reactivation

Fault reactivation can be identified from time-lapse seismic mainly in two different ways – by analysing time-shift data and by measuring the difference in continuity of the seismic reflectors (Figure 3.17). The latter is typically based on analysis of differences in the response of the faults on seismic attributes that highlight faults (e.g., variance and amplitude contrast). Given that fault reactivation causes a difference in fault displacement, it is assumed that this is possible to detect in time-shift data (i.e., the time-shift is not constant across the fault). This assumption may not be valid for small displacement changes below the resolution of the time-shift data and thus masked by noise.

The difference in seismic response due to fault reactivation is not only reliant on inconsistent time-shift across the fault. For example, constant compaction across a fault would still cause differences in amplitude, due to the vertical movement of the horizons.

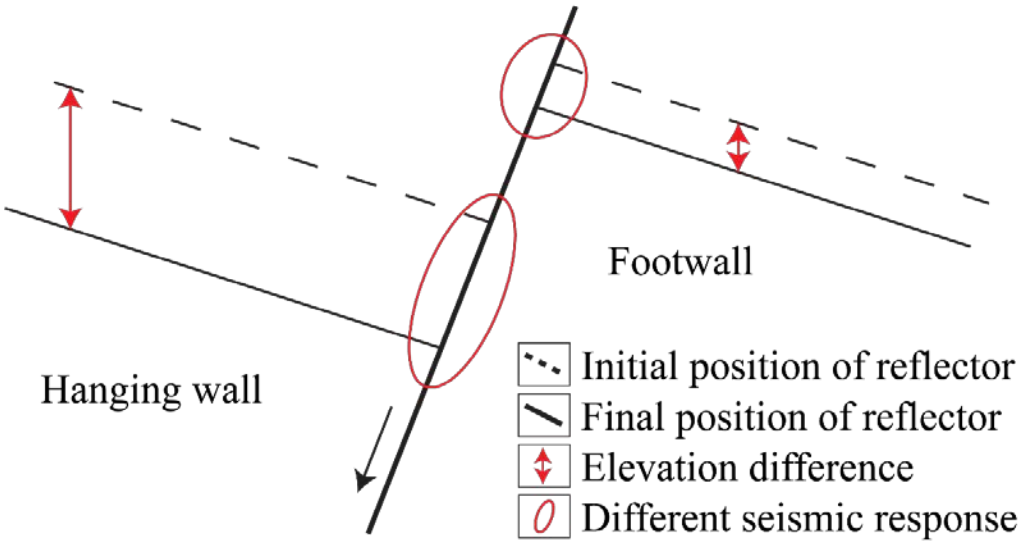


***Figure 3.17**: Schematic representation of how fault reactivation may affect seismic data. The two main effects are difference in time-shift across the fault and difference in the seismic response where the reflectors meet the fault.*

### 3.5.3 Fluid migration

As discussed above, acoustic impedance and seismic reflectivity are dependent on fluid saturation, and this forms the basis for applying time-lapse analysis with the aim to detect fluid movements. Figure 3.18 shows an example of how amplitudes vary with hydrocarbon production. As oil is produced and the oil-water contact moves upwards, the strong amplitude reflector of the top reservoir disappears for the lower part (i.e., below the oil-water contact). Figure 3.19 shows another time-lapse study, where the difference in reflectivity was calculated based on 90° phase rotated seismic data. A clear hardening effect (increase in acoustic impedance) is observed where the water saturation increases, and this allows the interpretation of the water flood front. Since different fluids and fluid contacts can be interpreted on seismic data, time-lapse seismic can identify unswept hydrocarbons, which is often the goal of reservoir monitoring.

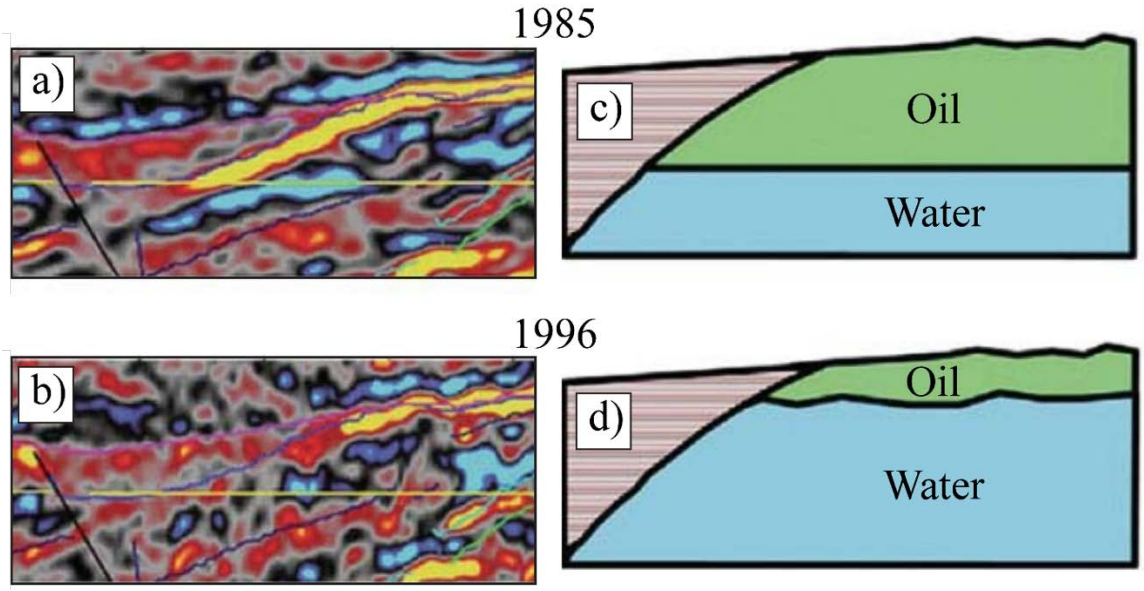


***Figure 3.18**: Seismic sections from 1985 (a) and 1996 (b) across the Gullfaks field in the North Sea. Effects of reservoir depletion are clearly observed as decreased amplitudes, allowing the interpretation of changes in the oil-water contact (c and d). Modified after Landrø (2015).*

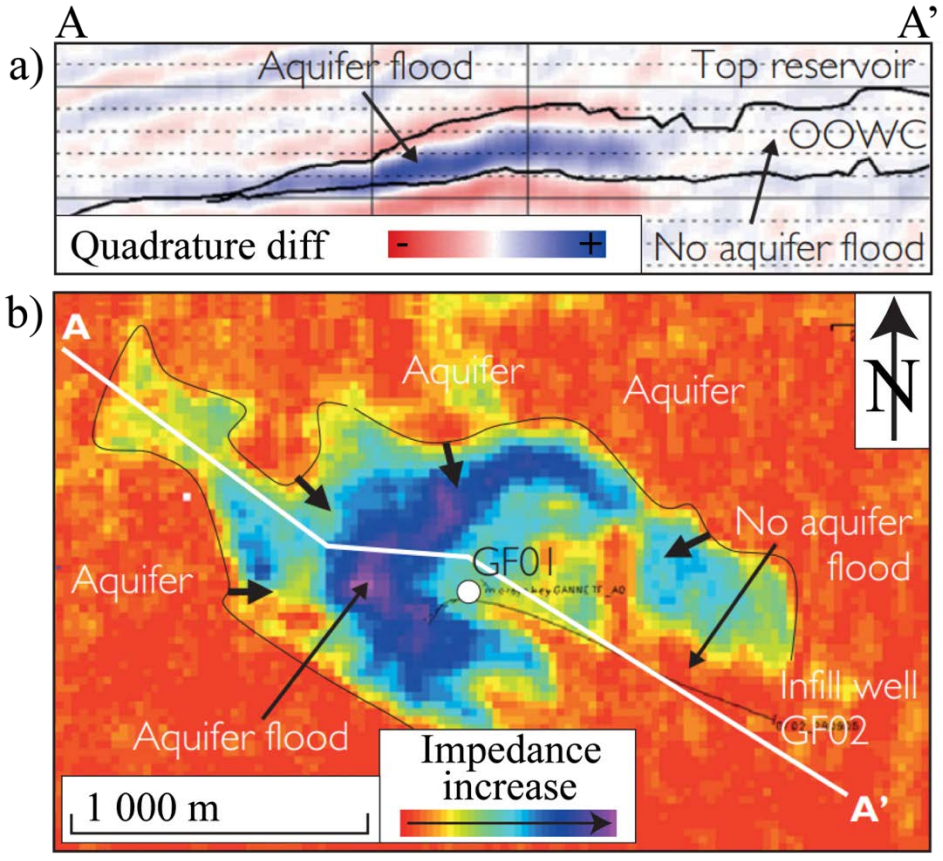


***Figure 3.19**: Time-lapse study of the Gannet F field in the North Sea. a) A cross section of the 90° phase rotated reflectivity difference across the field reveals the movement of the aquifer by an increase in impedance. b) The impedance increase is also observed in map view and interpreted as water encroachment. Modified after Staples et al. (2007).*

## 3.6 Seismic attributes and processes

Several seismic attributes and processes are applied in this study with the aim to detect subtle features that are not very easily observed in conventional seismic display. Before applying the attributes, the theory behind them is briefly discussed.

### 3.6.1 Variance

The Variance attribute is an edge detection attribute that estimates the local variance in the seismic signal of neighbouring traces. This means that it measures the horizontal continuity of the seismic reflectors and is thus capable of highlighting structural features like faults and fracture zones. Dip-guided variance is very useful when interpreting dipping reflectors. It computes the variance along the dipping reflectors instead of simply on a horizontal neighbourhood. Using regular variance (i.e., not dip-guided) will often result in interpretation of steeply dipping reflectors as faults.

### 3.6.2 Edge evidence

The Edge Evidence attribute searches for line segments with values that are significantly different from the surrounding values. It enhances amplitude edges by statistical methods, and it can thus be used for enhancing fault responses. Typically, the process is applied on an edge volume (e.g., a variance cube), and thus it highlights and increases the continuity of the fault response.

### 3.6.3 Ant tracking

Ant tracking is not regarded as an attribute, but it is an algorithm that is applied on a fault attribute cube. The algorithm uses ants (i.e., intelligent software agents), which extract the features in the input fault attribute cube that correspond to the expected behaviour of faults. The ant tracking algorithm is typically applied in a workflow starting with an edge detection attribute (e.g., variance), then an edge enhancement attribute (e.g., edge evidence) is applied on the edge detection attribute, and finally the ant tracking algorithm is applied on the edge enhancement cube (Figure 3.20). The result is a fault cube, which theoretically represents the fault pattern resolved by the seismic.

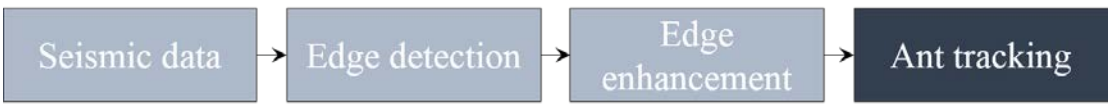


***Figure 3.20**: A typical ant tracking workflow consists of several steps, and it is assumed that the result is a proper fault cube.*

### 3.6.4 RMS amplitude

The RMS Amplitude attribute represents a calculation of the root mean square of the amplitudes at each trace over a user-defined gliding time window. It can generally be applied

on several types of data where the aim is to detect anomalies, rather than analysing the exact values of the data.

### 3.6.5 Seismic trace alignment

The Seismic Trace Alignment process is used to match different seismic cubes in order to properly compare the seismic data. It is based on the non-rigid matching technology described by Nickel and Sønneland (1999). The method estimates displacements based on the input cubes (Figure 3.21). The displacements are then applied to the cube to be matched, resulting in the matched cube. The process is typically applied to angle stacks prior to AVO and inversion workflows, and it is also used to align time-lapse seismic data.

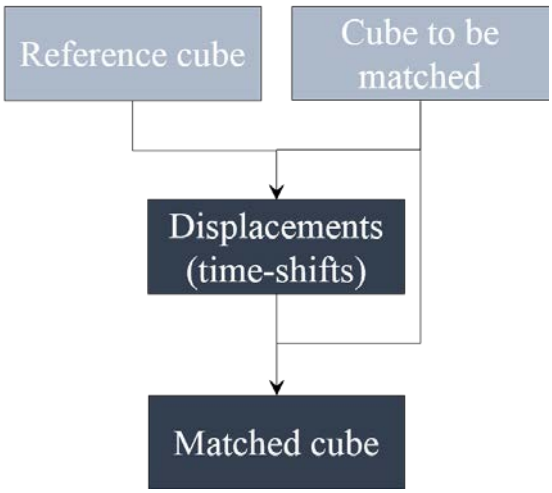


***Figure 3.21**: The seismic trace alignment process delivers the displacements and the matched cube. Modified after Nickel and Sønneland (1999).*

# 4. Data

The data used for this study consists of three 3D seismic cubes and well information from 22 wells (Figure 4.1). In this chapter, the data are introduced and briefly discussed.

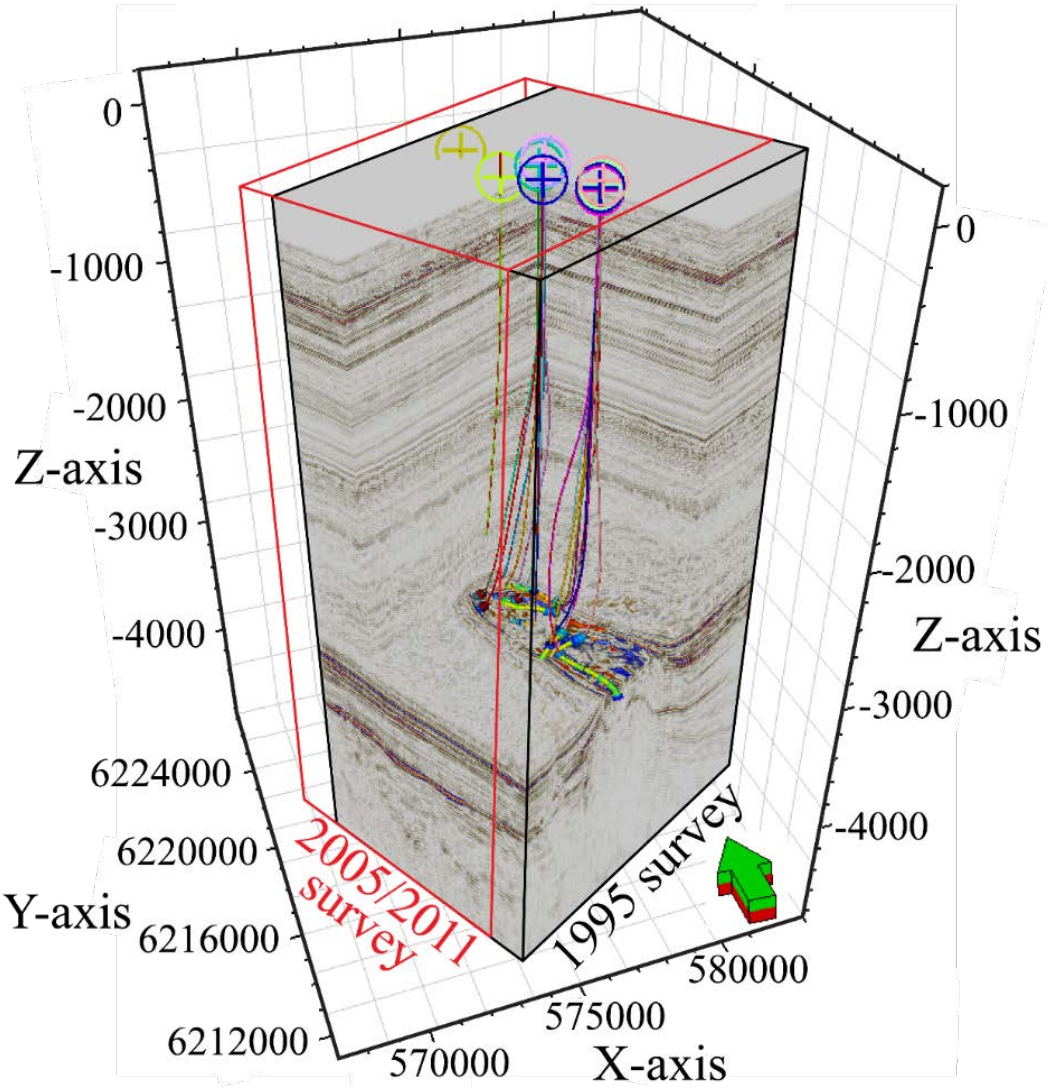


***Figure 4.1**: 1995 full stack seismic cube displayed together with the wells and the geometry of the 1995 survey (black) and 2005 and 2011 surveys (red).*

## 4.1 Seismic

For the purpose of reservoir monitoring, 3D seismic has been acquired at three different times – one base survey (pre-production) in 1995 and two monitor surveys in 2005 and 2011 (Figure 4.1). The seismic surveys have high repeatability, making them well-suited for time-lapse studies. The polarity of the seismic data is SEG (Society of Exploration Geophysicists) standard, meaning that the seismic response coming from an increase in acoustic impedance with depth is a positive peak. Compared to the monitor surveys, the base survey has some extra

inlines to the SSE and lacks some inlines to the NNW. There is an area in the seismic data with very low signal-to-noise ratio, and no information can be trusted in this part (Figure 4.2).

In addition to full stack seismic data, the three different surveys also include near, mid, and far angle stacks. The near stacks comprise seismic data acquired with incident angles in the range of 5-15°, mid stacks 15-25°, and far stacks 25-35° (Table 4.1).

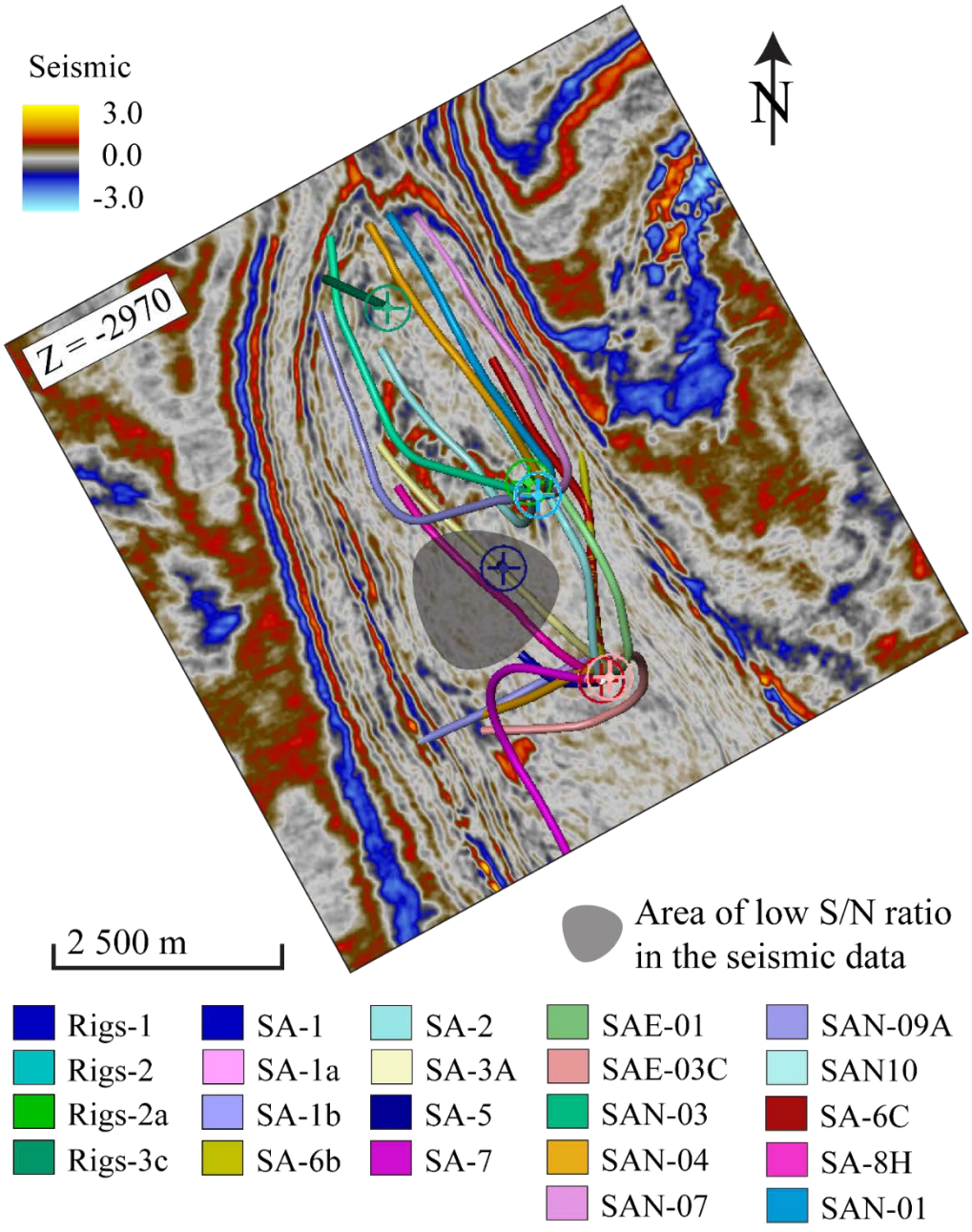


***Figure 4.2**: A time-slice of the 1995 full stack seismic displayed together with all the wells.*

## 4.2 Wells

Data from several wells are available, including exploration, appraisal, production, and injection wells (Table 4.2). The wells cover the whole field, and numerous well logs are

included with information at reservoir level. However, not many of the wells include data for the overburden. Check-shot surveys are also included for all the wells. Wells with P- and S-wave sonic and density are of particular interest. Six of the 22 wells have this information.

***Table 4.1**: Summary of the available seismic cubes and surveys.*

| Acquiring year | Stack | Angles, ° |
|---|---|---|
| 1995 | Full | - |
| | Near | 5-15 |
| | Mid | 15-25 |
| | Far | 25-35 |
| 2005 | Full | - |
| | Near | 5-15 |
| | Mid | 15-25 |
| | Far | 25-35 |
| 2011 | Full | - |
| | Near | 5-15 |
| | Mid | 15-25 |
| | Far | 25-35 |

***Table 4.2**: Wells and some of the well logs available for the study. All the wells have gamma ray (GR), density (ρ), total porosity (φ) and water saturation ($S_w$) logs, and some of the wells have P-wave ($Dt_p$) and S-wave ($Dt_s$) sonic logs. The locations of the wells are shown in Figure 4.2.*

| Well type | Well | GR | ρ | $Dt_P$ | $Dt_S$ | φ | Sw | Year |
|---|---|---|---|---|---|---|---|---|
| Exploration | Rigs-1 | Yes | Yes | Yes | Yes | Yes | Yes | 1995 |
| Appraisal | Rigs-2 | Yes | Yes | Yes | Yes | Yes | Yes | 1996 |
| | Rigs-2a | Yes | Yes | Yes | Yes | Yes | Yes | 1996 |
| | Rigs-3c | Yes | Yes | Yes | Yes | Yes | Yes | 2006 |
| | SA-1 | Yes | Yes | Yes | Yes | Yes | Yes | 1998 |
| | SA-1A | Yes | Yes | Yes | Yes | Yes | Yes | 1998 |
| | SA-1B | Yes | Yes | No | No | Yes | Yes | 1998 |
| | SA-6B | Yes | Yes | Yes | No | Yes | Yes | 2000 |
| Producer | SA-2 | Yes | Yes | Yes | No | Yes | Yes | 1998 |
| | SA-3A | Yes | Yes | No | No | Yes | Yes | 1998 |
| | SA-5 | Yes | Yes | No | No | Yes | Yes | 1999 |
| | SA-7 | Yes | Yes | No | No | Yes | Yes | 2000 |
| | SAE-01 | Yes | Yes | No | No | Yes | Yes | 2015 |
| | SAE-03C | Yes | Yes | No | No | Yes | Yes | 2014 |
| | SAN-03 | Yes | Yes | No | No | Yes | Yes | 2014 |
| | SAN-04 | Yes | Yes | No | No | Yes | Yes | 2015 |
| | SAN-07 | Yes | Yes | No | No | Yes | Yes | 2015 |
| | SAN-09A | Yes | Yes | No | No | Yes | Yes | 2016 |
| | SAN-10 | Yes | Yes | No | No | Yes | Yes | 2016 |
| Injector | SA-6C | Yes | Yes | No | No | Yes | Yes | 2000 |
| | SA-8H | Yes | Yes | No | No | Yes | Yes | 2001 |
| | SAN-01 | Yes | Yes | No | No | Yes | Yes | 2013 |

# 5. Methods

In this study, several different methods were implemented based on the theory discussed above. The methods that were applied are summarized in a workflow in Figure 5.1. Firstly, quality control (QC) and conditioning was applied to the seismic data. Then, conventional seismic and well interpretations were conducted, before studying the rock physics. The next steps were to analyse the time-shift data and evidences of fault reactivation. The last methods were amplitude and AVO analysis, before finishing with coloured inversion. The results were compared to detect relationships and trends in the data. The different methods are described in this chapter.

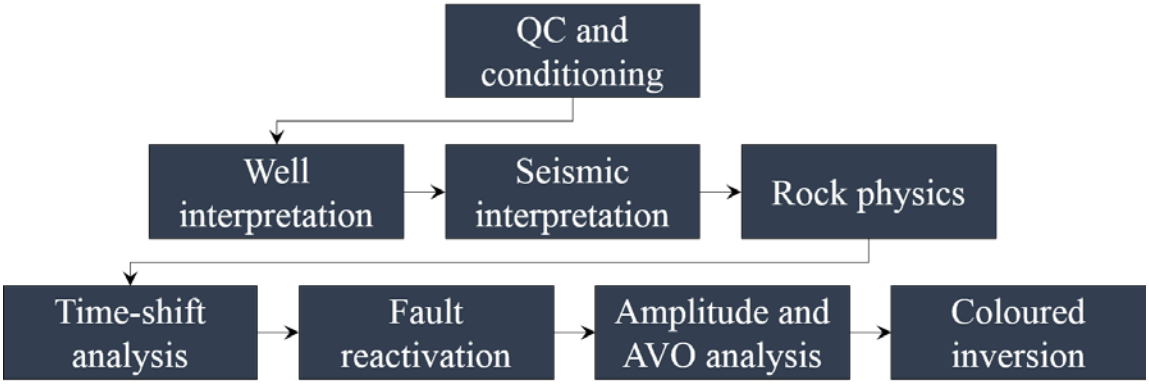


***Figure 5.1**: Workflow of the main methods that were applied in this study.*

## 5.1 Seismic QC and conditioning

Before doing any interpretation, the quality and comparability of the seismic data were examined. The QC was done before a possible conditioning step was applied. It included studies of the time alignment, amplitudes, and frequency of the different seismic cubes. The time alignment and amplitudes were studied on two surfaces at different elevations and the frequencies were studied in a seismic cube outside the reservoir (Figure 5.2).

### 5.1.1 Time-lapse seismic (full stack)

In order to study the difference in elevation and amplitude between the different surveys, the same reflector was interpreted in the exact same way (i.e., same type of tracking and surface generation) for the full-stack 1995, 2005 and 2011 surveys. Then the difference in elevation between the 1995 and the 2005 surfaces, and between the 2005 and 2011 surfaces, were examined by subtracting the two-way travel-times of the surfaces from each other (Figure 5.3).

A similar method was applied with regards to amplitude differences. The exact amplitudes of the different full stack surveys were extracted along the generated surfaces for each survey (i.e., 1995 full stack amplitudes were extracted along the 1995 surfaces, 2005 amplitudes along the 2005 surfaces, and 2011 amplitudes along the 2011 surfaces). Then the amplitude surfaces were subtracted from each other, delivering the difference in amplitude of the interpreted surfaces.

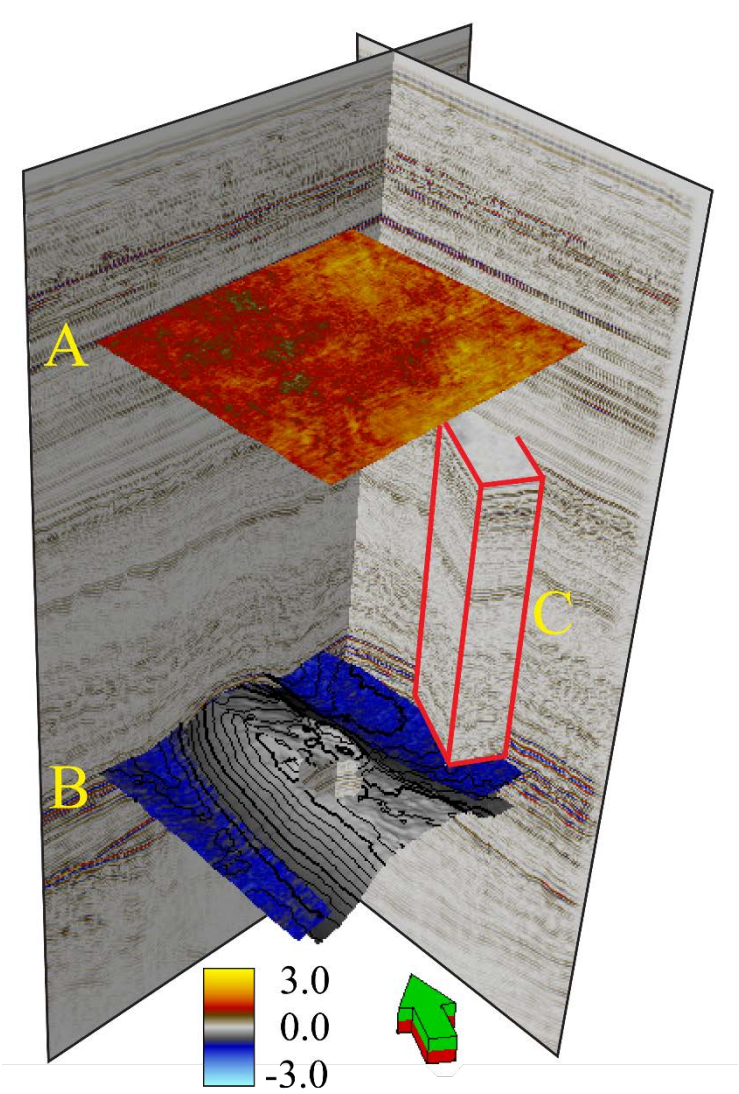


***Figure 5.2**: Two surfaces were used for the QC of elevation and amplitudes between the different surveys. Surface A is located at a much shallower depth than the reservoir and Surface B is at an elevation close to the reservoir level. A cropped seismic cube (C) was used for the frequency QC.*

The differences between the surveys were studied on the interpreted surfaces, and they were also detected by cross-plotting the surfaces against each other. This was done for both the elevation of the surfaces and the extracted amplitudes.

After these methods were applied, the results were studied in order to determine the magnitude of the differences. If the results were not acceptable (i.e., too large differences compared to the analysed anomalies and effects), the application of seismic conditioning was required. After the appropriate conditioning was done, the results were checked to determine whether further corrections were needed.

The frequency contents of the different full stack seismic surveys were examined in a similar way. The frequencies were extracted from a cropped cube outside the reservoir. Then the amplitude spectrum of the 1995, 2005, and 2011 surveys were studied and compared. Major differences here also indicate the necessity of seismic conditioning. Note that a proper

conditioning would typically be done by the seismic data processing centre because of the specialized software involved in the correction.

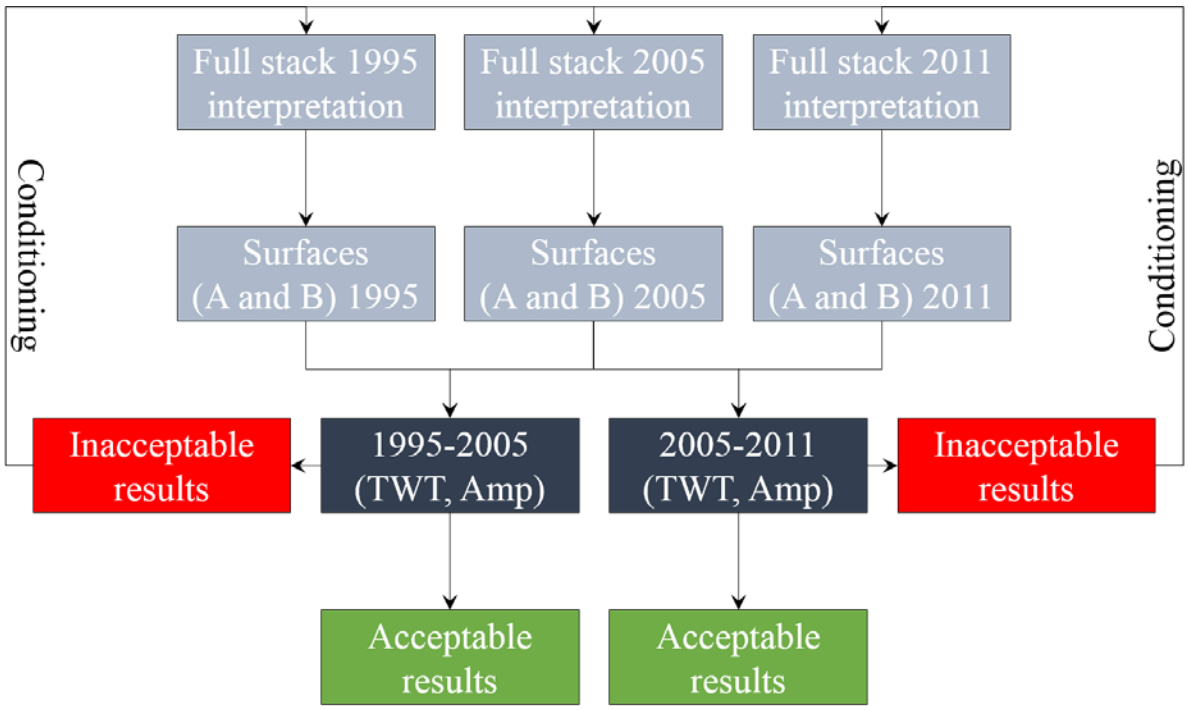


***Figure 5.3**: The seismic QC of the time alignment and amplitudes between the different surveys was conducted by studying two surfaces. These were interpreted on the different full stack cubes, and the results were compared. Significant differences indicated the need of seismic conditioning.*

### 5.1.2 Angle stacks

With the exception of the input data, the exact same approach as for the time-lapse seismic was applied on the angle stacks (Figure 5.3). Instead of using the different full-stack seismic surveys, the near and far stacks of the 1995 survey were now used as input for the QC. This applies to how the time alignment and amplitudes were studied, as well as the frequency content. If the QC indicated the need for conditioning, this was applied on the near, mid, and far angle stacks of the three seismic surveys.

### 5.1.3 Seismic trace alignment

The process discussed above led to the application of seismic trace alignment (Figure 5.4). Before doing this, the geometries of the different surveys needed to be matched (Figure 4.1). This was done by cropping the cubes to the same size and geometry – i.e., removing some of the inlines furthest to the SE on the 1995 survey, and removing some inlines to the NW on the 2005 and 2011 surveys.

The seismic trace alignment process was made complicated by the extensive number of cubes needed to be aligned. The first step was to align the full and near stacks of the 2005 and 2011 surveys to that of the 1995 survey. In addition, this process provided the time-shift cubes based on the full stack seismic.

The next step was to align the angle stacks – this was done by matching the respective mid and far stacks to the already aligned near stacks from the first step (i.e., the mid and far 1995 stacks were matched to the near 1995 stack, etc.). These two steps should result in alignment of all the seismic cubes, allowing them to be properly compared.

A QC was conducted after the application of the trace alignment process. This was done in the same way as the original QC as discussed above, in order to compare the elevation differences before and after the process. This means that the same surface (i.e., Surface B) was interpreted on the different matched cubes, allowing the elevations to be compared – the three full stack seismic cubes were used for the time-lapse seismic, and the near and far stacks of the 1995 survey were used for the angle stacks.

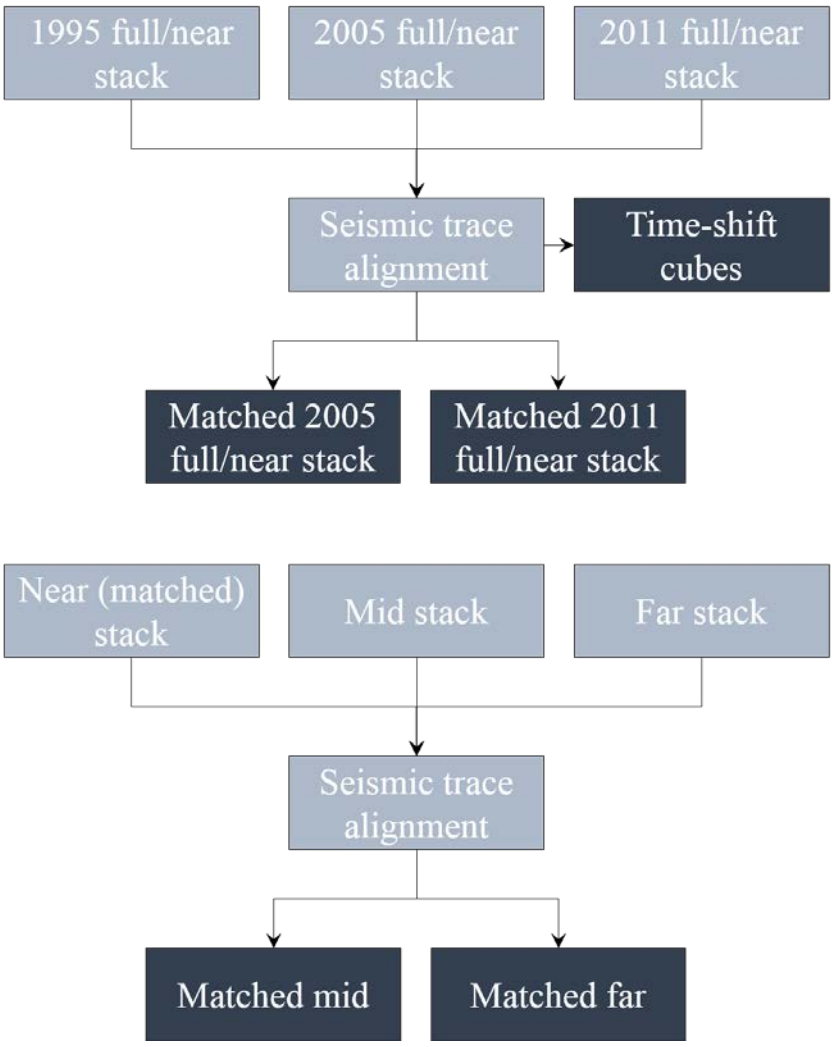


***Figure 5.4****: The seismic trace alignment was applied in two different steps – firstly the full and near stacks were matched, then the angle stacks were matched based on the aligned near stacks from the first step.*

## 5.2 Reservoir overview

The first interpretation method that was applied in this study consists of basic interpretation techniques to get an overview of the reservoir. This includes seismic and well log interpretations. Following the conventional seismic interpretation, structural seismic attributes were also applied.

### 5.2.1 Well log interpretation

The well log interpretation was conducted based on all available wells, and it was based on the well logs in addition to the well tops delivered by the operator. The logs that were used comprised the gamma ray, total porosity, water saturation, density-neutron combination, and acoustic impedance calculated from sonic and density. This well information guided the interpretation of the top and base reservoir, as well as the different zones within the reservoir.

### 5.2.2 Seismic interpretation

Seismic well ties were conducted based on the well interpretations and the 1995 full stack seismic data. Based on the well ties, the top reservoir reflector was interpreted for the whole field, and a top reservoir surface was generated. In addition, faults were interpreted manually based on the seismic data and outlined on the surface. Detailed seismic interpretation of the reservoir zones was only done on some key seismic sections, allowing the interpretation of the main structural features (Figure 5.5).

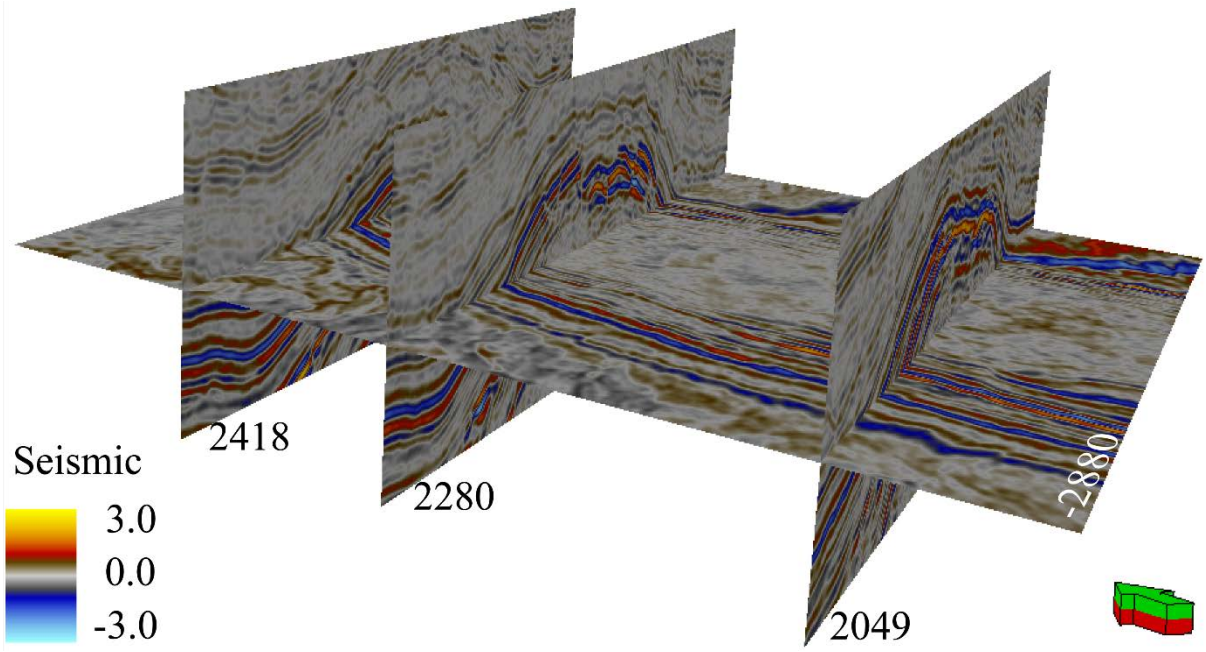


***Figure 5.5**: Detailed seismic interpretation was conducted on the inlines 2418, 2280, 2049. When discussing the results, these seismic lines are denoted A-A', B-B', and C-C'.*

In addition to the conventional seismic interpretation, structural interpretations based on seismic attributes were also conducted. In order to understand the fault and fracture network of

the field, an ant tracking process was applied as discussed in chapter 3.6.3 (Figure 5.6). The dip-guided variance attribute was first used to detect faults on the 1995 full stack seismic, and then the edge evidence attribute was applied twice in order to enhance the variance response. This cube was then used as input for the ant tracking algorithm. The ant tracking results were combined with a dip illumination cube and used to generate a structural attribute map by extracting the exact values at the top reservoir reflector.

The ant tracking cube was also used to generate fault surfaces in order to analyse the main structural trends. This was done by first cropping the ant tracking cube, so that it only contained information in an interval of 25 ms above the top reservoir reflector to 125 ms below. Subsequently, this cube was divided into four smaller cubes representing different areas of the data – one cube was generated on each side of the anticline (WSW and ENE) and two cubes were created on the anticline (NNW and SSE) (Figure 5.7). The automatic fault extraction process was then applied on these cubes, to generate fault surfaces. The resulting faults were then plotted in a rose diagram to detect different trends.

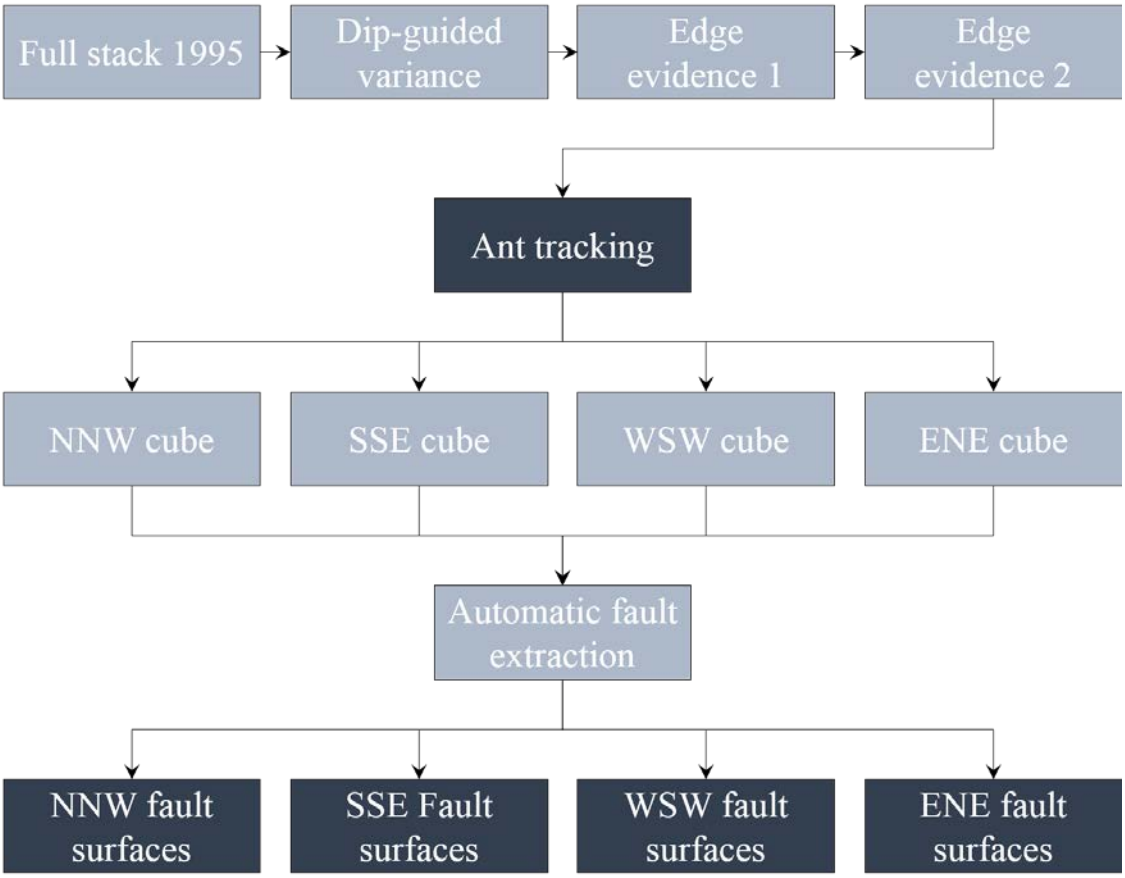


***Figure 5.6**: The ant tracking workflow was applied on the 1995 full stack seismic data. The resulting cube was then cropped into four different cubes, which were used as input to the automatic fault extraction process.*

## 5.3 Rock physics

The rock physics study was conducted based on available well data (Figure 5.8). Acoustic impedance and Vp/Vs ratio was calculated in addition to elastic parameters (i.e., Young's

modulus and bulk modulus), based on the equations described in Table 3.1. As density and P- and S-wave sonic are needed to generate the elastic properties, only the wells with this information were used for the purpose of analysing rock physics (Table 4.2). Once the rock physics properties were generated, the different parameters were cross-plotted in order to observe trends in the data. In addition to studying the discussed rocks physics properties, cross-plots were generated for other well data (i.e., porosity, water saturation and gamma ray). When cross-plotting the properties, the data were filtered to separate the different reservoir intervals.

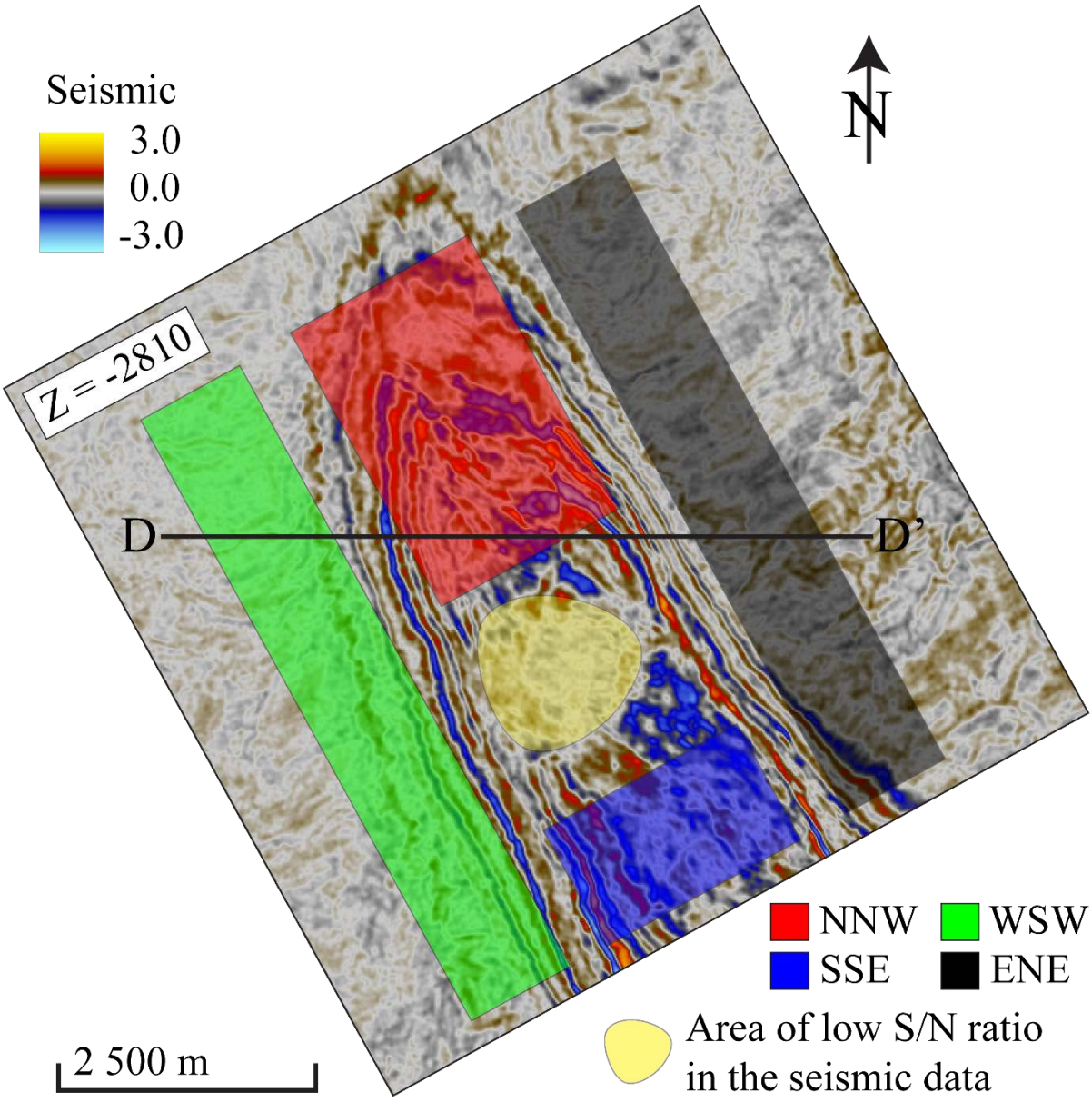


***Figure 5.7**: The approximate lateral location of the cubes used to generate fault surfaces are displayed on a time-slice of the 1995 full stack seismic. A random seismic section (D-D'), which has been used for time-shift, amplitude, and coloured inversion analysis, is also displayed.*

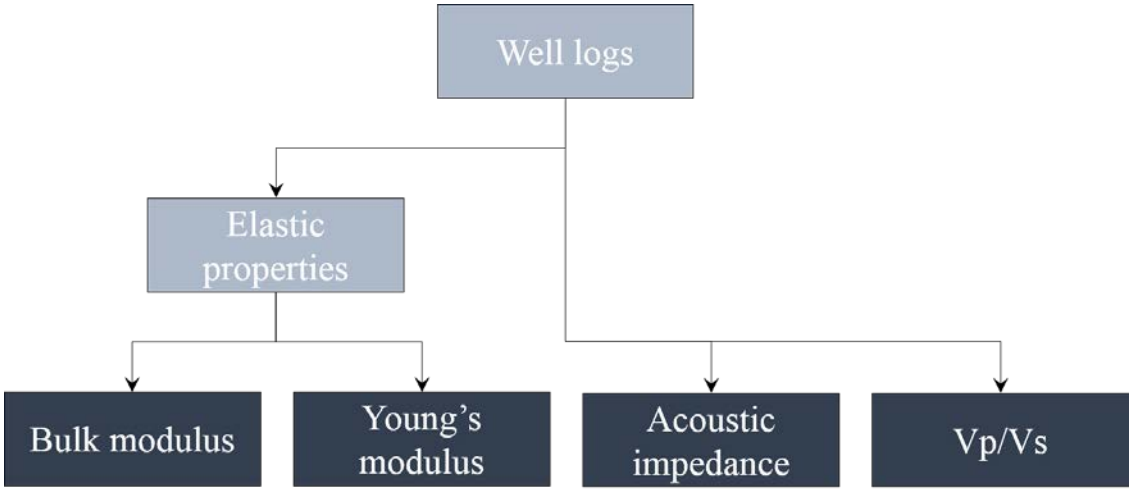


***Figure 5.8**: Rock physics properties were calculated from well data, and cross-plotted to identify trends in the data.*

## 5.4 Structural changes

The analysis of the structural changes in the reservoir was separated into two main topics – the analysis of time-shifts between the seismic surveys to study compaction, and the study of fault reactivation based on differences in the continuity of seismic reflectors.

### 5.4.1 Time-shift

The time-shift analysis was largely based on the time-shift cubes generated from the seismic trace alignment process (Figure 5.4). The cubes that were analysed include time-shifts between 1995 and 2005, and between 1995 and 2011. These results were studied on seismic sections and along seismic surfaces. The time-shifts were extracted as surface attributes on the top reservoir map, in order to analyse the lateral extent of the compaction. This made it possible to compare the time-shift results with the fault analysis. This was done by combining the time-shift map of 1995-2011 with a structure map generated from the variance cube of the 1995 full stack seismic.

The time-shifts were also interpreted in detail on a random seismic section (D-D') (Figure 5.7). On this section, the time-shift between 1995 and 2011 was combined with the original seismic, with the aim to understand the role of signal-to-noise ratio with respect to the time-shift results. In addition, the first derivative of the 1995-2011 time-shift cube was calculated. A seismic section along the navigation D-D' mentioned above was derived from this cube, to understand how the time-shift changed with depth.

In order to understand the causes of compaction, the time-shift between 1995 and 2011 was extracted along the wellbores, and cross-plotted against different rock properties for the Tor Fm. In addition, the compacting rocks were identified in a cross-plot of elastic properties (i.e., bulk and Young's modulus), and compared to uncompacting rocks. This was done by comparing well locations with seismic time-shifts, in order to detect the wells through compacting reservoir rocks.

Based on the cross-plots of time-shift and different rock properties, an interesting well (i.e., well SA-6b) was chosen for a more detailed analysis of rock properties and time-shift. This was done by creating a seismic section of the 1995-2011 time-shift cube along the wellbore of this well, and displaying the porosity well log on top of the section.

### 5.4.2 Fault reactivation

Fault reactivation was studied with the help of the variance attribute, which was applied on the three different full stack seismic surveys (Figure 5.9). The variance cubes were subtracted from each other (i.e., 2005-1995 and 2011-1995), and used as input into the RMS attribute. The resulting cubes were used to generate attribute maps of the top reservoir, where the values were extracted from a small interval within the reservoir (i.e., top reservoir to 10 ms below).

The resulting surfaces were compared with the ant tracking surface of the 1995 survey, in order to understand the cause of the differences in variance response. The surface corresponding to difference in variance between 1995 and 2011 was combined with the 1995-2011 time-shift surface, in order to correlate these results and detect other indications of fault reactivation (i.e., time-shift changes across reactivated faults).

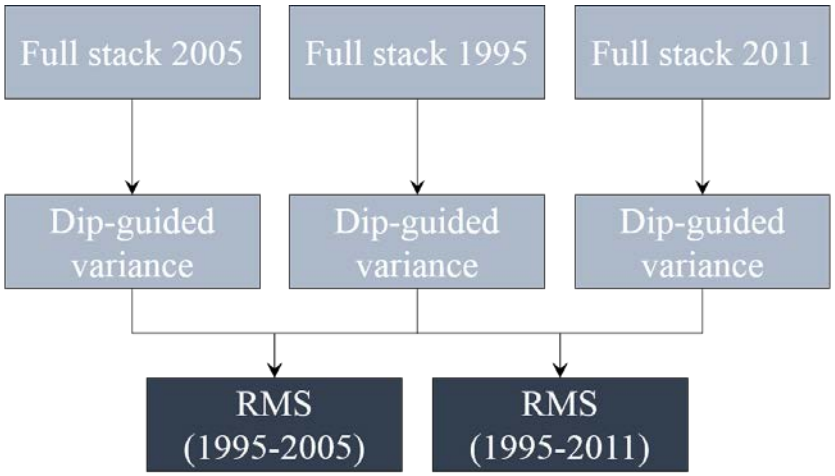


***Figure 5.9**: The workflow used to analyse fault reactivation was mainly based on differences in the result of the variance attribute of the different full stack seismic surveys.*

## 5.5 Amplitude and AVO analysis

The analyses of amplitudes and AVO responses were conducted by first detecting initial anomalies (i.e., pre-production) and then looking at how these anomalies change with production time. Differences in amplitude and AVO response between the different surveys were studied using similar methods. Attributes were applied on the seismic cubes to identify pre-production anomalies, and the differences with production time were examined by subtracting cubes from different surveys.

### 5.5.1 Full stack seismic

Firstly, the original seismic response (i.e., pre-production) of the reservoir was studied based on the 1995 full stack seismic. This was done by extracting the exact amplitude of the top reservoir reflector. In addition, the RMS amplitude was extracted from the reservoir interval (i.e., top reservoir to 60 ms below) (Figure 5.10). The results were displayed as amplitude maps on the top reservoir surface in order to detect anomalies.

Differences in amplitude between the different surveys were analysed by subtracting the full stack seismic cubes from each other (i.e., 2005-1995 and 2011-1995). The resulting difference cubes were used as input to the RMS attribute, and extracted from the reservoir interval. The results were used to generate amplitude maps.

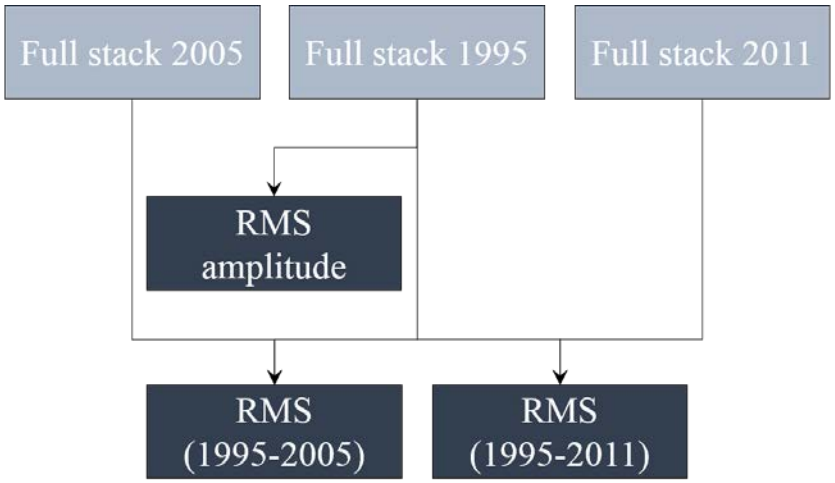


***Figure 5.10**: The full stack amplitude analysis was done by applying the RMS attribute to the difference in amplitude between 1995 and 2005 and between 1995 and 2011, in addition to applying it on the 1995 full stack alone.*

### 5.5.2 AVO

The AVO analysis was conducted in a similar way as the full stack amplitude analysis. The intercept and gradient were calculated from the angle stacks of the three different surveys, using Shuey´s two-term approximations as discussed in chapter 3.3.2 (Figure 5.11). The intercept and gradient of the 1995 survey were studied by extracting the exact amplitudes of the top reservoir reflector and displaying the results as amplitude maps, with the aim to detect AVO effects.

In addition, the intercepts and gradients were multiplied for the three surveys (i.e., 1995 intercept (A) * 1995 gradient (B), etc.) to generate intercept*gradient attribute cubes. These results were analysed for seismic section D-D', in addition to extracting the RMS value from the reservoir interval of the 1995 and 2011 surveys and displaying the results as amplitude maps.

The differences in AVO response were also studied by subtracting the intercept*gradient attribute cubes from each other (i.e., 2005-1995 and 2011-1995). The resulting difference cubes

were used as input to the RMS attribute, and extracted from the reservoir interval. The results were used to generate amplitude maps.

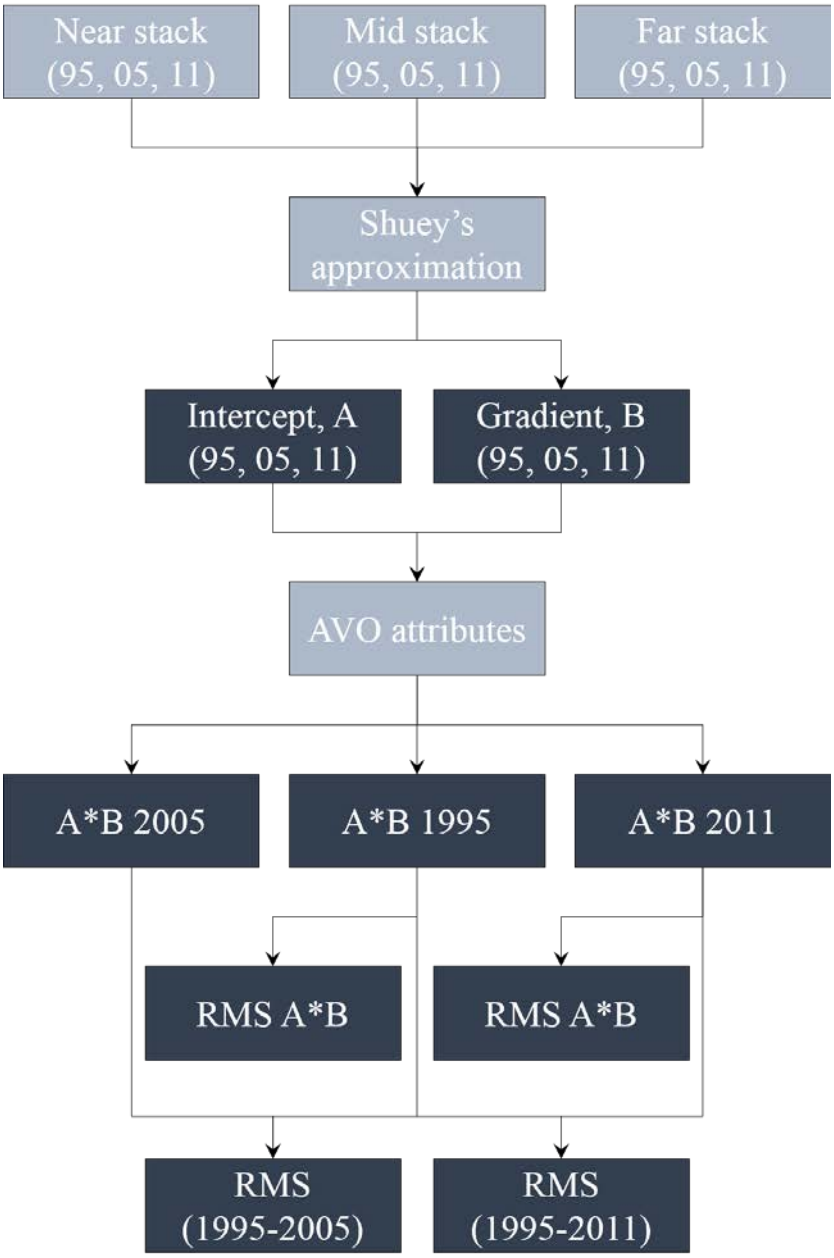


***Figure 5.11**: The AVO analysis was done by computing the intercept and gradient of the three surveys. Then these were multiplied to generate intercept*gradient cubes, and the results were analysed for differences.*

## 5.6 Coloured inversion

Coloured inversion was applied on the full stack seismic of the 1995, 2005, and 2011 surveys (Figure 5.12). This was done by generating an operator based on acoustic impedance from well log data and the 1995 full stack seismic. The operator was then convolved with the three

different full stack seismic surveys, resulting in three colour inverted cubes assumed to represent relative acoustic impedance.

The difference in acoustic impedance was then studied by subtracting coloured inversion results from each other (i.e., 2005-1995 and 2011-1995). The result should represent relative differences in acoustic impedance. These difference cubes were studied for section D-D', in addition to generating a horizon probe for the reservoir interval of the difference between 1995 and 2011. The horizon probe uses a volume rendering technique to create a seismic volume based the geometry of the input surface and a defined interval.

The colours of the horizon probe were adjusted to identify hardening effect in the reservoir, and the results were studied in map view. The horizon probe was also studied together with the ant tracking map of the 1995 survey, in order to detect the influence of faults on changes in acoustic impedance with time.

In addition, these results were compared with the 1995-2011 time-shift results. This was done by creating a horizon probe from the time-shift cube based on the same interval as the hardening horizon probe, and comparing the two probes in 3D while displaying the production and injection wells.

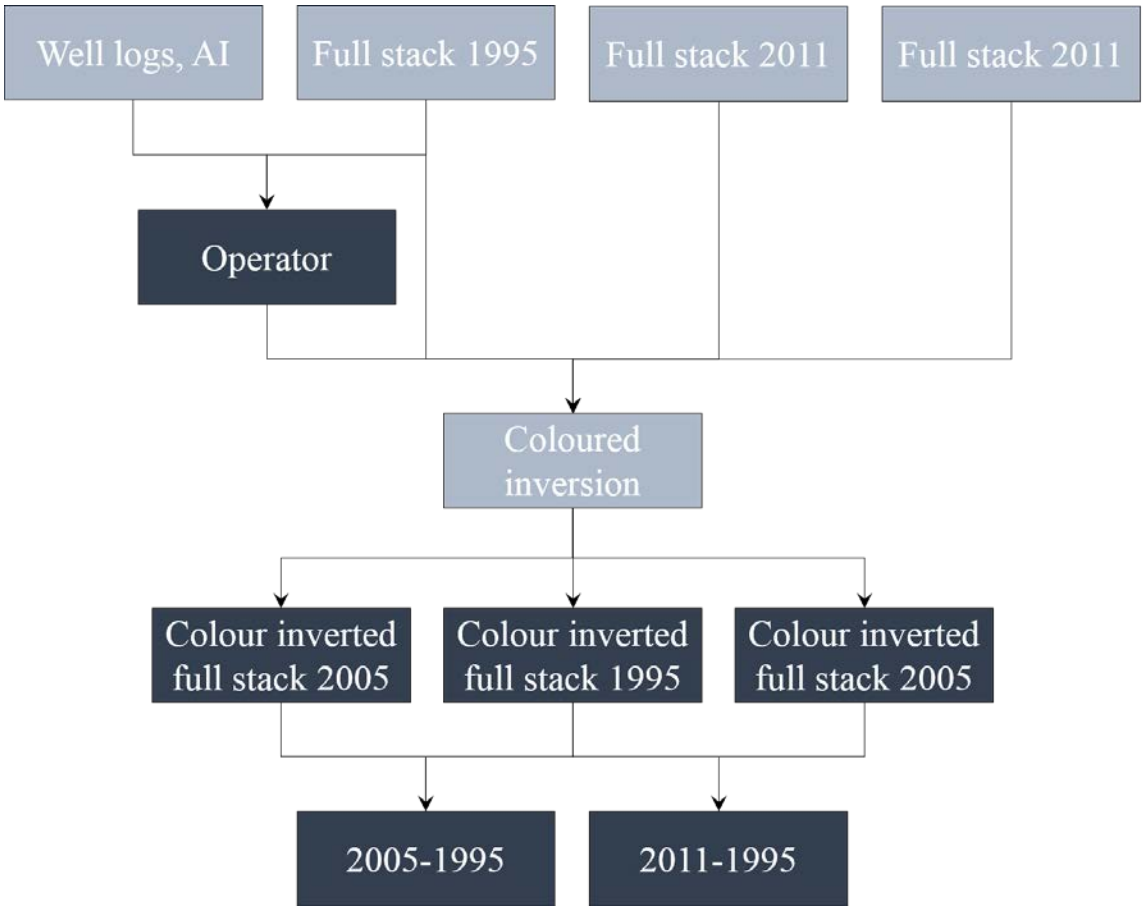


***Figure 5.12**: The coloured inversion was conducted by generating an operator based on well log data and the full stack seismic of the 1995 survey. This operator was then convolved with the 1995, 2005, and 2011 full stack seismic surveys, and the results were subtracted from each other detect differences.*

# 6. Results

## 6.1 Seismic QC and conditioning

As discussed above, the seismic QC was done using two surfaces (A and B) and a cropped volume (C) (Figure 5.2). The results are presented below.

### 6.1.1 Time-lapse seismic (full stack)

Figure 6.1 shows the difference in elevation of the same surfaces interpreted on the different full stack surveys, and Figure 6.2 shows the different surface elevations cross-plotted against each other.

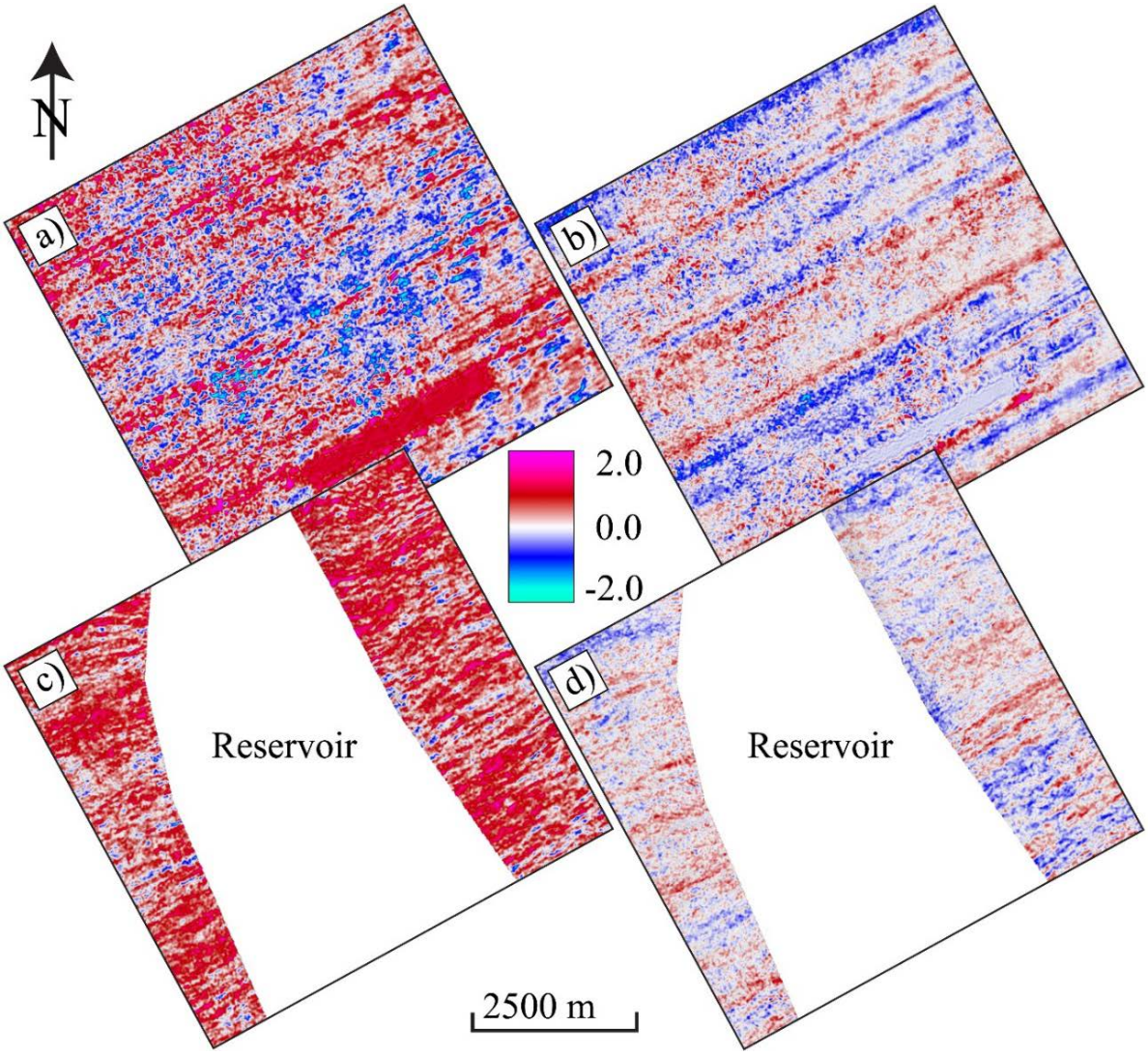


***Figure 6.1**: Difference in elevation of the full stack seismic between the different surveys. Surface A is shown in a) and b), and surface B in c) and d). The time-shifts between the 1995 and 2005 surveys are shown in a) and c) and the time-shifts between 2005 and 2011 are shown in b) and d). The colours represent values of difference in TWT (ms).*

There is clearly a larger difference between the 1995 and 2005 surveys, than between the 2005 and 2011 surveys. It is also evident that there is a decrease in elevation difference with depth (i.e., larger difference on surface A than B), and on Surface B there is almost a constant positive time-shift of about 0.5-1.5 ms TWT between 1995 and 2005. Another interesting observation is a strong ENE-WSW trend, interpreted to represent acquisition noise. This trend, however, becomes less dominant with depth, indicating that the interpretations at reservoir level are more reliable than at shallower depth.

Although the differences are not major issues, they need to be corrected for, because the study is largely based on comparing the different seismic cubes. Without aligning them, there is a big risk that incorrect features of the seismic data are compared, causing unreliable interpretations.

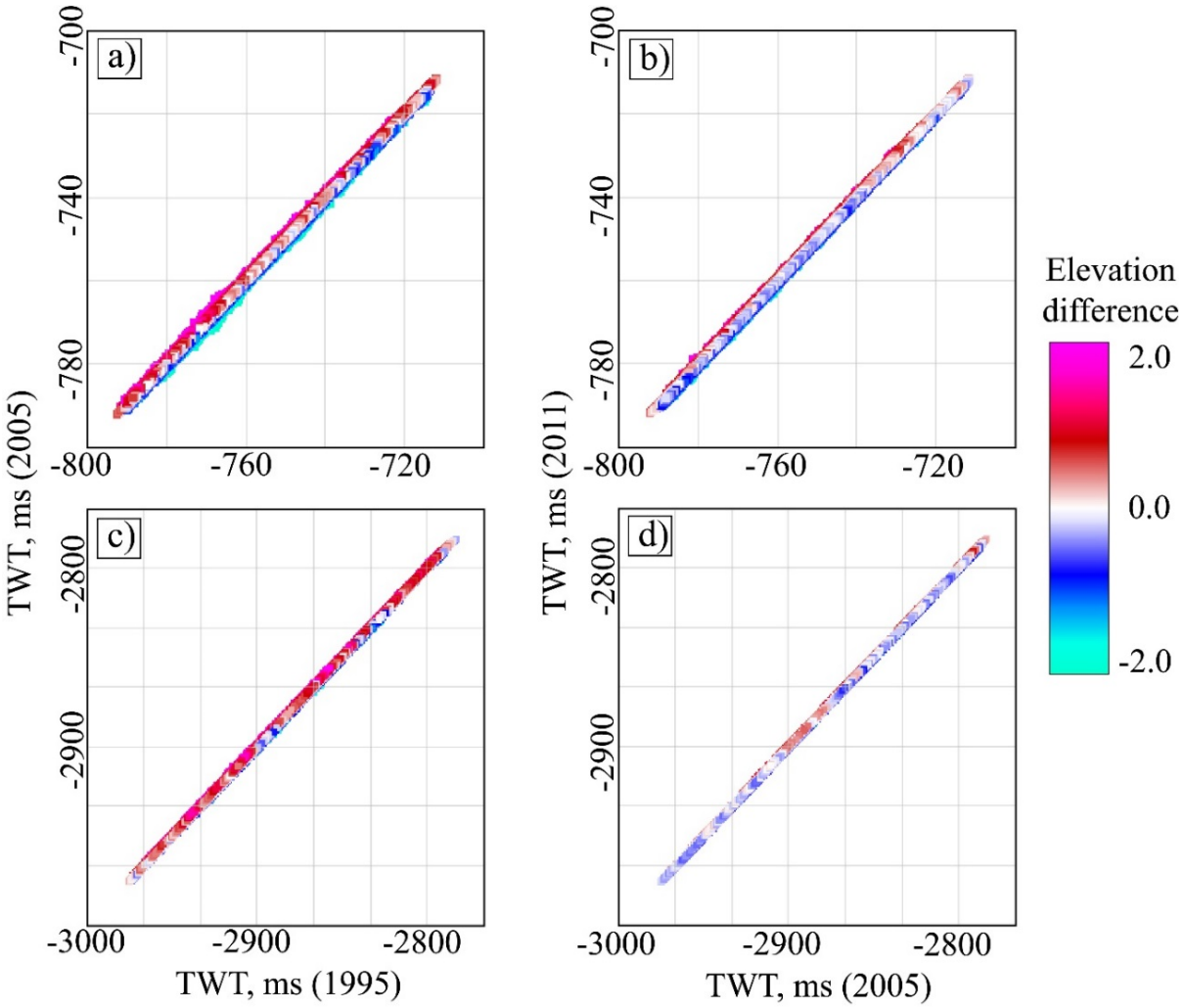


***Figure 6.2**: Cross-plots of the elevation of the same surfaces interpreted on the different full stack seismic surveys. Elevations of Surface A interpreted on the different surveys are cross-plotted in a) and b), and the elevations of Surface B are cross-plotted in c) and d). Interpretations on the 2005 survey is plotted against interpretations on the 1995 survey in a) and c), and interpretations on the 2011 survey is plotted against interpretations on the 2005 survey in b) and d). The colours represent values of difference in TWT (ms).*

The results of the QC on Surface B after the application of the seismic trace alignment process on the time-lapse seismic is displayed in Figure 6.3. There is an overall decrease in difference compared to the data before seismic trace alignment; however, some large value differences

are observed, with a somewhat E-W trend. These anomalies represent noise induced by the seismic trace alignment process, and this noise should be kept in mind when running the amplitude analysis. Although the overall result of the seismic trace alignment is a decrease in elevation difference between the surveys, the trend observed in the cross-plots might appear smoother before the application of seismic trace alignment. This is also a result of the noise caused by the seismic trace alignment.

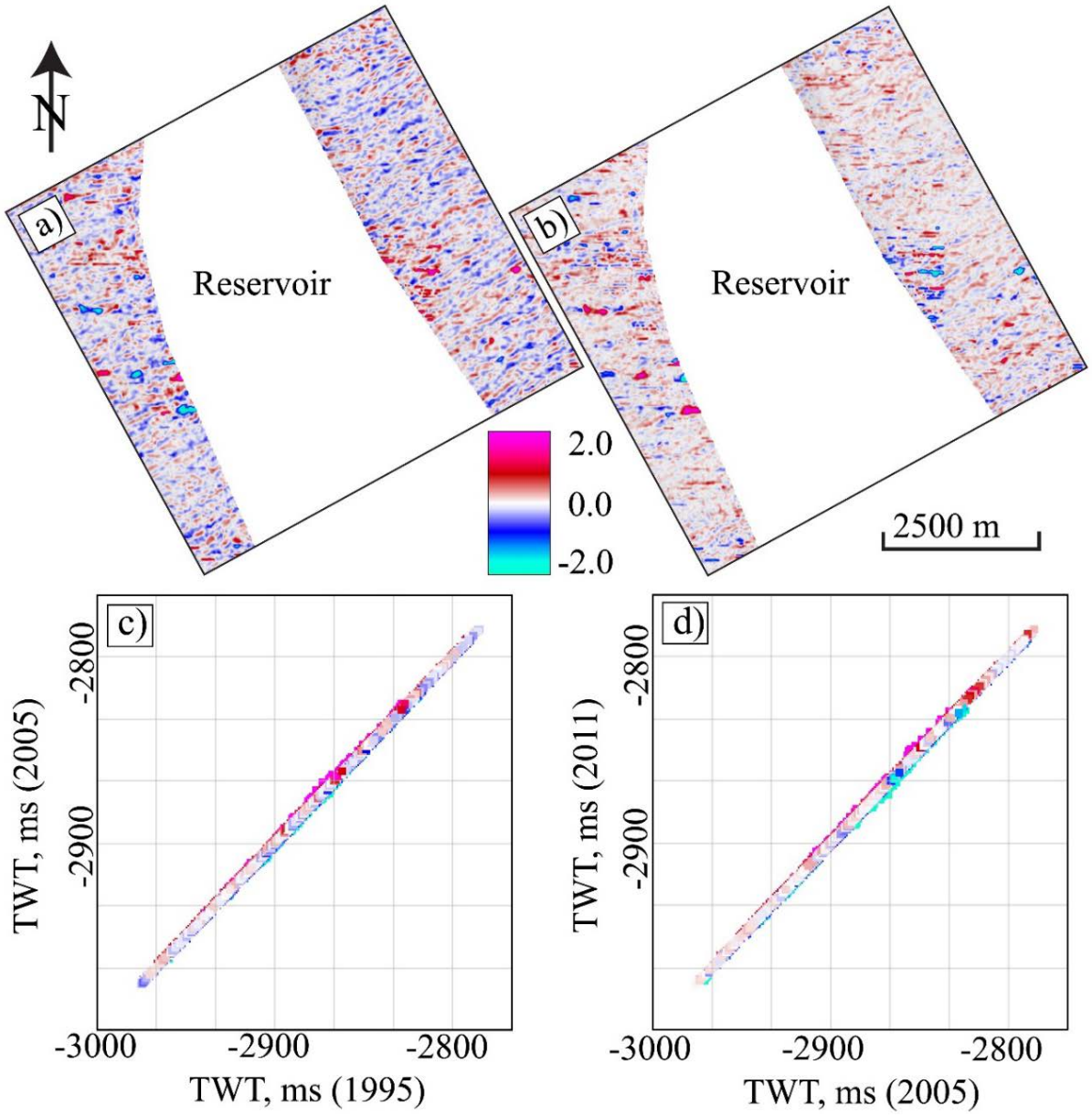


***Figure 6.3**: Full stack seismic time-shifts of Surface B after trace alignment. The difference in elevation between 1995 and 2005 is displayed in a), and between 2005 and 2011 in b). The elevations are cross-plotted in c) and d). The colours represent values of difference in TWT (ms).*

The differences in amplitude of the same surfaces interpreted on the different full stack surveys are displayed on the surfaces in Figure 6.4, and the amplitudes of the different surfaces are cross-plotted against each other in Figure 6.5. As with the time-shifts, a larger amplitude difference is observed between the 1995 and 2005 surveys, than between the 2005 and 2011

surveys. The large amplitude differences at Surface A are probably results of differences in acquisition noise of the surveys.

For the amplitudes, the differences decrease with depth, and the same acquisition induced ENE-WSW trend is observed. At reservoir level (i.e., Surface B), no major problems are detected, meaning the differences are acceptable in terms of the comparison of time-lapse data. This is especially true since the amplitude analysis mainly detects anomalies, and the observed differences are small and seem to be fairly constant along the discussed trend.

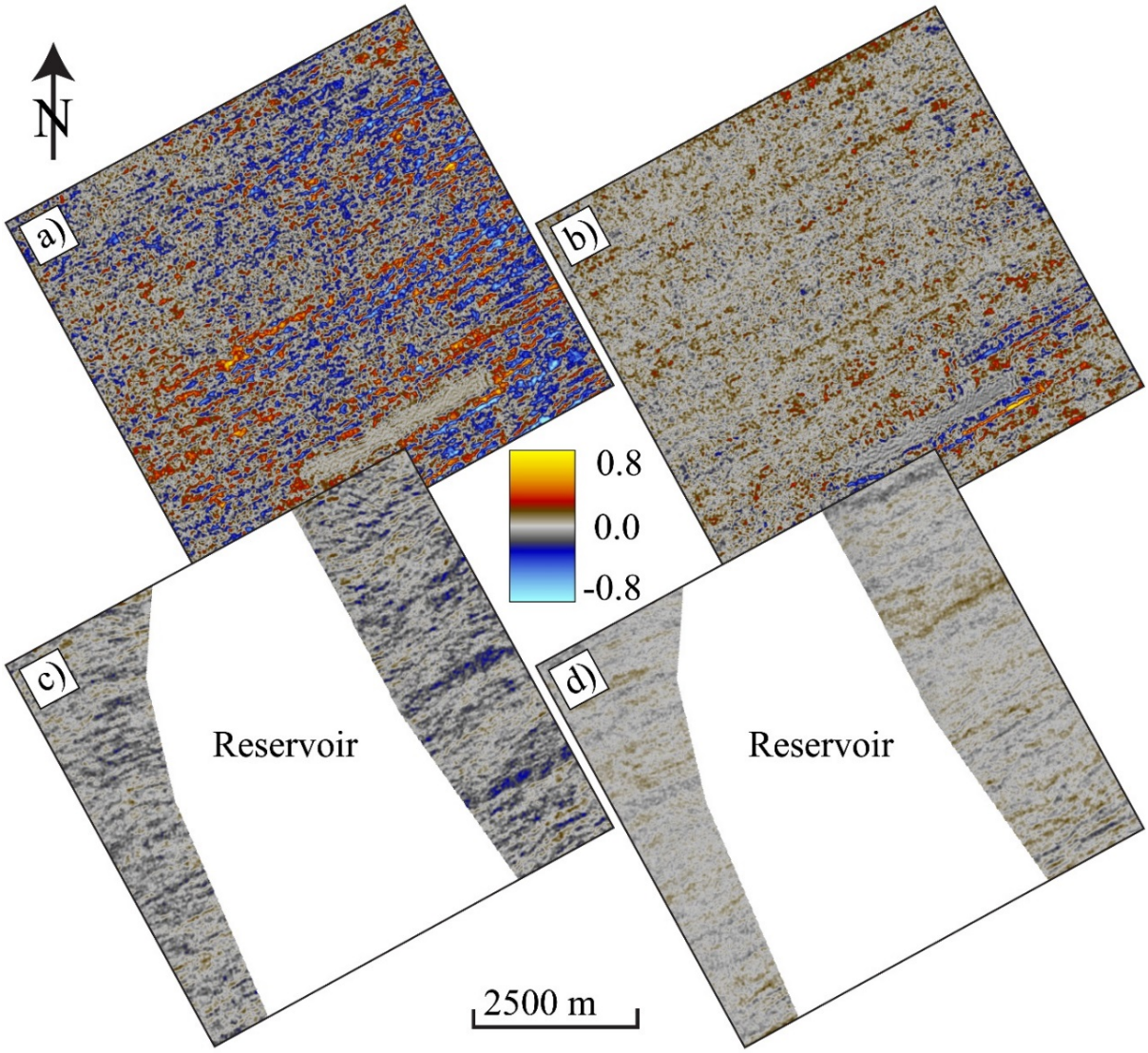


***Figure 6.4**: Difference in amplitude of the full stack seismic between the different surveys. The difference at Surface A is shown in a) and b), and at Surface B is shown in c) and d). The amplitude difference between the 1995 and 2005 surveys are shown in a) and c) and the difference between 2005 and 2011 are shown in b) and d). The colours represent values of difference in amplitude.*

The frequency content of the three full-stack seismic cubes are displayed in Figure 6.6. Generally, as for the amplitude and elevation differences, the main variations in frequency content are observed when comparing the 1995 survey with the two other surveys. There are very little differences between the 2005 and 2011 surveys.

Although some differences are observed overall, they are assumed to be relatively insignificant and should not influence the outcome of the study. This means that no frequency conditioning is required.

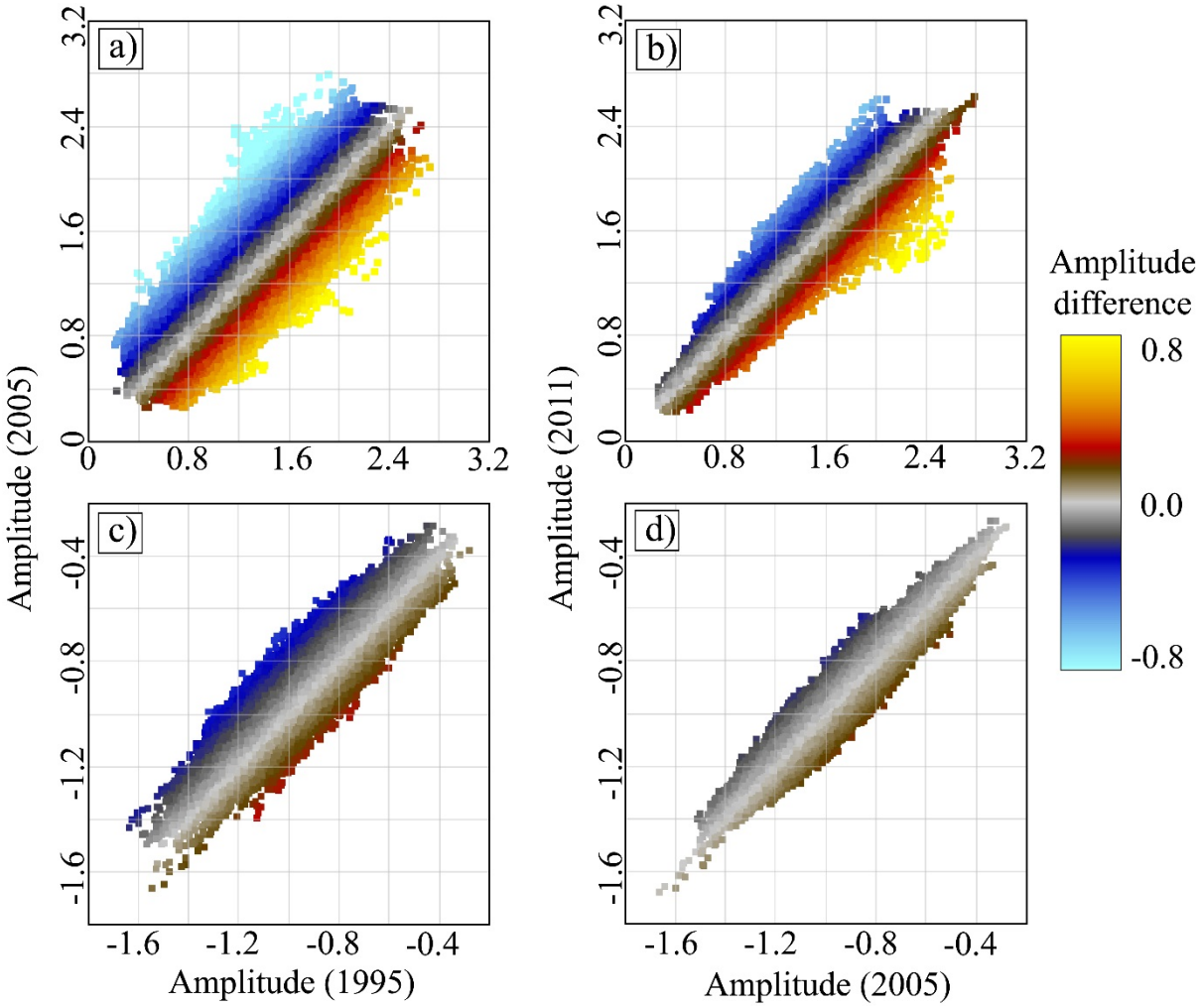


***Figure 6.5**: Cross-plots of the amplitudes of the same surfaces interpreted on the different full stack seismic surveys. Amplitudes of Surface A interpreted on the different surveys are cross-plotted in a) and b), and the amplitudes of Surface B are cross-plotted in c) and d). Interpretations on the 2005 survey is plotted against interpretations on the 1995 survey in a) and c), and interpretations on the 2011 survey is plotted against interpretations on the 2005 survey in b) and d). The colours represent difference in amplitude.*

### 6.1.2 Angle stacks

Figure 6.7 shows the difference in elevation of the same surfaces (A and B) interpreted on the near and far stacks of the 1995 survey. The differences seem to be quite significant, with time-shifts of about 3-5 ms TWT dominating surface A and several small areas of time-shifts approaching and larger than -5 ms TWT on surface B. For the angle stacks, it seems the elevation differences increase with depth, and the large differences at reservoir level indicate that a seismic trace alignment process is necessary.

Figure 6.8 displays the result of the QC on Surface B after the application of the seismic trace alignment process for the angle stacks. A clear improvement is observed. The differences are now randomly distributed, mainly in the range of -3-3 ms TWT.

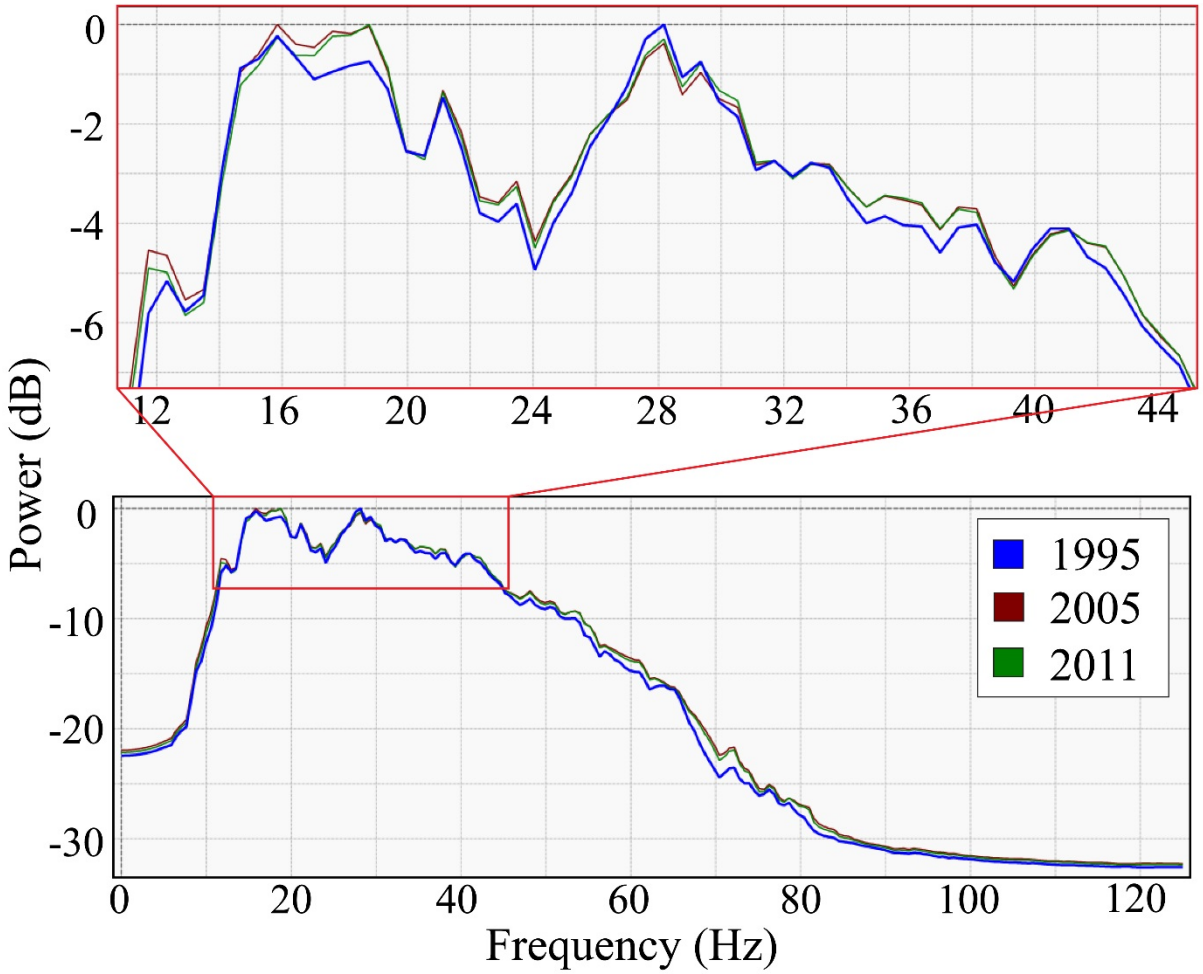


***Figure 6.6**: Frequency content of the different full stack seismic surveys extracted from the cropped seismic volume, Cube C.*

The frequency content of near and far stacks of the 1995 survey is displayed in Figure 6.9. No major issues are observed. The main differences are that the far stack lacks the high-frequency content that the near stack contains. This is expected, because of the increased wavelet stretching as consequence of the NMO (normal moveout) correction (i.e., correction for the difference in travel times of the same seismic event, caused by different offsets) performed in the seismic data processing centre. A correction is very difficult or impossible and would be part of seismic processing.

The difference in amplitude between the near and far stacks of the 1995 survey is displayed in Figure 6.10. On Surface A, the differences seem randomly distributed. The differences are more uniformly distributed on Surface B, where the near stack generally has larger negative amplitudes compared to the far stack.

Great care is required when interpreting these differences, as they are closely related to AVO effects and do not necessarily represent data issues. With this in mind, the amplitude behaviour

of surface B is expected where no major AVO effect is encountered, and further amplitude conditioning is not necessary.

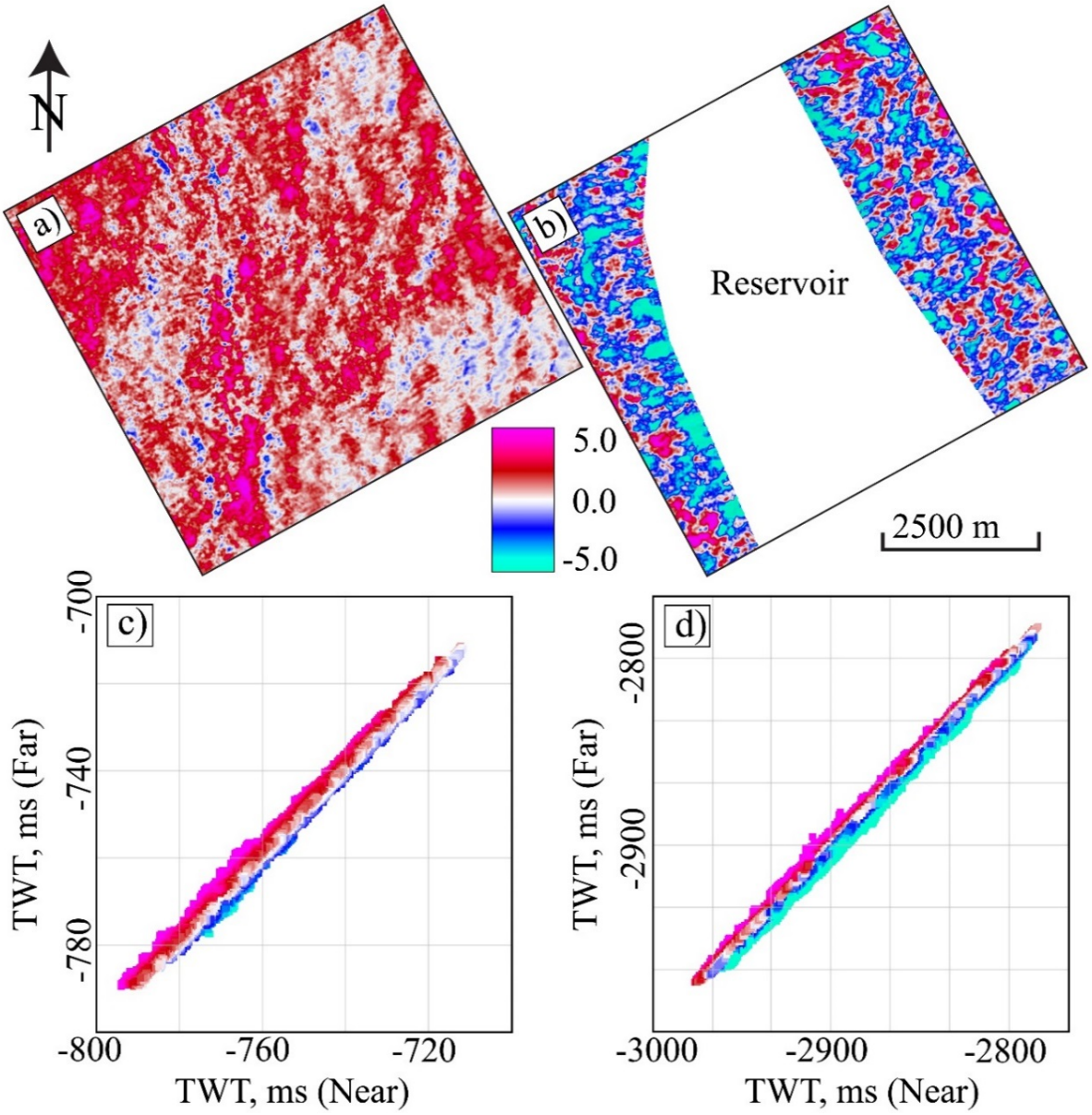


***Figure 6.7**: Difference in elevation of the near and far stacks of the 1995 survey. The difference at Surface A is shown in a) and at Surface B in b). The elevations of Surface A are cross-plotted against each other in c), and d) represents the elevations of Surface B. The colours represent values of difference in TWT (ms).*

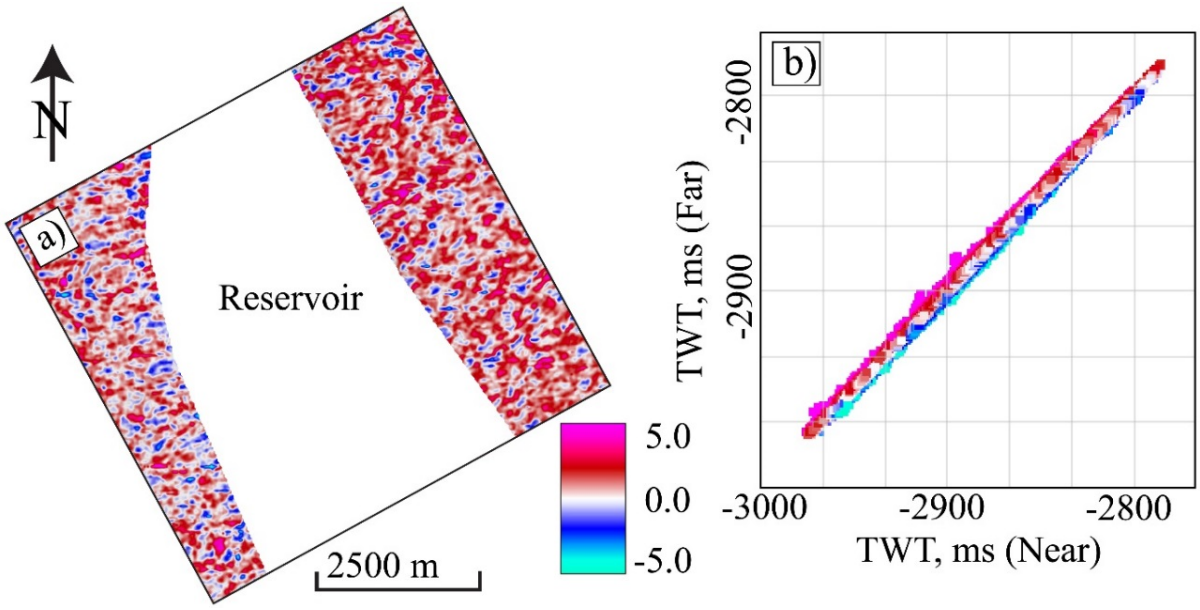


***Figure 6.8**: Difference in elevation of the near and far stacks of the 1995 survey after trace alignment. The differences are shown on Surface B in a), and the elevations are cross-plotted against each other in b). The colours represent values of difference in TWT (ms).*

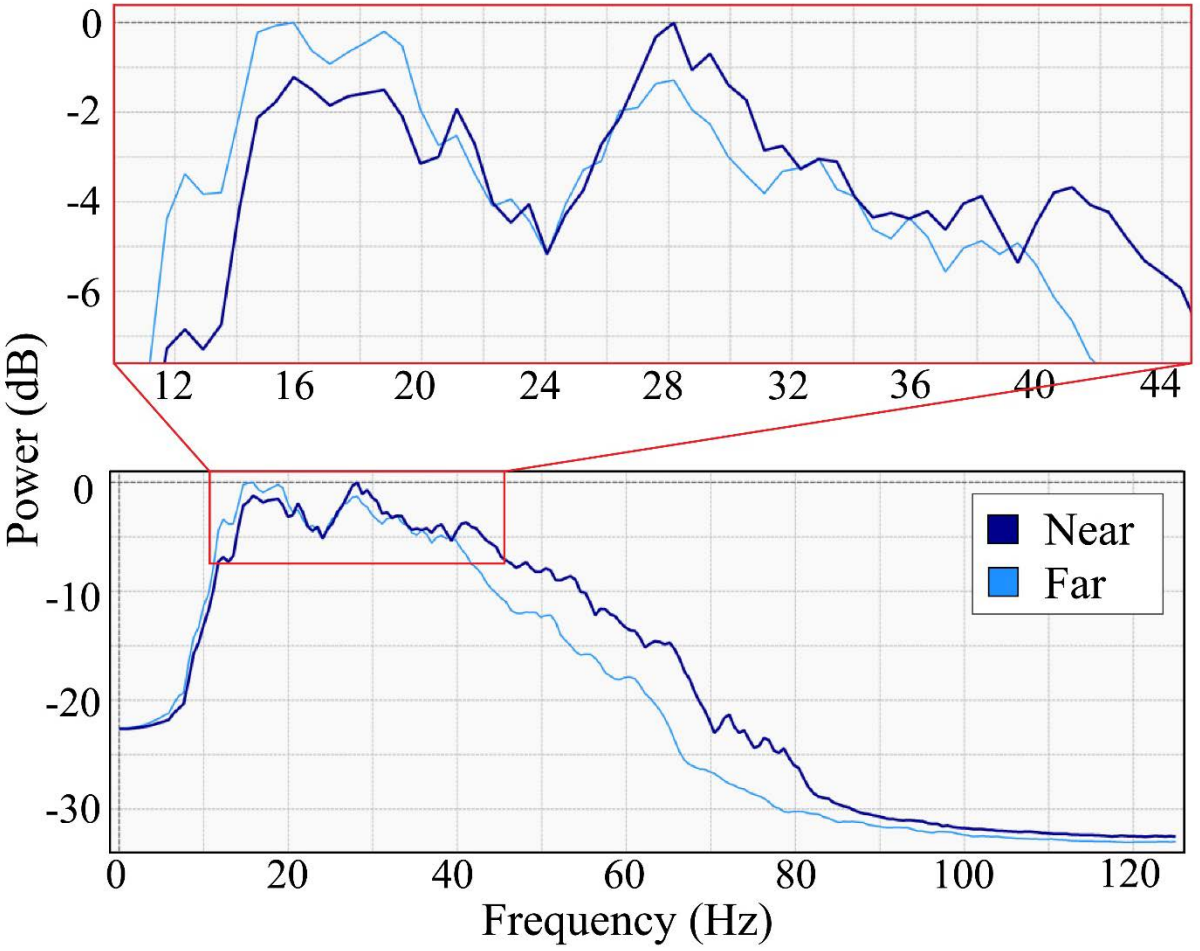


***Figure 6.9**: Frequency content of the near and far stacks of the 1995 survey extracted from the cropped seismic volume, Cube C.*

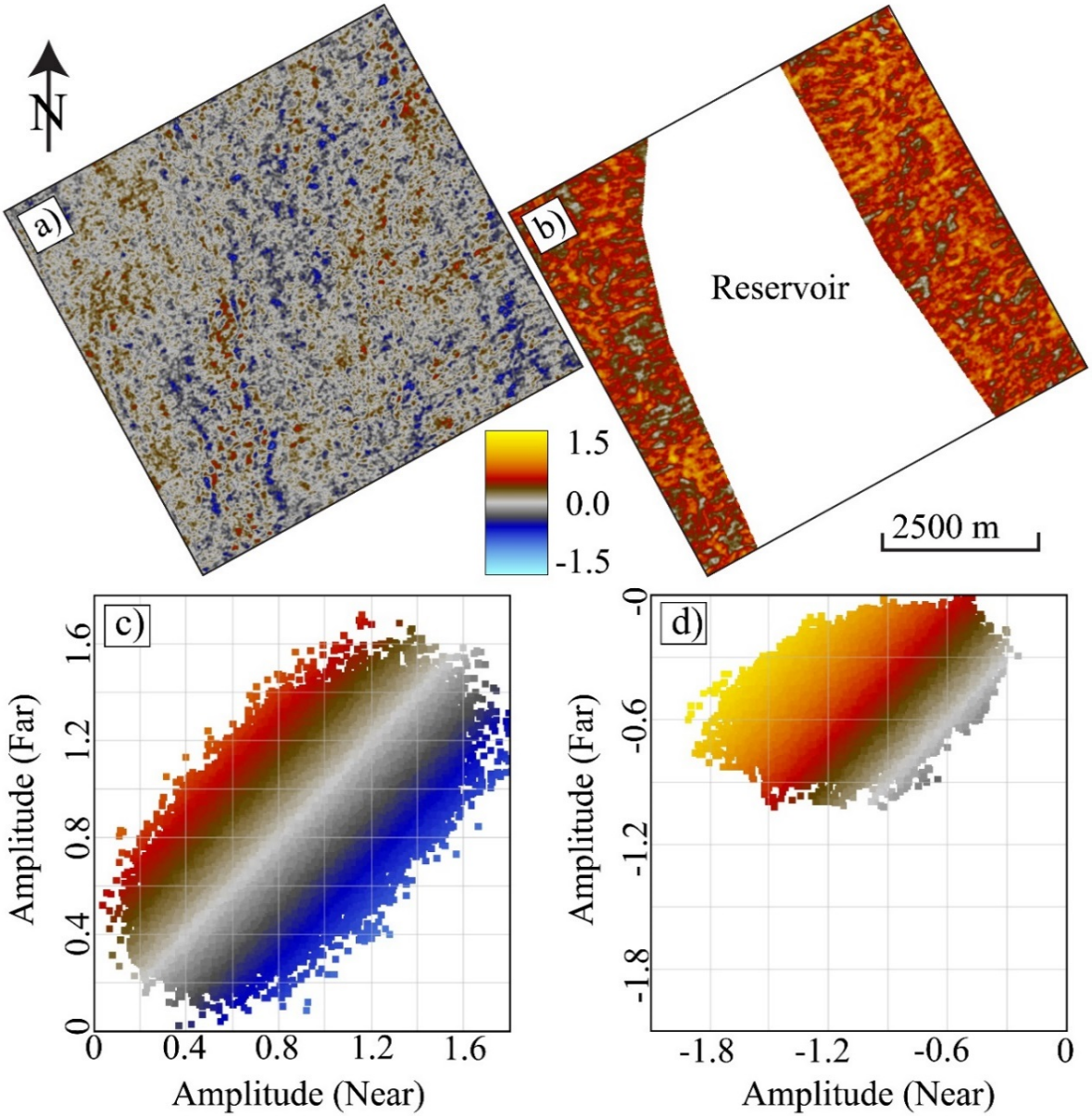


***Figure 6.10**: Difference in amplitude between the near and far stacks of the 1995 survey. The difference at surface A is shown in a) and the corresponding amplitudes are cross-plotted in c). Surface B is represented in b) and d).*

## 6.2 Reservoir overview

An overview of the seismic data and some of the results are given by Figure 6.11. It shows the approximate location of the reservoir and high RMS amplitude values interpreted to represent the gas cloud. A low signal-to-noise ratio affecting an area of the seismic data at reservoir level is due to the gas cloud reflecting most of the seismic energy. Therefore, no proper interpretation can be conducted below the gas cloud. The negative time-shift between 1995 and 2011 is also displayed in 3D, and this is further discussed in chapter 6.4.1.

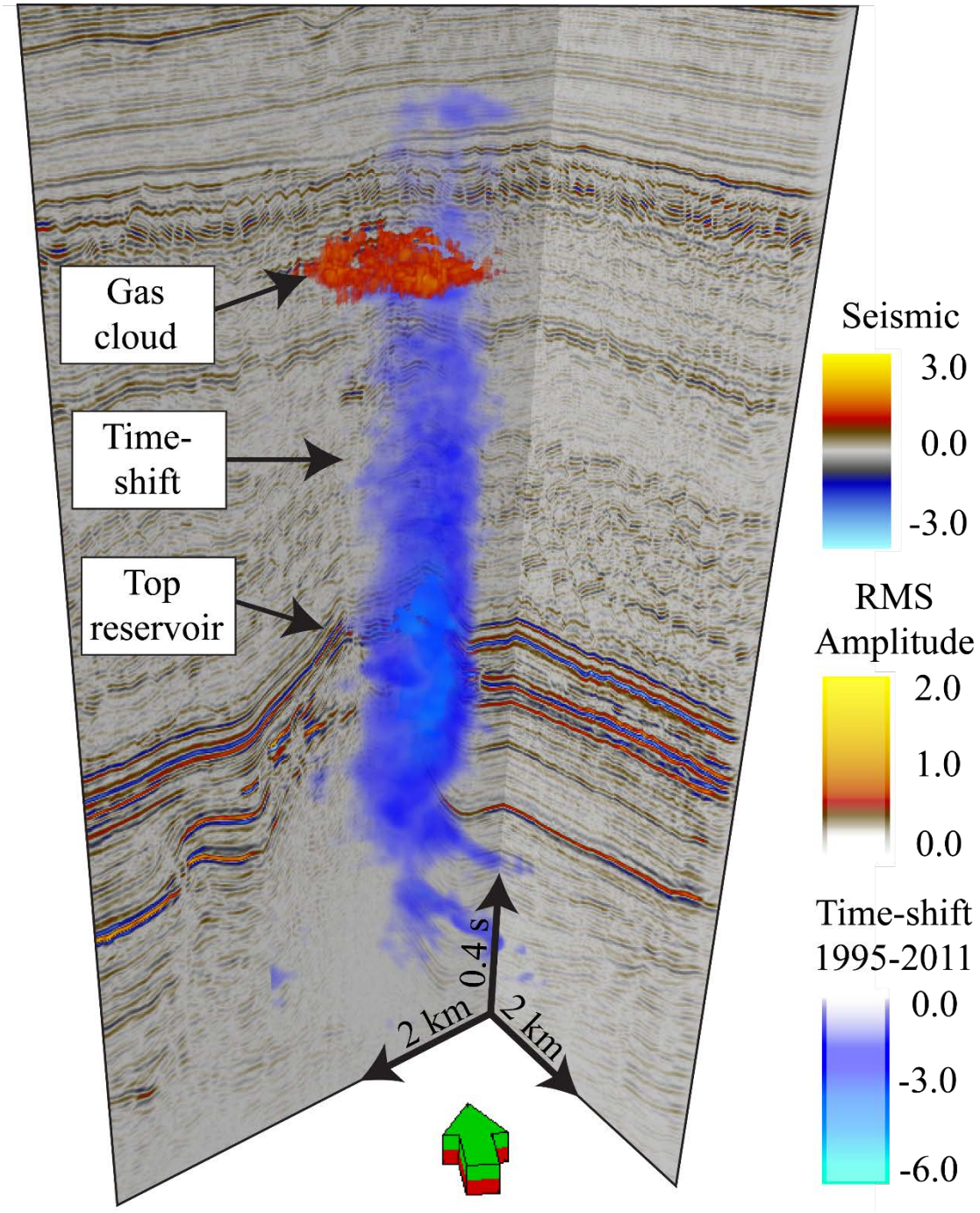


***Figure 6.11**: 3D view of an inline and crossline of the 1995 full stack seismic, displayed together with the extracted negative time-shift between 1995 and 2011 and the gas cloud extracted based on high RMS amplitude values of the 1995 full stack seismic.*

### 6.2.1 Structure

The South Arne field is located in an elongated anticline trending NNW-SSE (Figure 6.12). The anticline widens and increases in elevation towards the SSE, and it loses relief and dies out towards the NNW. In the NNW part, the limb on the ENE part of the anticline dips more steeply than the limb on the WSW part. This relationship is opposite in the SSW part of the

anticline. Note that the main production area, as indicated by the production and injection wells, is just north of the gas cloud area.

Based on seismic well ties, the top Ekofisk Fm is identified as a soft event in the seismic data (Figure 6.13). The same is true for the reflector of the top Tor Fm, whereas the base reservoir is identified as a hard event. The amplitudes of the reservoir are further discussed in chapter 6.5. Due to very thin reservoir units at several locations, the different reservoir zones are not mapped for the whole reservoir.

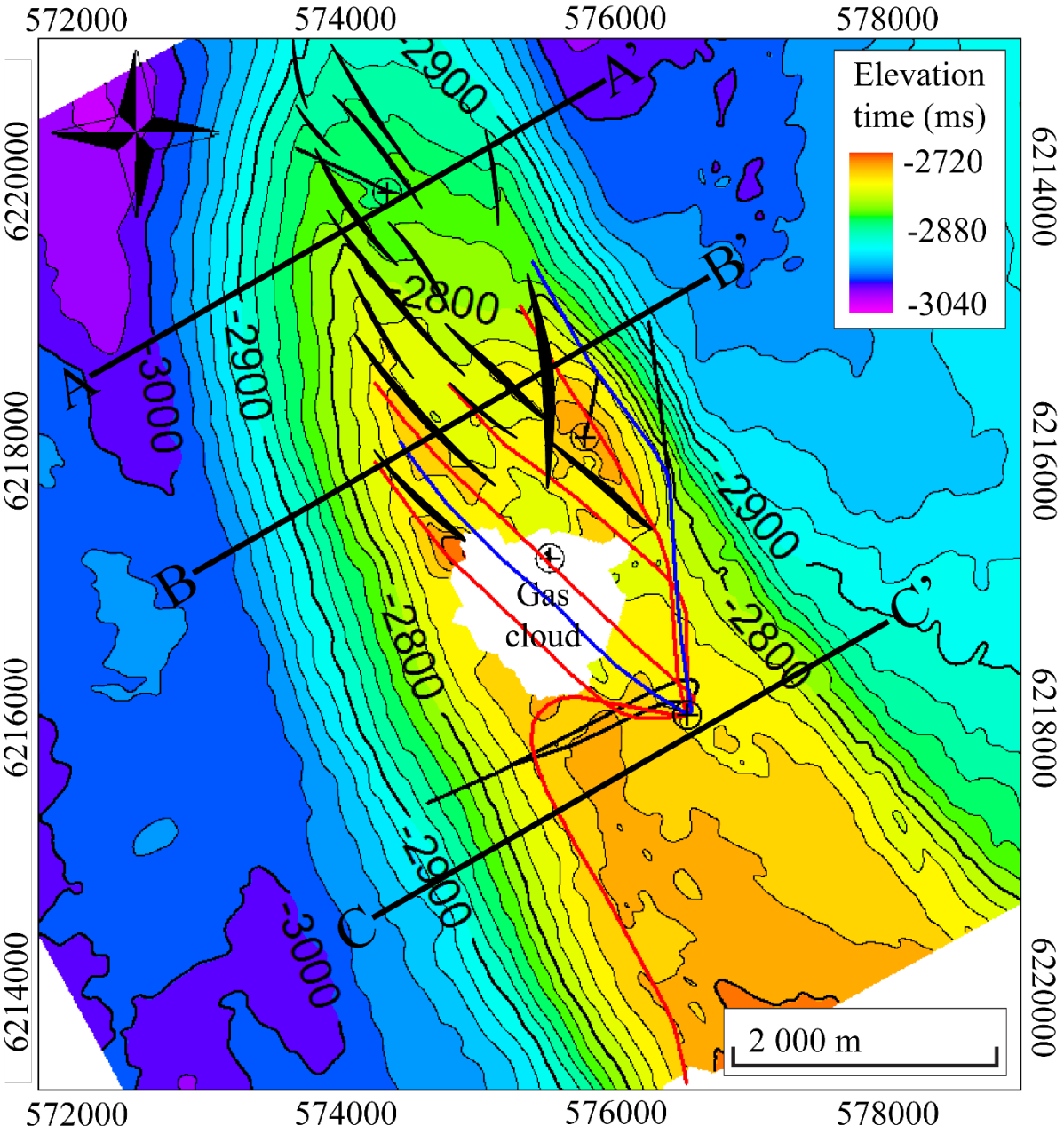


***Figure 6.12**: Time-structure map of the top reservoir (i.e., top Ekofisk Fm) reflector with major faults in black. The producers (red) and injectors (blue) drilled before 2011 are displayed together with exploration and appraisal wells in black. The location of the seismic sections A-A', B-B', and C-C' in Figure 6.13 are also shown.*

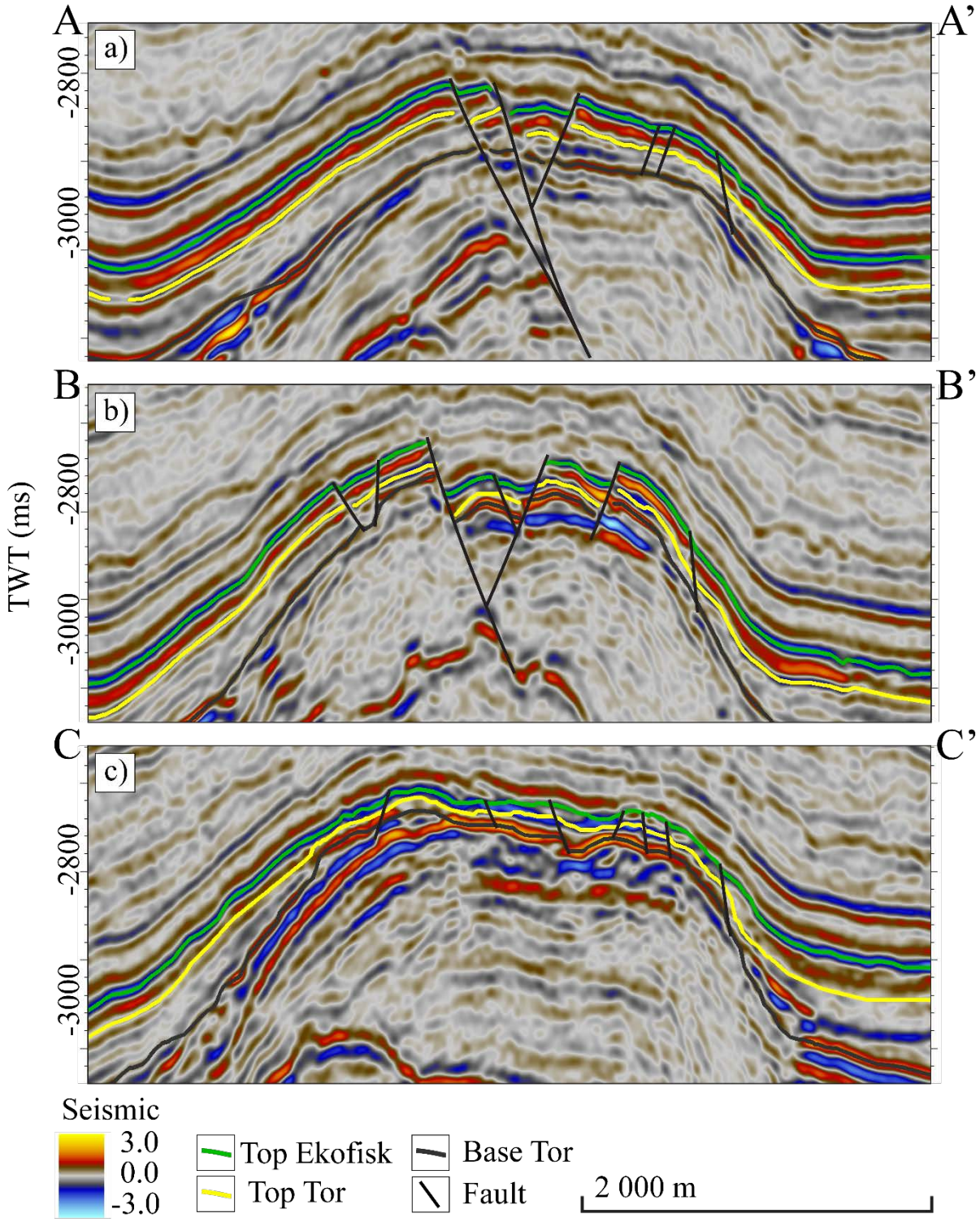


***Figure 6.13**: Interpretation of seismic sections A-A' (a), B-B' (b), and C-C' (c) covering the reservoir.*

Based on the seismic interpretations in Figure 6.13, the thicknesses of the reservoir units generally increase towards the NNW. In addition, the Tor and Ekofisk fms increase in thickness away from the anticline (i.e., towards the ENE and WSW). In the NNW part of the anticline, a graben structure is observed. This structural feature is most prominent just north of the gas cloud area and a decrease in fault displacement towards the NNW is observed. This is evident

from studying the elevation differences across faults in Figure 6.12 and comparing seismic sections A-A' and B-B' in Figure 6.13. In the SSW part of the anticline, no major faults are observed. However, minor discontinuities in the seismic amplitudes are interpreted to represent minor faults with very small displacements.

Figure 6.14 shows the top reservoir structural map based on ant tracking and dip illumination. The ant tracking results are assumed to represent faults, and the trends of these features are plotted in the rose diagram in Figure 6.15. The main fault trend in the reservoir is between NNW-SSE and NW-SE, but a minor E-W trend is also observed. The main trend is most noticeable in the NNW part of the anticline. The same trend is also observed in the SSE part; however, this area yields weaker and more chaotic ant tracking response. Outside the anticline, the main trend is WSW-ENE (i.e., perpendicular to the trend of the anticline), and a minor trend similar to the areas within the anticline is also observed.

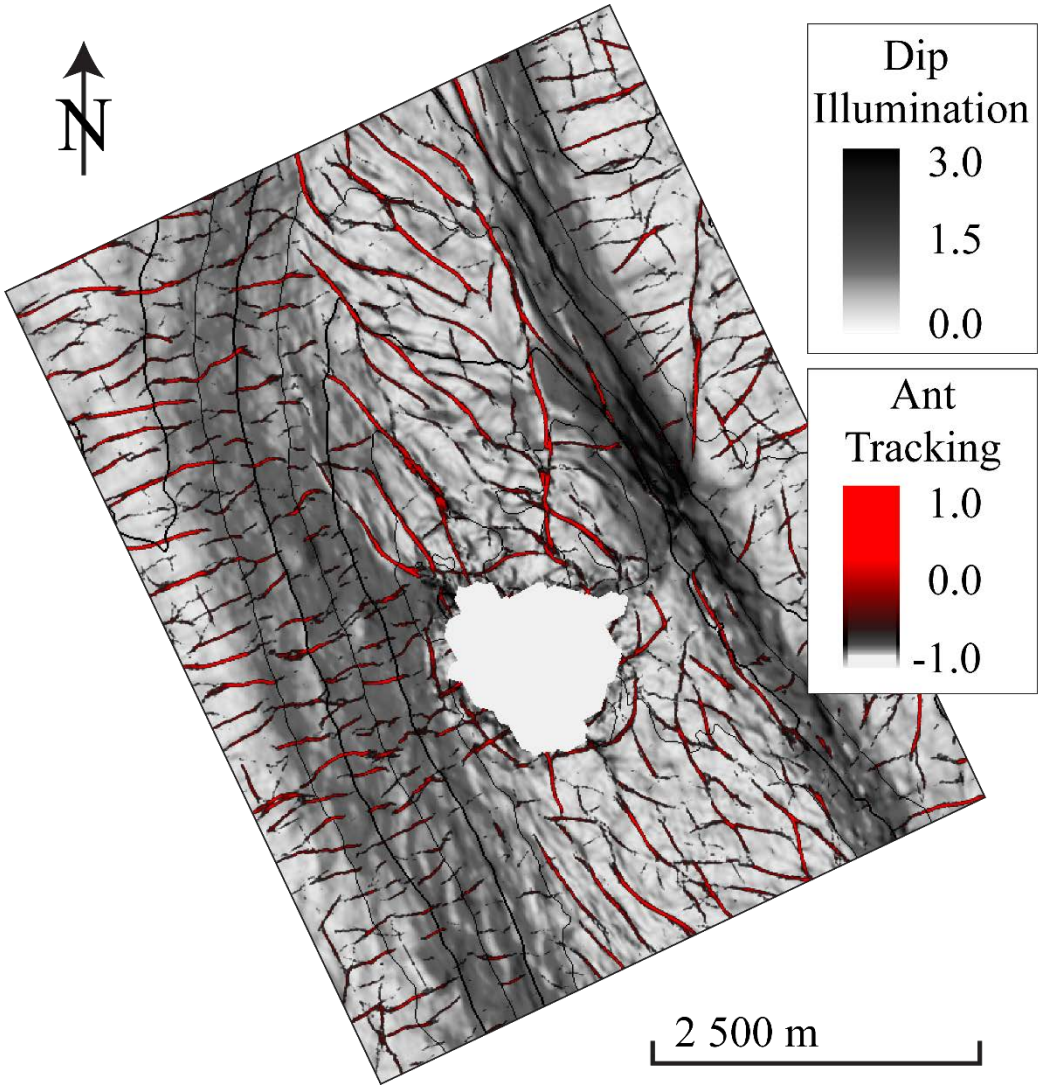


***Figure 6.14**: Top reservoir structural map based on the ant tracking results and dip illumination. The ant tracking is assumed to represent faults and fracture zones, and the dip illumination highlights steeply dipping reflectors.*

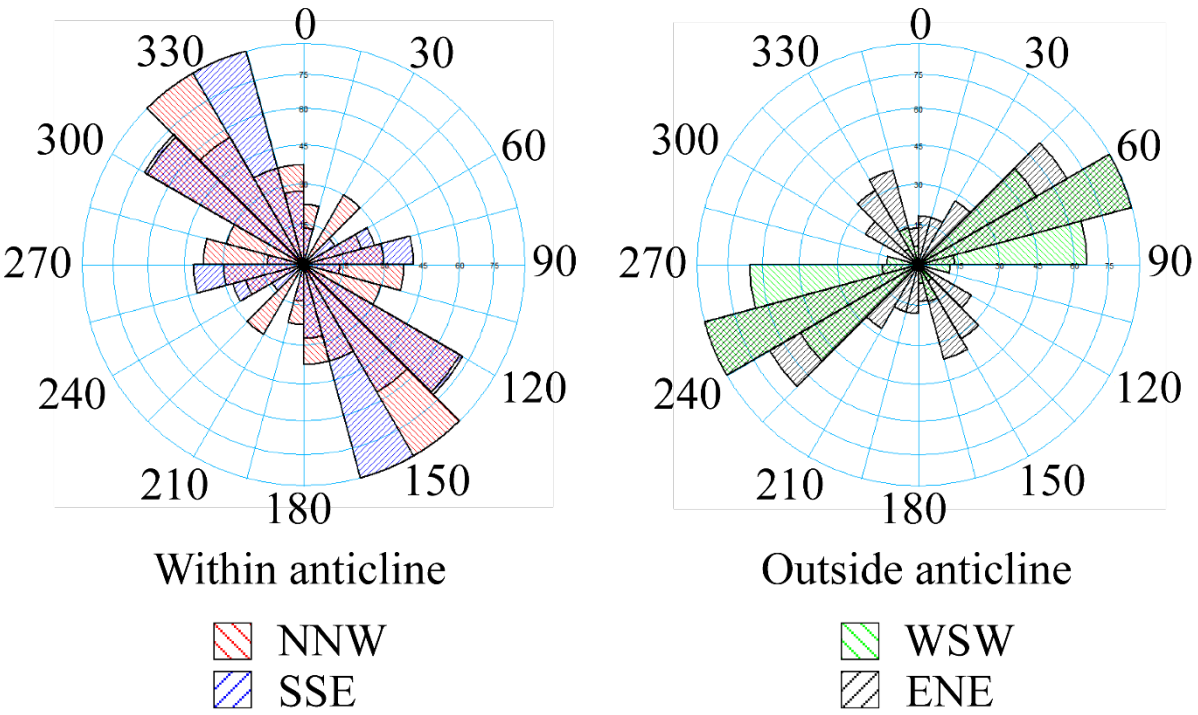


***Figure 6.15**: Rose diagram of the fault surfaces extracted from the ant tracking results, showing different trends for the different areas within and outside the anticline.*

### 6.2.2 Stratigraphy

Well interpretations of the chalk reservoir units (i.e., the Tor and Ekofisk fms) are shown in Figure 6.16. A summary of the interpreted well log response of the reservoir, including the different reservoir units and the tight zone between the Ekofisk and Tor fms, is given as follows:

- Gamma ray (GR) readings are lower for the chalk compared to the over- and underburden and the tight zone. In addition, higher GR values are observed for rocks of high reservoir quality compared to rocks less favourable for oil production.
- The density-neutron combination (ρ, φN) delivers close to zero separation for water saturated chalk, and a negative separation for oil filled reservoir rocks. The over- and underburden are represented by a positive separation.
- The acoustic impedance (AI) is lower for chalk than the over- and underburden and the tight zone, given that the reservoir contains oil.
- The use of porosity (φ) and water saturation (Sw) logs are self-explanatory in that they indicate the quality of the reservoir rocks.

The highest reservoir quality is observed for the Tor Fm in the main production area just north of the gas cloud (i.e., well Rigs-2). This area yields porosities of about 45 % and very low water saturation (i.e., <5 %). In this area, the Ekofisk Fm also shows acceptable reservoir quality with high porosities (i.e., about 40 %) and water saturation of about 5-10 %.

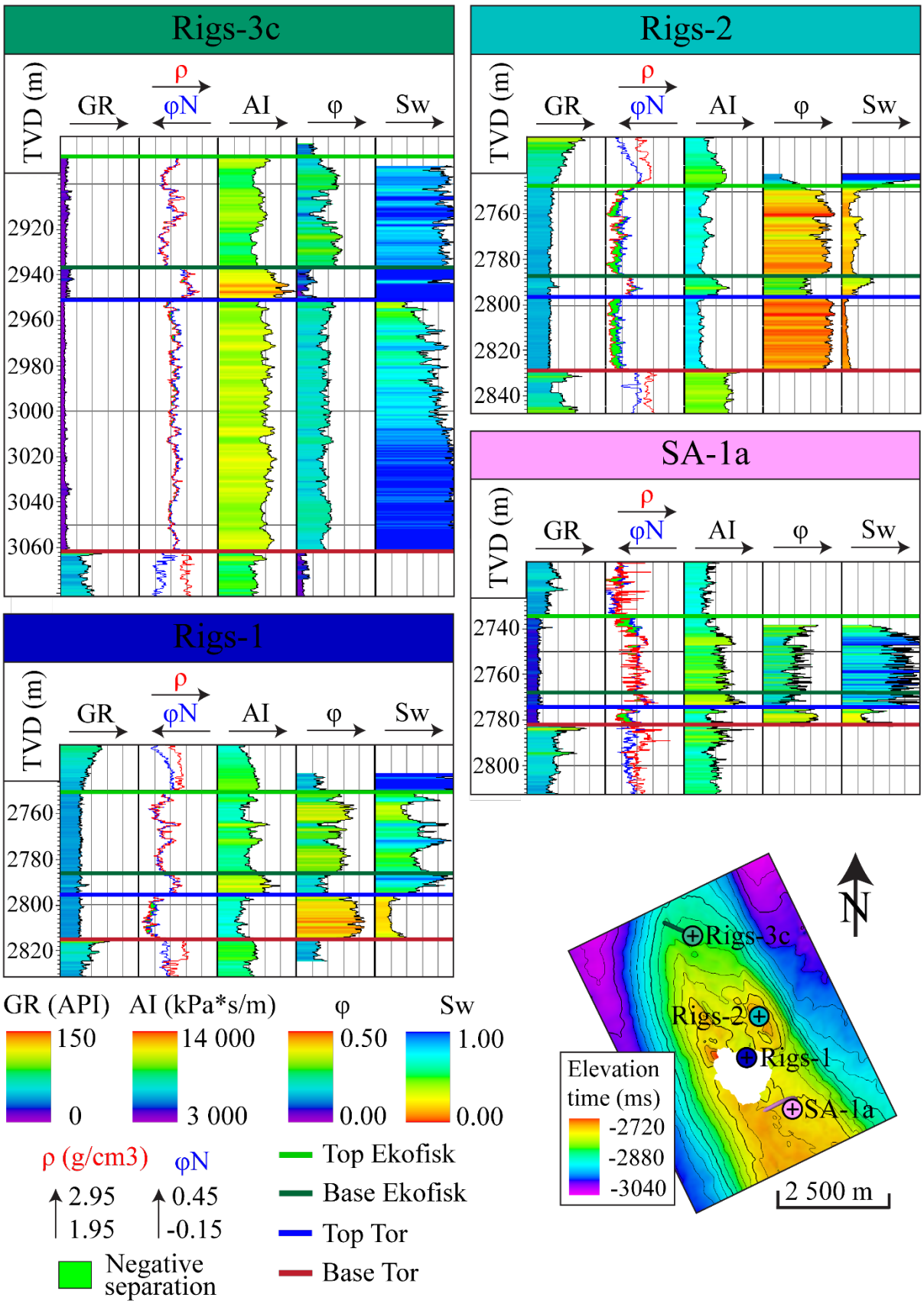


***Figure 6.16**: Well log interpretations based on four key wells covering the reservoir (i.e., Rigs-1, Rigs-2, Rigs-3C, and SA-1a).*

In the NNW part of the anticline (i.e., well Rigs-3c), the reservoir quality is not favourable for oil production, with lower porosities (about 20 %) and relatively higher water saturation. In the SSE part (i.e., well SA-1a), the reservoir quality is slightly better with porosities of about 30 % in the Tor Fm and lower water saturation. The problem in this area is however the very thin reservoir unit of the Tor Fm. These areas have both very low GR readings indicating pure chalk with low shale content.

The observation from the seismic interpretations of a decrease in thickness towards the SSE is supported by the well interpretations. The main thickness differences are observed for the Tor Fm, which changes from about 110 metres in the NNW to about 5 metres in the SSE; whereas the Ekofisk Fm changes from about 50 metres in the NNW to about 30 metres in the SSW.

## 6.3 Rock physics

Rock properties are plotted against porosity in Figure 6.17. A strong trend between elastic properties (i.e., bulk and Young's modulus) and porosity is observed, where low values of the elastic properties are related to high porosities. This negative correlation is most prominent for the Tor Fm but it is observed to some extent for the Ekofisk Fm. It indicates that the reservoir rocks with low porosity are stiffer than the high-porosity rocks, and that the rocks with high porosity are more susceptible to deformation (i.e., compaction and/or faulting).

A trend is also observed between water saturation and porosity, where high porosities yield low water saturation. This is in agreement with the observation from the well-log interpretations, where the lowest water saturations are observed for the rocks with highest porosity, resulting in reservoir rocks of excellent quality.

No trend is observed between Vp/Vs ratio and porosity, indicating that AVO effects are not sensitive to porosity. However, acoustic impedance yields a strong negative correlation with porosity. This trend is somewhat clearer for the Tor Fm than the Ekofisk Fm. The relationship indicates that seismic reflections are dependent on the porosity of the reservoir rocks.

The cross-plot of gamma ray and porosity shows different clusters of data. These clusters correspond to data from different wells and show that the formations have very well-defined ranges of GR values at the different well locations. Nevertheless, as expected from the well interpretations, there is a positive correlation between the two properties. Assuming that the gamma ray values represent shale content, the highest reservoir quality (i.e., high porosity and low water saturation) is found in the chalks with the highest shale content. The different clusters of data for each well indicates that the shale content is relatively constant vertically, but it varies laterally.

Other rock properties are cross-plotted in Figure 6.18. Based on the cross-plots, the Tor Fm has a larger range of acoustic impedance values than the Ekofisk Fm, indicating that larger variability in the seismic response is expected for the Tor Fm. Acoustic impedance is highly dependent on the elastic properties (i.e., bulk and Young's modulus), where low acoustic impedances are related to low values of the elastic parameters. This trend is strongest for the Tor Fm.

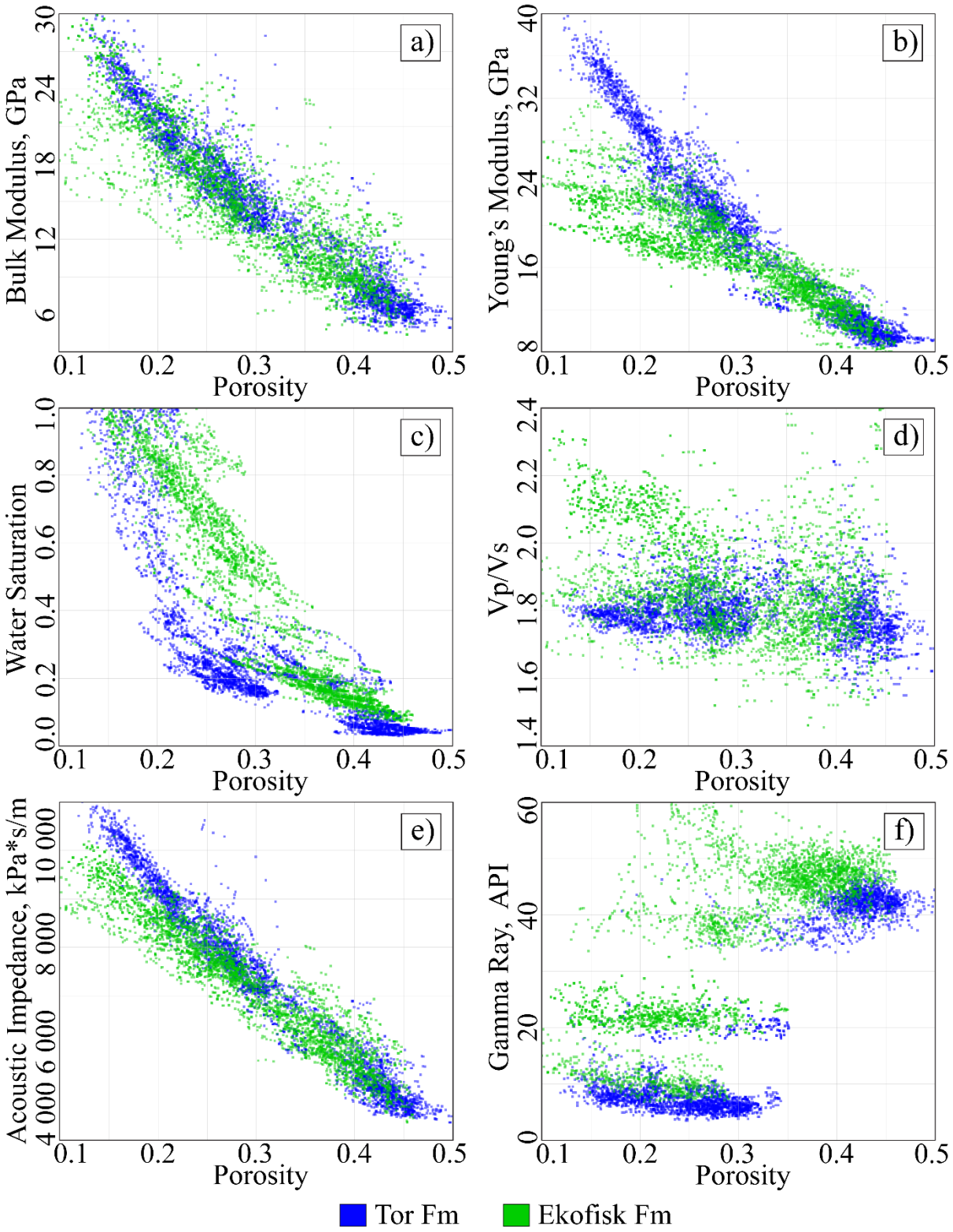


***Figure 6.17**: Different rock properties are plotted against porosity for the two reservoir units. The properties that are displayed are bulk modulus (a), Young's modulus (b), water saturation (c), Vp/Vs ratio (d), acoustic impedance (e), and gamma ray (f).*

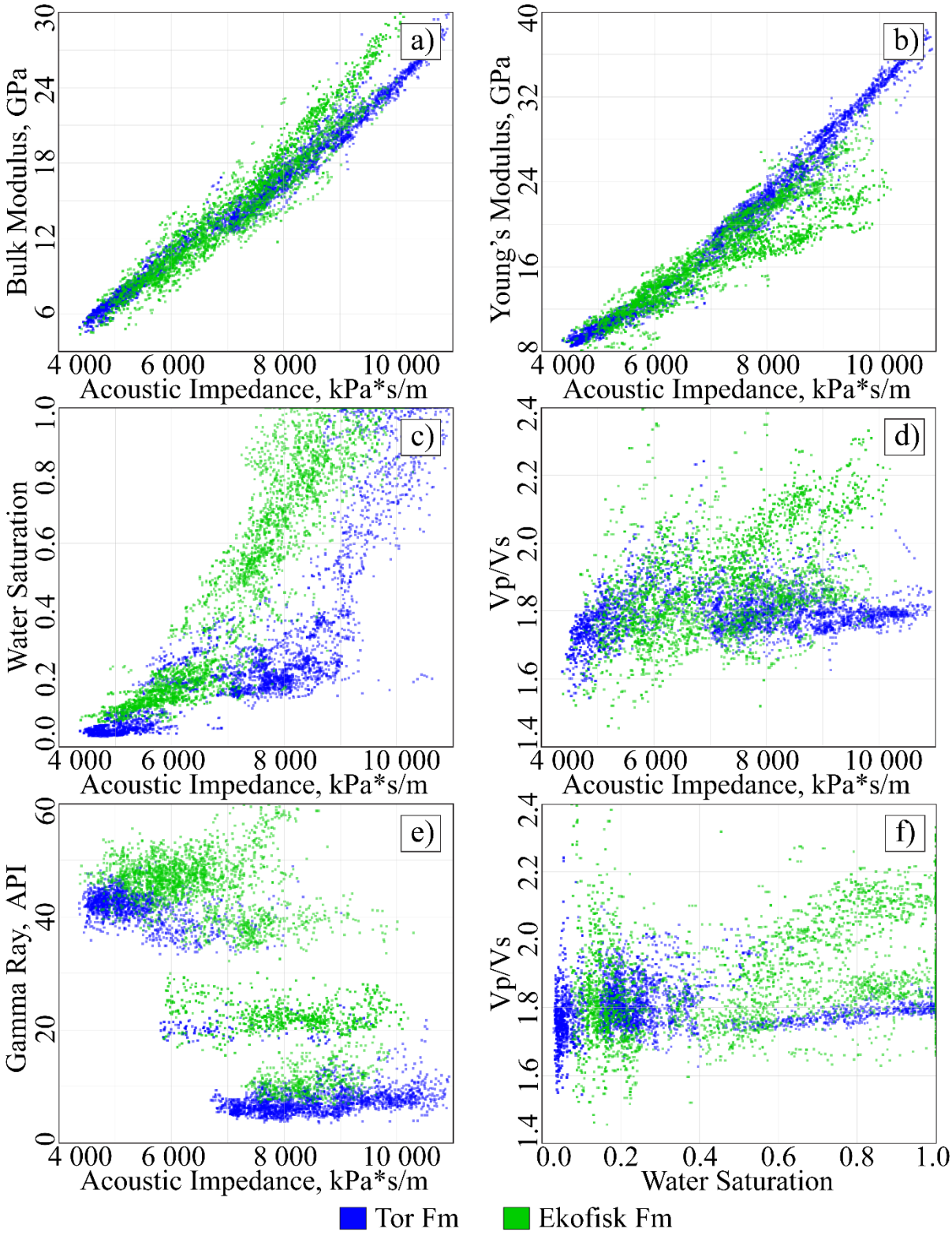


***Figure 6.18**: Cross-plots of different rock properties. The properties that are plotted against acoustic impedance are bulk modulus (a), Young's modulus (b), water saturation (c), Vp/Vs ratio (d), and gamma ray (e). Vp/Vs ratio is also plotted against water saturation (f).*

The relationship between the elastic properties and acoustic impedance might also be linked to the effect of porosity on the elastic parameters and the strong correlation between porosity and

acoustic impedance. However, the elastic properties are also affected by changes in the mineralogy mix, which may affect the acoustic impedance.

A trend is observed between acoustic impedance and water saturation, where low water saturations yield low acoustic impedance. This indicates that it should be possible to detect oil- compared to water-bearing formations in the seismic data. In addition, it indicates that changes in water saturation with production time should be detectable. This trend, however, might also be connected to changes in porosity.

A very weak positive correlation between acoustic impedance and Vp/Vs ratio is observed, and the same happens for the cross-plot of Vp/Vs ratio and water saturation. This indicates that AVO effects might be related to fluid saturation. However, given the very weak nature of this relationship, it is probably not possible to detect AVO effects in seismic data.

The clusters of gamma ray data discussed above are observed also when plotting the data against acoustic impedance. This cross-plot shows a negative correlation. However, this trend might also be linked to other rock properties (e.g., porosity and acoustic impedance).

## 6.4 Structural changes

As previously discussed, the structural changes that are expected to be observed in the time-lapse data include compaction and fault reactivation. The analysis of these processes is given below.

### 6.4.1 Time-shift

A comparison of the same seismic section from the three full stack seismic surveys is shown in Figure 6.19. The top reservoir reflector interpreted on the 1995 survey is also displayed for reference. On the eastern part of the section, the top reservoir reflector (1995) is at the peak amplitude on the 1995 survey but lies just above the peak amplitude on the more recent surveys. This downward shift of the reflector represents the time-shifts caused by compaction.

The negative time-shift between the different surveys is displayed on a seismic section in Figure 6.20. A larger time-shift is observed between 1995 and 2011 than between 1995 and 2005. The time-shift starts in the overburden and increases (i.e., becomes more negative) with depth towards the reservoir, reaching a maximum of about -6 ms TWT at the reservoir level between 1995 and 2011. Just below the reservoir, the time-shift slightly decreases, before it continues to increase with depth. This is better observed by studying the first derivative of the time-shift. This derivative shows a generally weak negative response within the reservoir and a strong positive response just below the reservoir (Figure 6.20). This indicates that the time-shift increases within the reservoir and decreases below.

This behaviour of the time-shift is partly caused by compaction and partly by velocity changes as discussed in chapter 3.5.1. An increase of the time-shift with depth in the overburden, most likely means that the lithology is stretched and the seismic velocity decreases. The sharp reduction in time-shift just below the reservoir is caused by an increase in velocity due to the compaction of the reservoir. The velocity of the reservoir is also affected by the decrease in pore pressure, and increase in water saturation, caused by the production. This means that the

increase in velocity observed from the time-shift data probably captures a combination of these velocity-increasing effects.

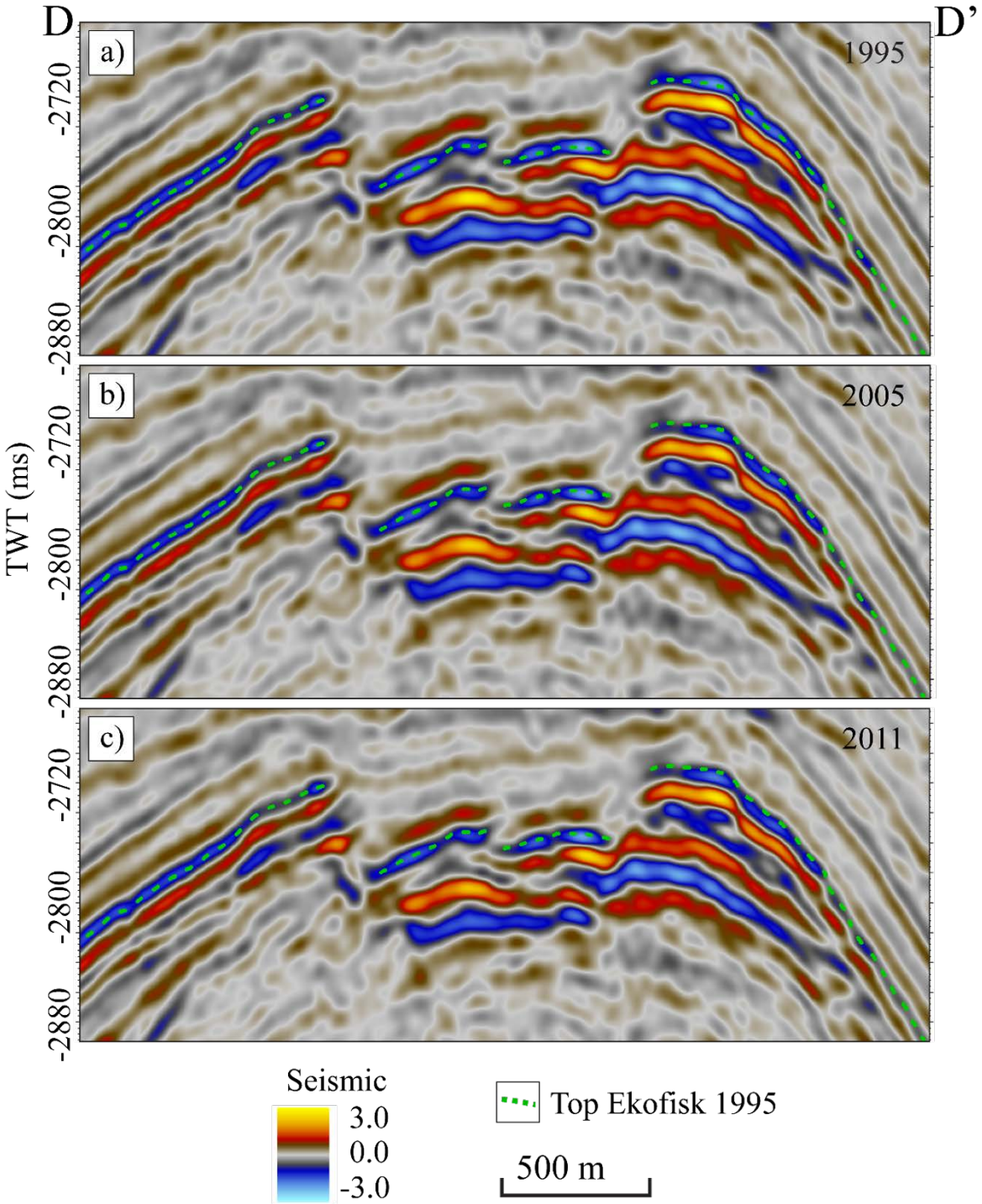


***Figure 6.19**: Seismic section D-D' of the 1995 (a), 2005 (b), and 2011 (c) full stack seismic surveys. The interpretation of the top reservoir reflector interpreted on the 1995 survey is included for reference. The location of seismic section D-D' is shown in Figure 6.22.*

The increase in negative time-shift further below the reservoir indicates that the seismic velocities are more sensitive to the extending rocks in the overburden than to the compaction

in the reservoir. This means that the cumulative time-shift remains negative below the reservoir, even though the velocity is increased by the compaction.

The negative time-shift between 1995 and 2011 is displayed together with seismic data in Figure 6.21. The time-shift starts at about -1500 ms TWT, meaning that the compaction is not affecting the seafloor. Below the reservoir, the time-shift is irregular and not constant, and at least partly correlates with the signal-to-noise ratio (i.e., the time-shift varies sharply where the strength of the seismic signal varies). This behaviour is also observed on the first derivative of the time-shift in Figure 6.20, in areas where strong amplitudes abruptly change with depth. This is expected, as the seismic trace alignment that produces the time-shift results is reliant on relatively high signal-to-noise ratios. The process tries to align the same reflectors of different cubes, and it seems challenging to match the seismic events properly where the seismic signal strength is very low. The signal-to-noise ratio might however not explain all the observed irregular time-shift results.

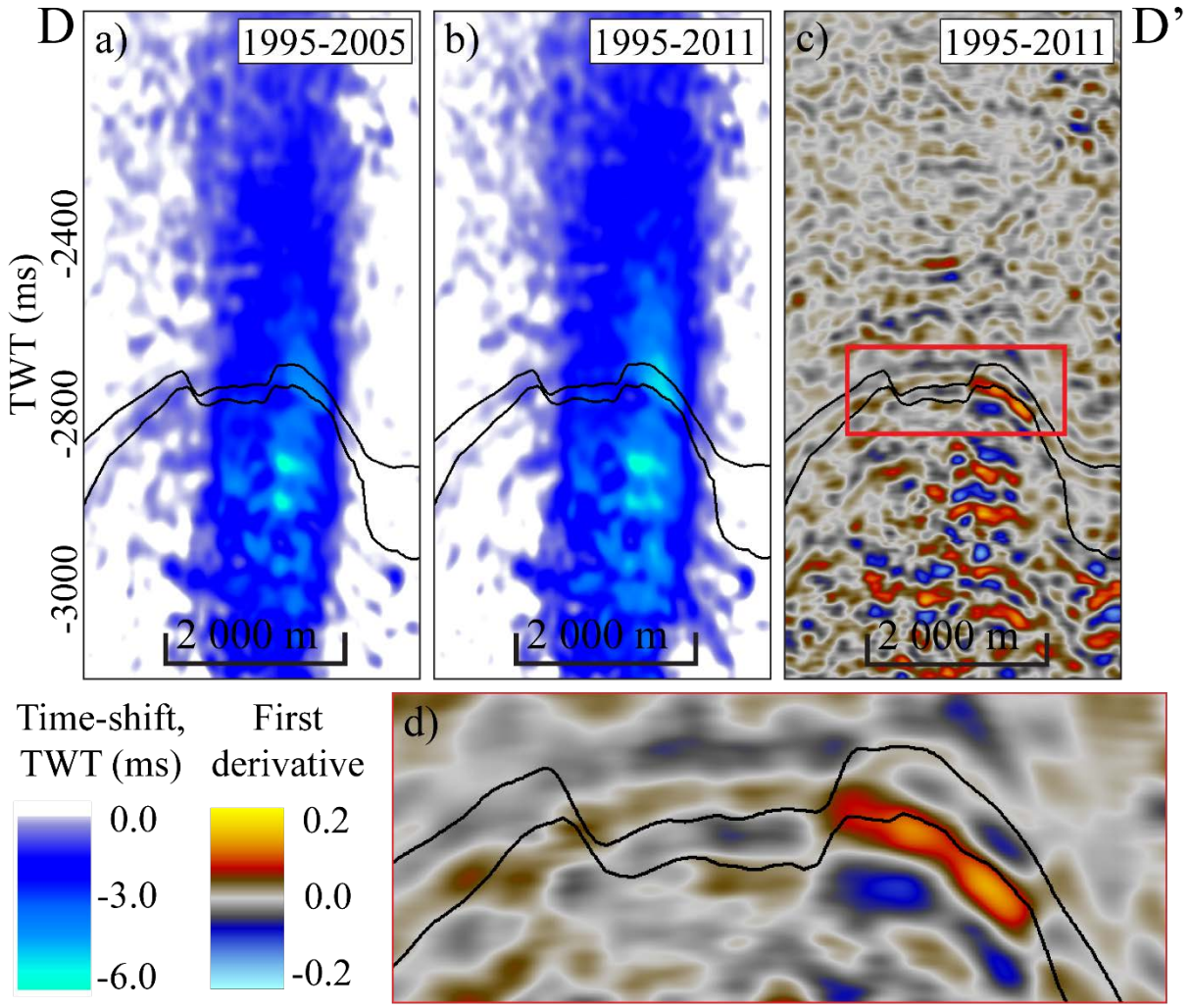


***Figure 6.20**: Negative time-shifts between 1995 and 2005 (a) and between 1995 and 2011 (b) displayed on seismic section D-D'. The first derivative of the 1995-2011 time-shift is displayed in c), with a zoom of the compacting area in d). The top and base reservoir interpretations are included for reference.*

The negative time-shift of the top reservoir reflector is displayed in Figure 6.22. The observed time-shift covers an area just north of the gas cloud. As observed on the seismic sections in

Figure 6.20, the time-shift is larger between 1995 and 2011 than between 1995 and 2005. This applies to both the absolute value and the lateral extent of the time-shift, and it indicates that compaction continues with production. A small negative time-shift is also shown to the WSW on the SSE part of the anticline. Note that the time-shift is not continuous across faults, which is observed by comparing the time-shift with variance (Figure 6.22c). This is an indication of fault reactivation, and it is observed that some of the main normal faults are reactivated as reverse faults.

The time-shift seems to correlate well with the main production area, as indicated by the production and injection wells displayed in Figure 6.12. Another interesting observation is that the time-shifts correlate with the area of highest quality reservoir rocks identified in the well log data.

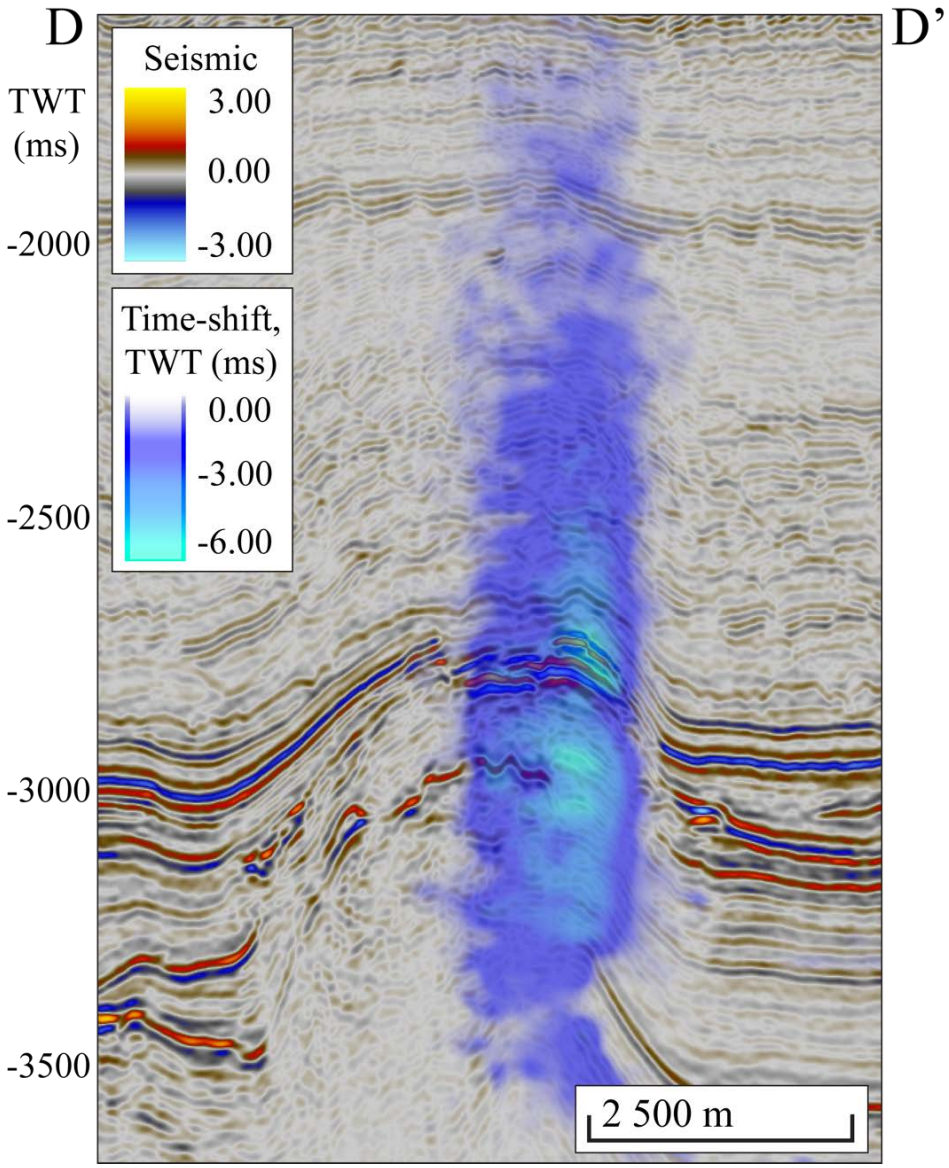


***Figure 6.21**: Seismic section D-D' of the 1995 full stack seismic, coloured with the negative time-shift between 1995 and 2011.*

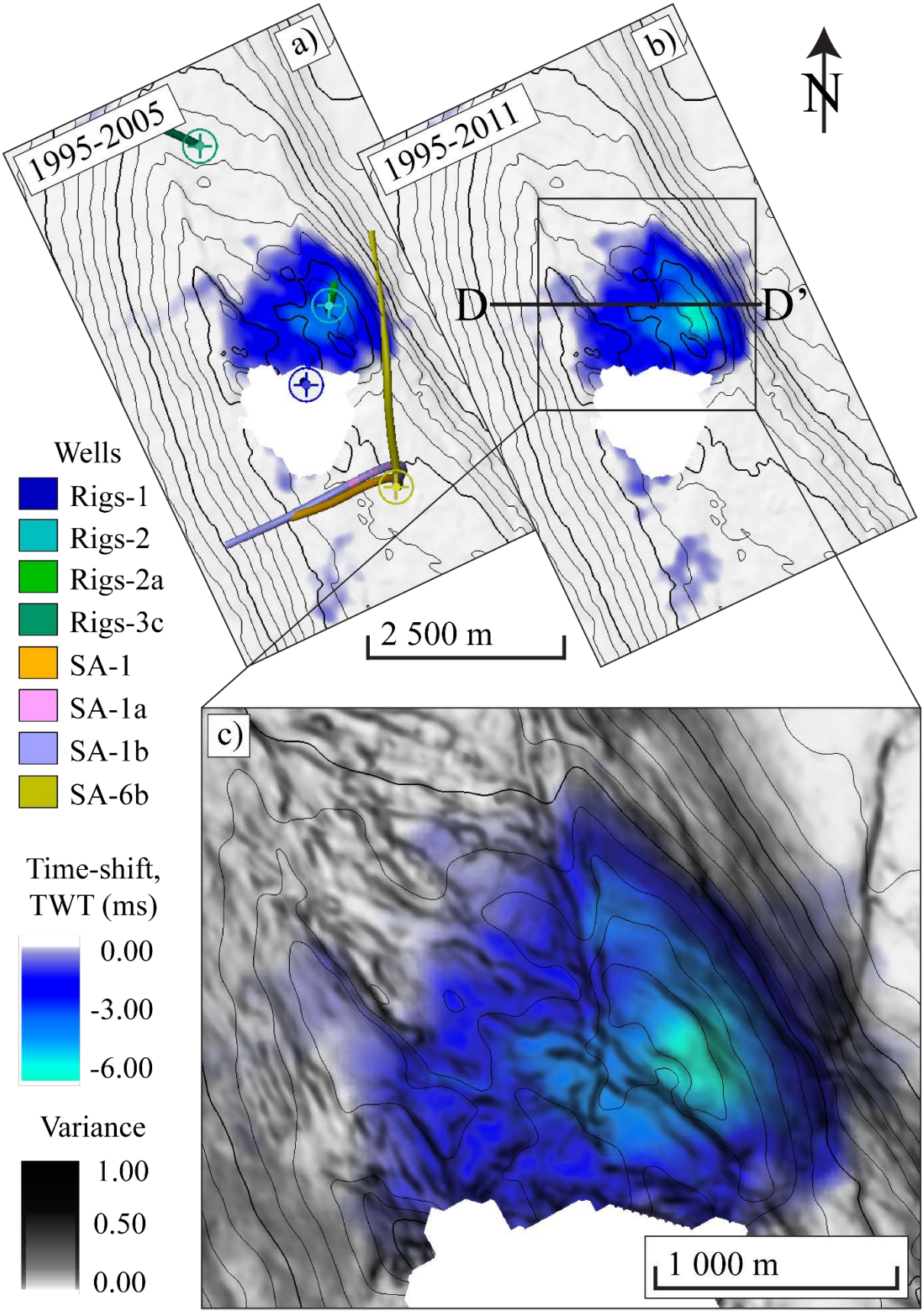


***Figure 6.22**: Time-shift surfaces of the top reservoir reflector. The time-shift between 1995 and 2005 is displayed in a) and between 1995 and 2011 in b). The 1995-2011 time shift surface is displayed together with variance in c). Some wells used for the time-shift analysis are shown in a).*

Based on the lateral extension of the seismic time-shift, the reason for the compaction can be investigated with the help of well log data. Figure 6.23 shows a cross-plot of the elastic properties, bulk and Young's modulus. The data have been filtered to the Tor Fm, because it is assumed that this is the compacting formation as it is the main reservoir unit and contains the rocks with lowest stiffness and highest porosity. The compacting reservoir is identified based on the well locations displayed in Figure 6.22. These wells show lower values of the elastic properties than those located in other parts of the reservoir. The compacting reservoir (i.e., the Tor Fm in the wells Rigs-2 and Rigs-2a) has an average porosity of about 43 %, whereas the other well data of the cross-plot in Figure 6.23 (excluding Rigs-1) yield an average porosity of about 24 %.

Because the time-shift below the gas cloud (i.e., location of well Rigs-1) cannot be trusted due to the poor signal-to-noise ratio, it is unclear if this part of the reservoir is compacting. However, as the time-shift is slowly decreasing towards the gas cloud area in Figure 6.22, it is likely that it continues into this area and terminates 'somewhere' within this area. This interpretation is strongly supported by the cross-plot in Figure 6.23, which shows similar behaviour for the Rigs-1 data as the compacting area.

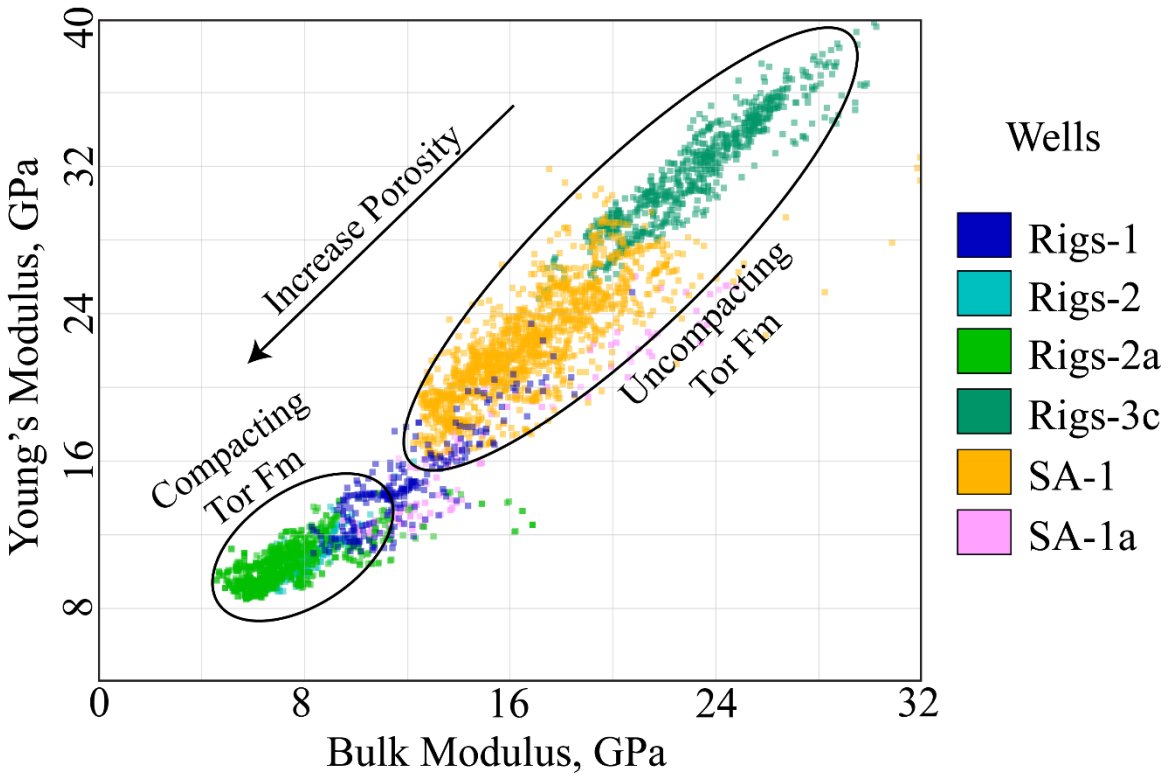


***Figure 6.23**: Cross-plot of bulk and Young's modulus of the Tor Fm, where the compacting and uncompacting formations are highlighted based on well location compared to seismic time-shifts.*

Figure 6.24 shows different rock properties plotted against the seismic time-shift (i.e., compaction) extracted along the wellbores. Although the data plotted against each other (i.e., well data and seismic data) are of very different resolution some clear trends are observed. The resolution problems are evident as the large value ranges of the well data show a relatively small variation of the time-shift.

As expected, low values of the elastic properties (i.e., bulk and Young's modulus) correlate with negative seismic time-shift. The same applies for water saturation and porosity, where time-shift is observed for rocks with high porosity and low water saturation.

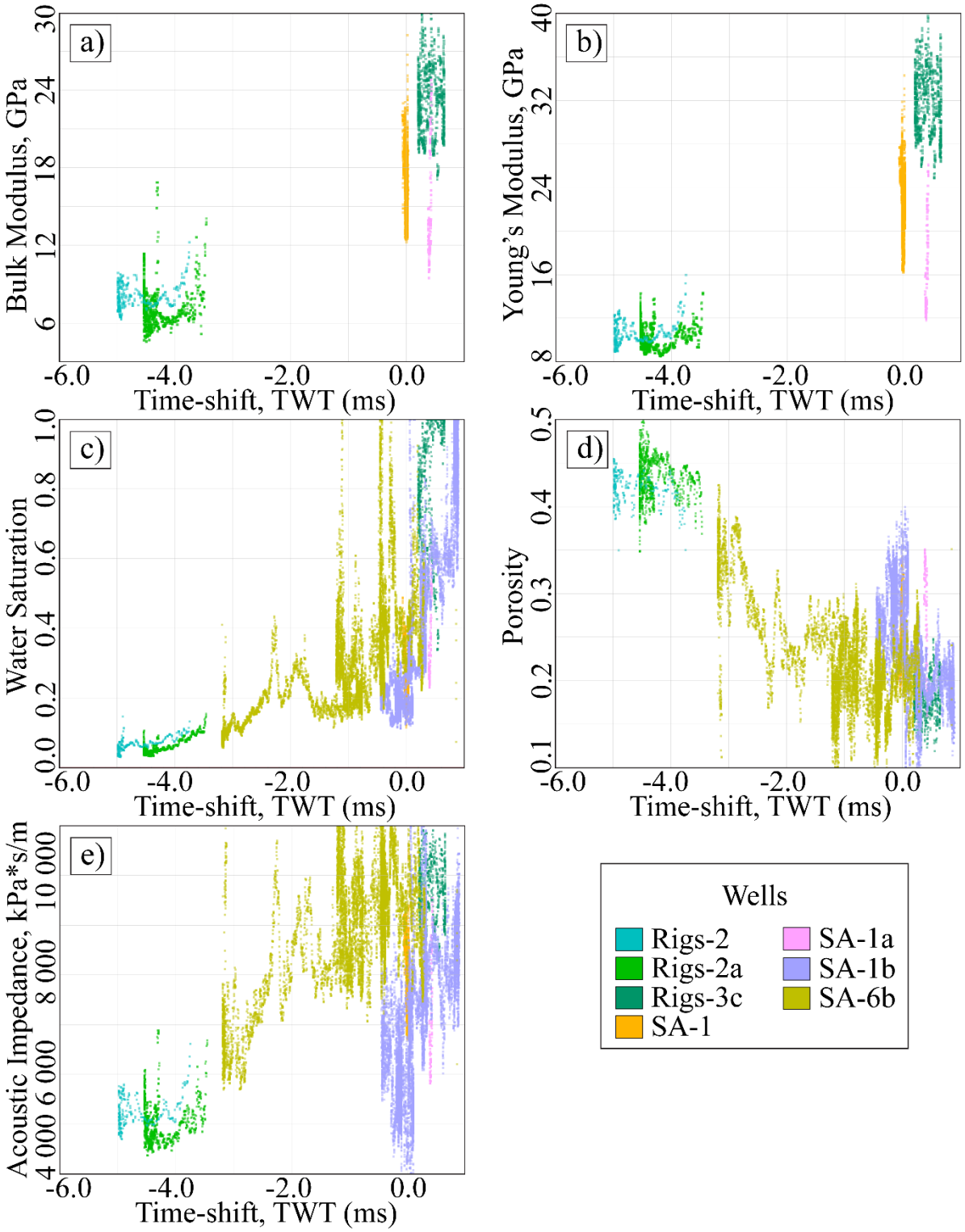


***Figure 6.24**: Different rock properties plotted against 1995-2011 seismic time-shift extracted along the wellbores, filtered to the Tor Fm. The properties displayed are bulk modulus (a), Young's modulus (b), water saturation (c), porosity (d), and acoustic impedance (e).*

There is a correlation between time-shift and acoustic impedance, where negative time-shift is observed for low acoustic impedance values. This indicates that the compacting area should be detected as anomalously soft events in pre-production seismic data.

Figure 6.25 shows a seismic time-shift section along the wellbore of well SA-6b, together with the porosity log. The largest amount of compaction is observed for the high-porosity reservoir rocks, and the time-shift is decreasing away from this area together with a decrease in porosity. The effect of different resolution on the seismic and well data is also observed as the detailed porosity log is compared with the relatively smooth time-shifts.

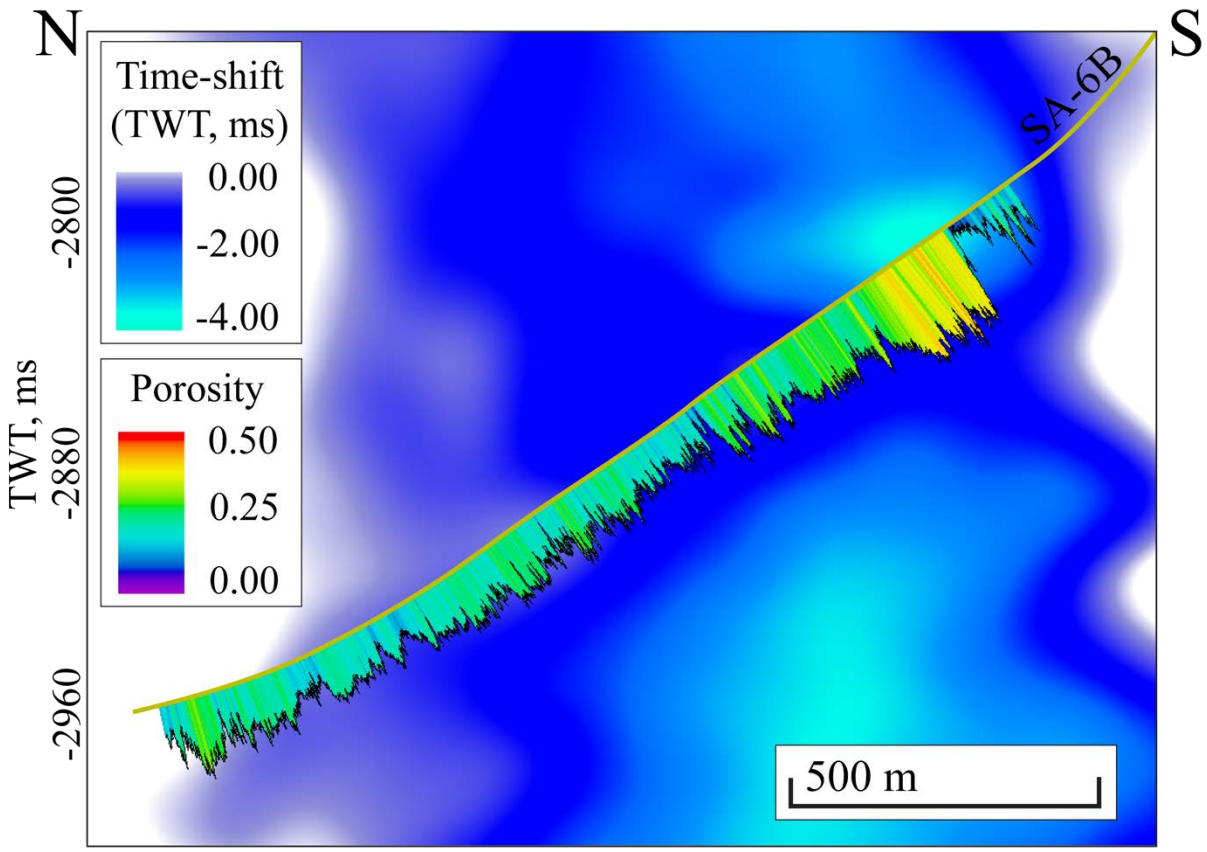


***Figure 6.25**: Porosity log of well SA-6b on the 1995-2011 time-shift. The locations of the well and the seismic section are displayed in Figure 6.22a.*

## 6.4.2 Fault reactivation

RMS of the differences in variance response between the different surveys are displayed as attribute maps in Figure 6.26. The results represent differences in the continuity of the seismic reflectors and are thus assumed to indicate faulting and fault reactivation. Differences are observed between the surveys, with larger values encountered between 1995 and 2011 than between 1995 and 2005. This is interpreted to be a result of continued faulting as the reservoir is produced and the reservoir pressure drops.

The main differences are observed for the main production area just north of the gas cloud (i.e., the area affected by compaction), and decreases towards the NNW. The fact that fault reactivation is interpreted in the NNW part, where no production wells have been drilled,

indicates the whole reservoir has been affected by the production, not just the main production area. Minor changes are observed on the SSE part of the reservoir. These differences, however, are not interpreted as faulting because no proper trend is observed, but rather as noise.

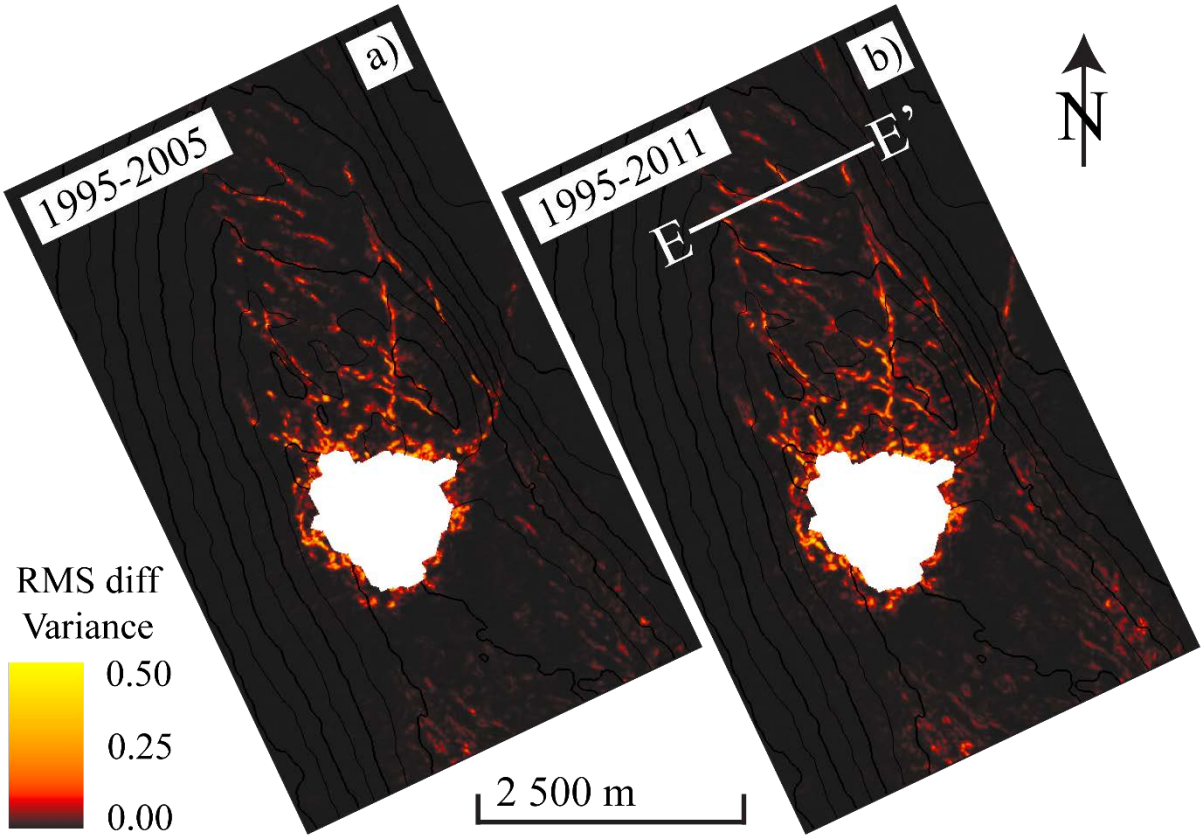


***Figure 6.26**: Attribute maps generated from the RMS of the difference in variance at reservoir level between 1995 and 2005 (a) and between 1995 and 2011 (b).*

The fault reactivation results are compared with the ant tracking results in Figure 6.27. The two main faults outlining the small graben deduced from the ant tracking are reactivated based on the difference in variance. In addition, seismic sections of the 1995 and 2011 surveys are compared, and subtle amplitude differences are observed where the top reservoir reflector is offset by the faults.

The 1995-2011 fault reactivation surface is displayed together with the 1995-2011 time-shift surface in Figure 6.28. The previously discussed time-shift results showing inconsistent compaction across several faults supports the assumption that the variance differences allow identifying fault reactivation.

Interestingly, the same observation can be made to the NNW outside the compacting area, where small positive time-shift changes across faults. It should be noted that the positive time-shift is observed everywhere outside the compaction area and the reservoir, and is thus generally assumed to represent 'background noise'. The time-shift data represent a combination of this noise and actual compaction. Thus, the observation that the positive time-shift aligns with the fault reactivation from variance differences indicates that the time-shift outside the main compaction area is related to minor compaction and fault reactivation.

Obviously this interpretation is approaching the limit of seismic resolution and is highly uncertain.

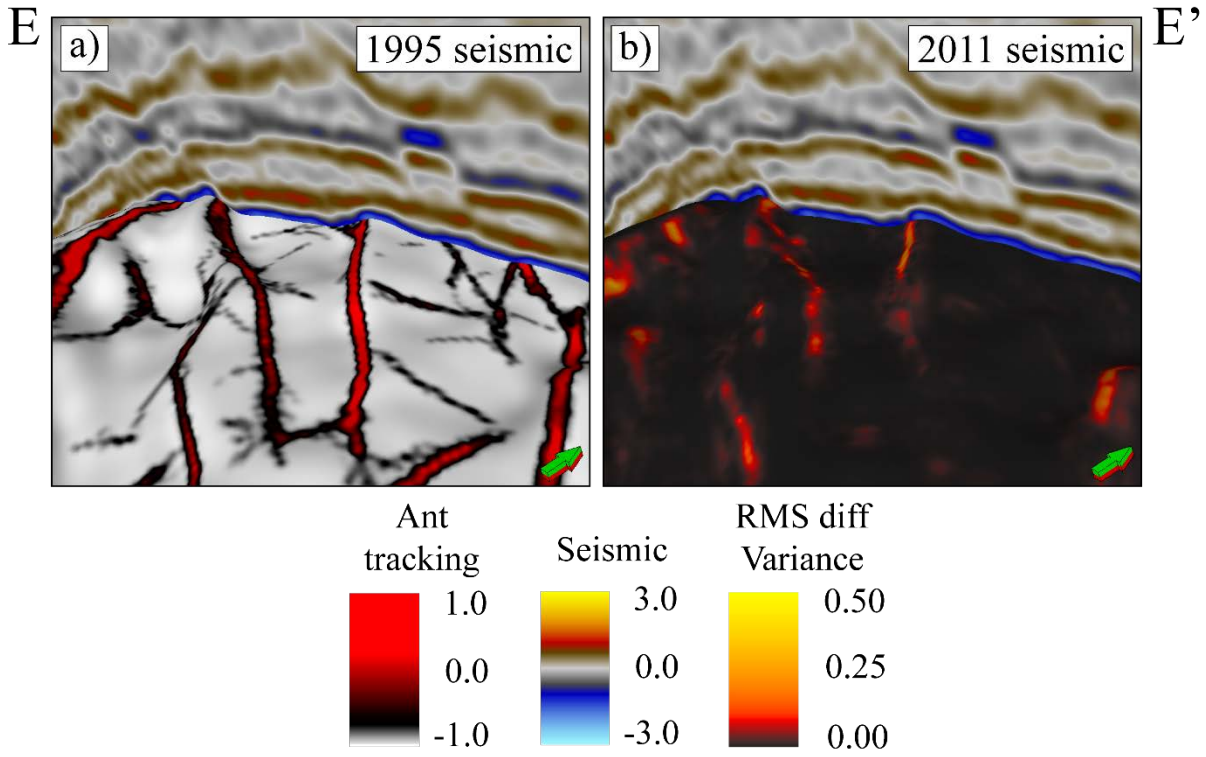


***Figure 6.27**: a) Top reservoir ant tracking map displayed together with seismic section E-E' of the 1995 full stack seismic. b) Attribute map of the RMS of the difference in variance between the 1995 and 2011 at reservoir level, displayed together with seismic section E-E' of the 2011 full stack seismic. The location of seismic section E-E' is shown in Figure 6.26b.*

## 6.5 Amplitude and AVO analysis

As discussed in chapter 5.5, the amplitude and AVO analyses are based on firstly detecting pre-production anomalies, and then identifying how these anomalies change with production time.

### 6.5.1 Pre-production full stack amplitudes

The 1995 full stack amplitudes of the reservoir (i.e., pre-production) are displayed as attribute maps in Figure 6.29. The exact amplitude of the top reservoir reflector is a strong negative feature (i.e., soft event) over the whole area, and does not show significant anomalies. This indicates that the top reservoir reflector is not sensitive to fluid saturation, and hydrocarbon-water contacts cannot be identified. However, by taking the RMS of the amplitudes over the reservoir interval, anomalously high amplitudes are observed on the anticline compared to the surrounding area, possibly highlighting oil saturation.

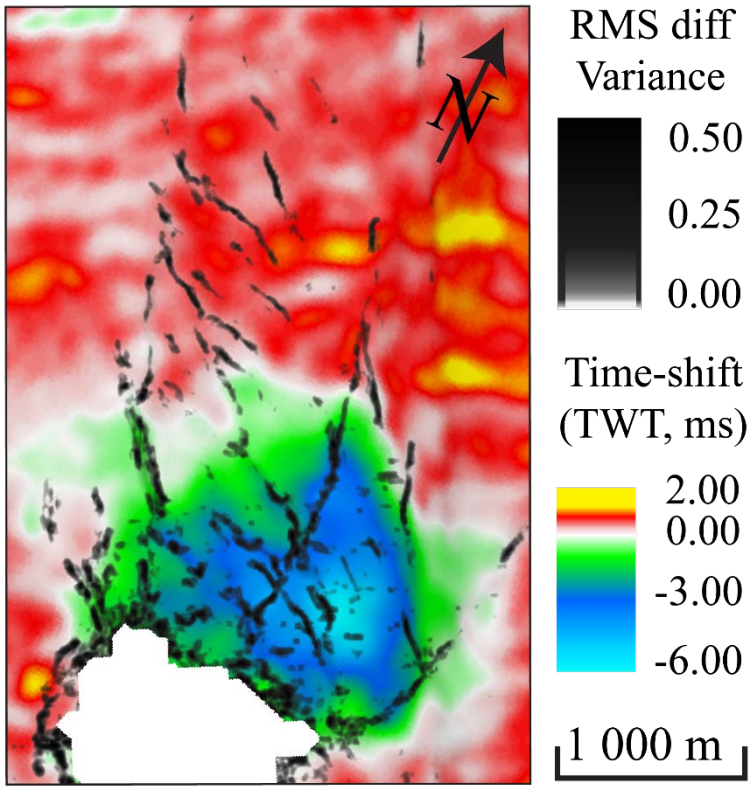


***Figure 6.28**: Attribute map of the RMS of the difference in variance between the 1995 and 2011 at reservoir level displayed on top of the 1995-2011 time-shift map.*

In order to understand why anomalies are observed when studying the RMS amplitude from the reservoir interval and not on the top reservoir reflector, the geological equivalent to the seismic amplitudes need to be discussed. A possible explanation is that the top reservoir reflector represents the Ekofisk Fm, which yields an acoustic impedance that is not very sensitive to oil saturation. However, when extracting the amplitudes from the reservoir interval, the seismic response of the Tor Fm is also included, which may be more sensitive to fluids.

This interpretation is partly supported by the rock physics study, showing a greater range of acoustic impedance values as a function of water saturation for the Tor Fm than for the Ekofisk Fm. This indicates that the Tor Fm is more sensitive to changes in fluid saturation, and might explain why hydrocarbons are detected by including the entire reservoir interval (i.e., the Ekofisk and Tor fms) and not only the Ekofisk Fm.

It should be noted that acoustic impedance correlates better with porosity than water saturation, based on the rock physics study. This means that the mapped high RMS amplitudes are probably more related to areas of high porosity, than oil saturation as assumed above. The correlation between porosity and water saturation complicates these interpretations, making it difficult to separate between the two effects. In reality, the amplitude anomalies are probably related to a combination of high porosity and oil saturation.

A strong response is observed for the main production area, which also correlates with the large porosity and the compaction. This supports the interpretation that high amplitudes are related to both low water saturation and high porosity.

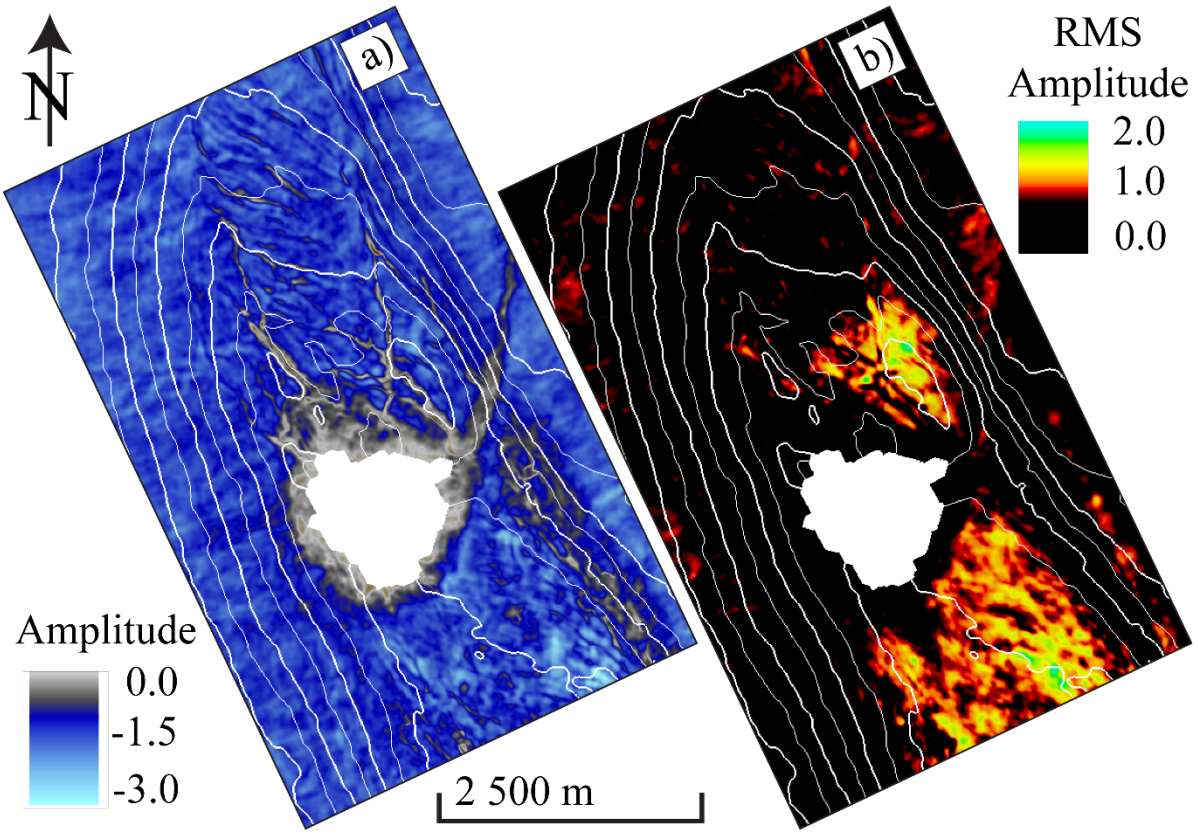


***Figure 6.29**: Top reservoir amplitude maps of the 1995 full stack seismic. a) Exact amplitude of the top reservoir reflector. b) RMS amplitude taken over the reservoir interval.*

Strong amplitude responses are also observed for the SSE part of the anticline; however, no anomalies are observed on the NNW part. This is to some extent in agreement with the well log interpretations (chapter 6.2.2). The NNW part of the anticline is identified as containing the lowest reservoir quality based on well data, and the reservoir quality on the SSE part is fairly good assuming that it is represented by well SA-1a. This might explain the observed high amplitudes on the SSE part of the anticline. However, the oil-containing reservoir here is very thin, possibly below the resolution of the seismic data. Another possible contributor to the high amplitudes is tuning effect (i.e., interference of seismic waves from closely spaced reflections), and it cannot be excluded that the thin reservoir units to the SSE might approach tuning thickness, thus inducing anomalously high amplitudes.

### 6.5.2 Full stack amplitude changes with production time

A comparison of the full stack seismic of the different surveys on a seismic section is displayed in Figure 6.30. An amplitude decrease with production time is detected within the reservoir. The changes are mainly observed for the soft events, indicating that the reservoir is hardening. This is interpreted to be related to a combination of changes in fluid saturation, decreased pressure, and compaction. This interpretation is supported by the rock physics studies, showing negative correlation between acoustic impedance and porosity, which means that compaction (i.e., decrease in porosity) increases the acoustic impedance. The same is valid for water saturation, as an increase in water saturation will also increase the acoustic impedance.

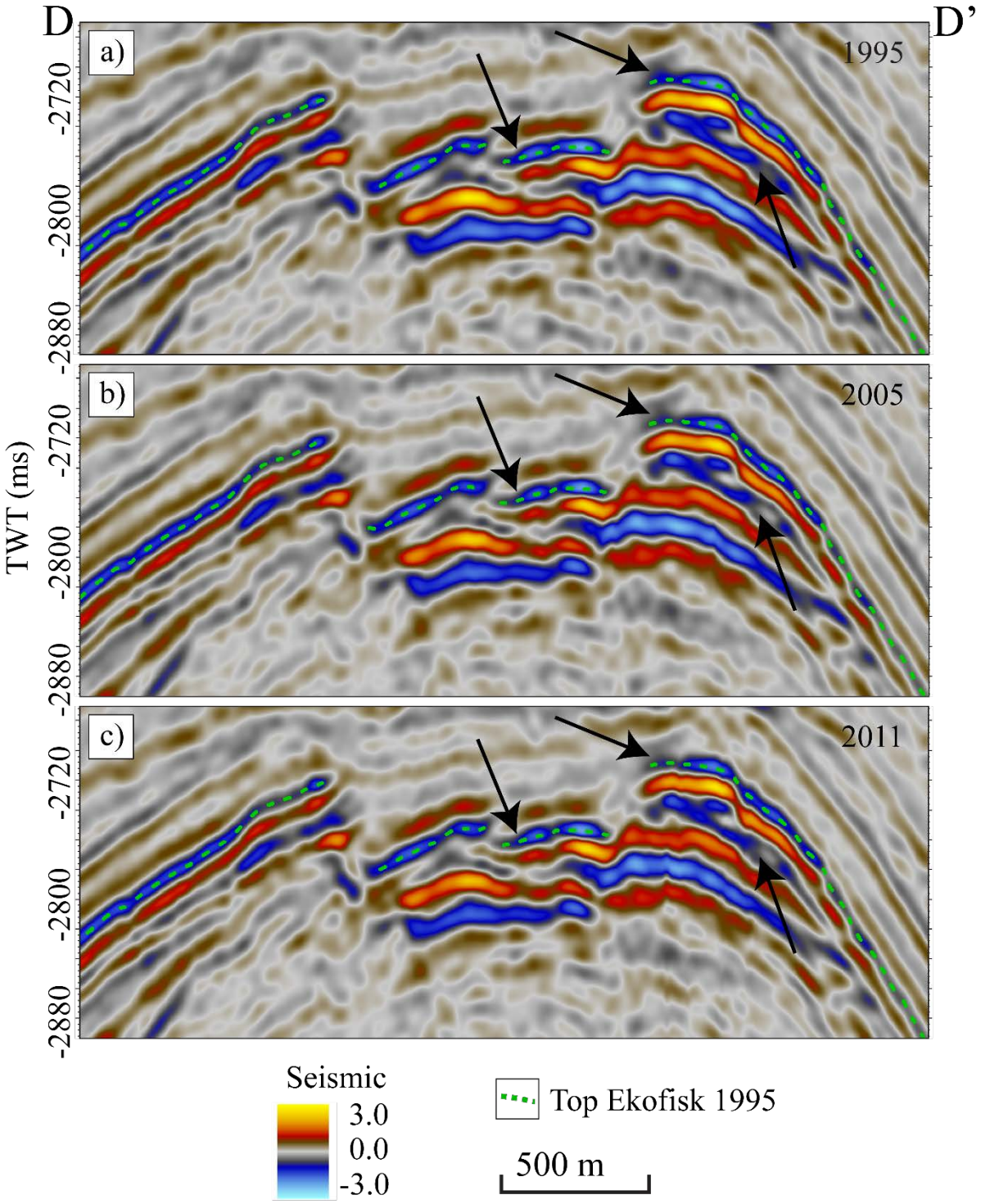


***Figure 6.30**: Seismic section D-D' of the full stack seismic from 1995 (a) and matched full stack seismic of 2005 (b) and 2011 (c). Black arrows indicate decreased amplitudes with time. Note the vertical noise, which is a result of the trace alignment process.*

The RMS of the difference in amplitude with time in the reservoir interval is displayed as attribute maps in Figure 6.31. A significant change in amplitude is observed for the main production area between the different surveys, with the largest difference between 1995 and 2011. The amplitude differences correlate well with compaction (Figure 6.22), indicating that the decreased amplitudes are related to the decrease in porosity caused by compaction.

However, the effect of fluid saturation and pressure should not be excluded. As the pre-production anomaly is assumed to highlight areas of high porosity and oil saturation, it is likely that the decreased amplitudes with production time are caused by a combination of compaction, increase in water saturation, and decrease in pressure.

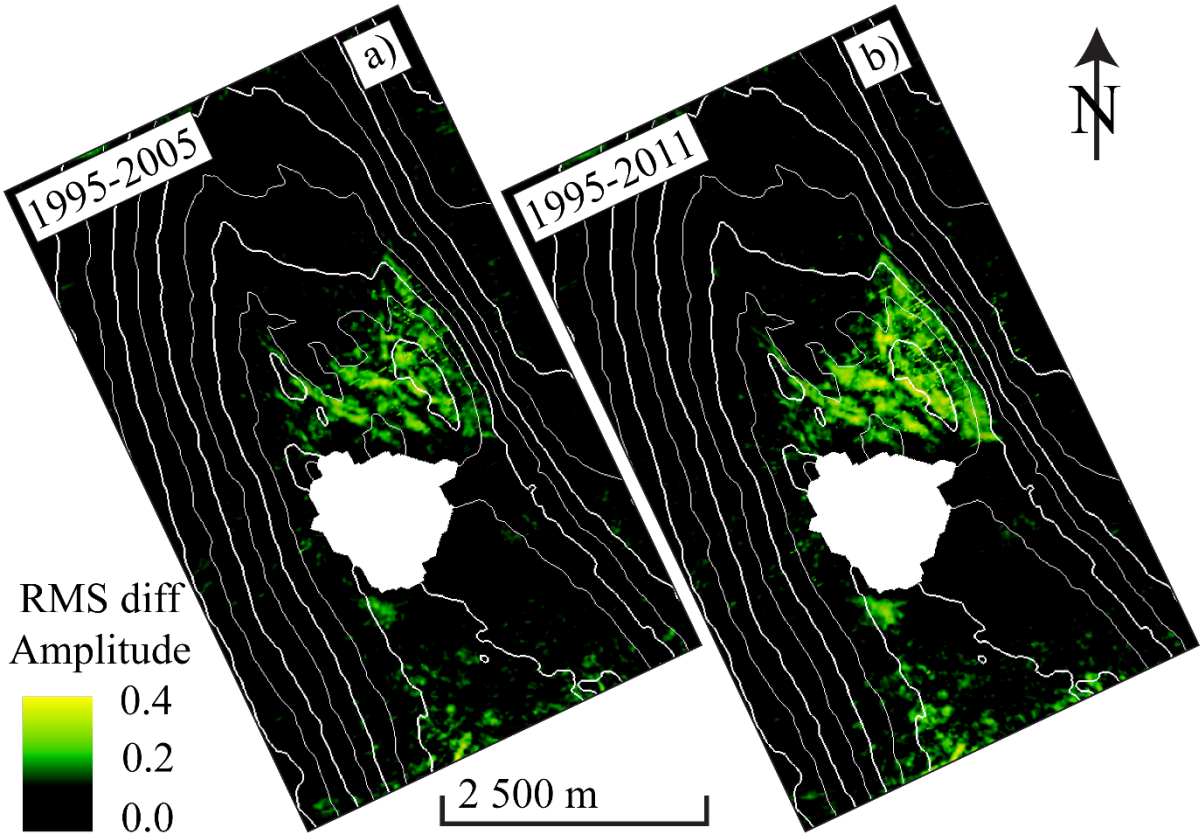


***Figure 6.31**: RMS of the difference in amplitude between 1995 and 2005 (a) and between 1995 and 2011 (b) extracted from the reservoir interval and displayed on the top reservoir surface.*

### 6.5.3 Pre-production AVO effects

The near and far angle stacks of the 1995 survey are displayed in a seismic section in Figure 6.32. As expected, the near stack includes more detailed information than the far stack, allowing a better analysis of both structural elements and amplitudes. It is clearly observed that the amplitudes are decreasing with offset, as no high amplitudes are detected on the far stack. This observation is confirmed by the intercept*gradient, showing strong negative responses, and only minor positive patches in some areas. This indicates that no typical hydrocarbon AVO response (i.e., class 3/2) can be identified in the seismic data. This is expected based on the rock physics study, as the relationship between Vp/Vs ratio and water saturation is identified as too weak to properly affect seismic data. This means that the gradient, which theoretically is strongly dependent on Vp/Vs ratio, is not very sensitive to fluid saturation.

The intercept and gradient of the top reservoir reflector is displayed as amplitude maps in Figure 6.33. As expected from the full stack amplitudes, the intercept shows a strong negative response and no anomaly is detected. The gradient is generally positive over the whole area, and no major anomalies are observed. This reveals that no AVO anomalies are observed for

the top reservoir reflector, which may be explained by the fact that the top reservoir reflector represents the Ekofisk Fm as discussed above. However, the possibility that AVO effects are overall insensitive to fluid saturation cannot be excluded.

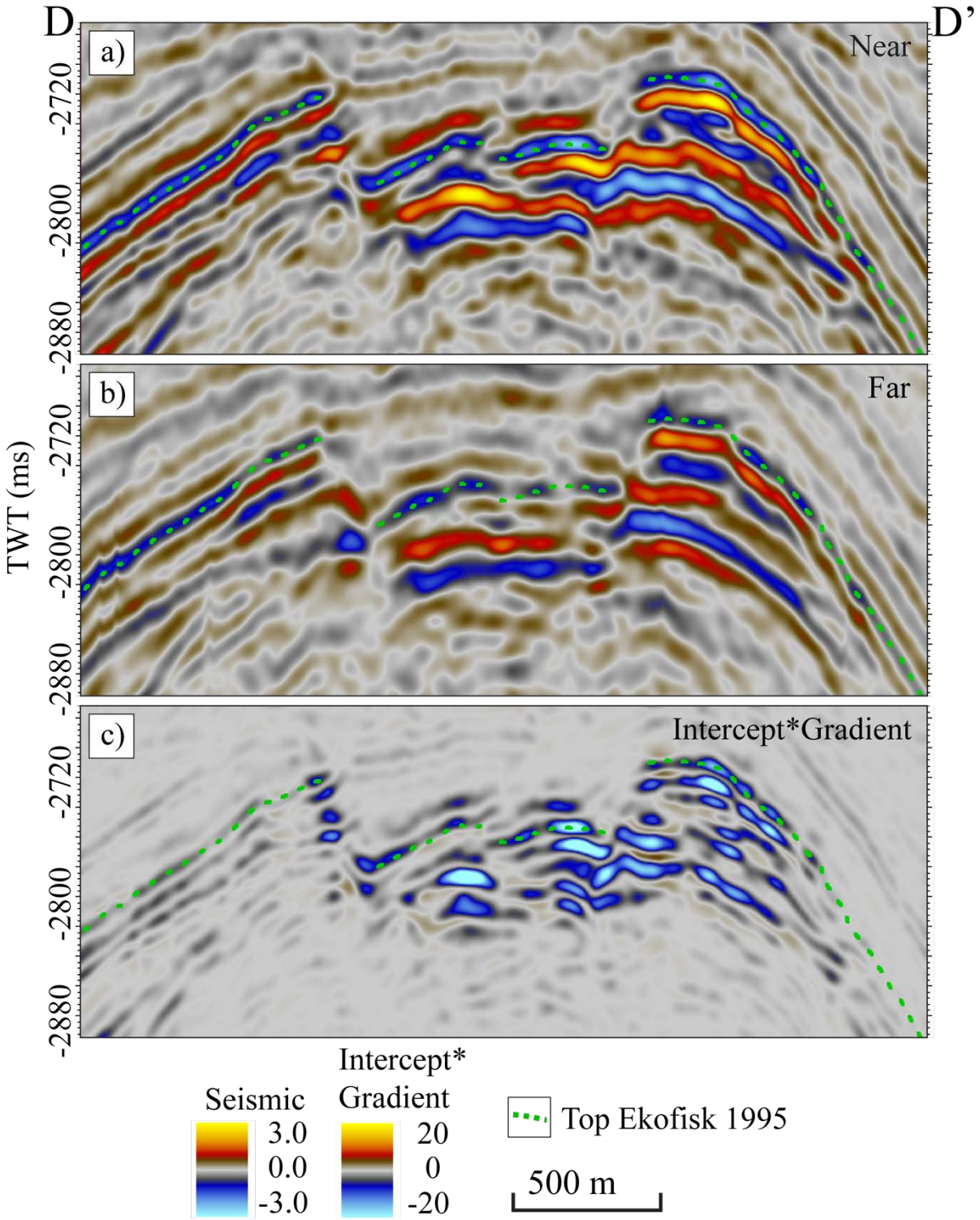


***Figure 6.32**: Seismic section D-D' of the near (a) and far (b) angle stacks, and intercept*gradient (c) of the 1995 survey.*

Although the AVO response observed in the seismic section in Figure 6.32c is not theoretically a common hydrocarbon effect, a clear anomaly is observed on the anticline. This anomaly is located where the reservoir is of high quality, and this is further investigated in map view by taking the RMS of the intercept*gradient from the reservoir interval (Figure 6.34a).

This approach shows a similar result to the RMS of the full stack amplitudes from the reservoir interval, with anomalies observed for the main production area and the SSE part of the anticline (Figure 6.29b). A difference between these results is the observation of higher amplitudes of the RMS of the intercept*gradient to the WSW on the SSE part of the anticline. In contrast, the RMS of the full stack amplitudes shows a larger anomaly to the ENE on the SSE part of the anticline. These differences might be the result of different sensitivity to fluid saturation. The higher amplitudes on the RMS of the intercept*gradient correlate with the location of a production well, which might indicate better reservoir quality in this part compared to the rest of the SSE part of the anticline. This anomaly also follows a contour line which could indicate an oil-water contact.

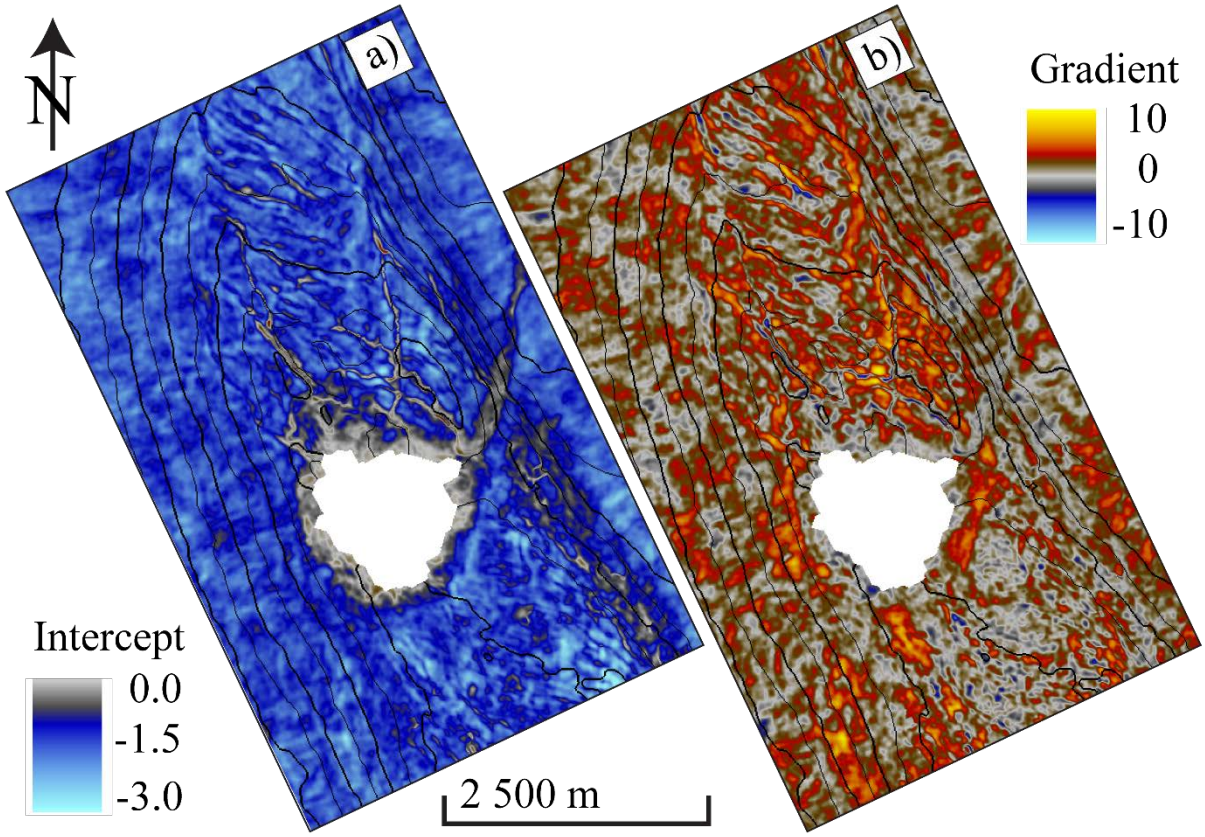


***Figure 6.33**: Top reservoir amplitude maps of the intercept (a) and gradient (b) of the 1995 survey.*

## 6.5.4 Changes in AVO effects with production time

The RMS of the intercept*gradient extracted from the reservoir interval of the 1995 and 2011 surveys are compared in Figure 6.34. The differences are also displayed in Figure 6.35, as maps of the RMS of the difference in intercept*gradient response with time extracted from the reservoir interval. The largest differences are observed as decreased anomalies on the monitor surveys in the main production area, and decreased responses are also observed on the SSE

part of the anticline. These results also show that the anomaly differences partly follow contour lines, possibly indicating movement of the fluid contacts.

Compared to the changes in full stack amplitudes, more differences are observed on the SSE part of the anticline, although these differences do not correlate very well with compaction. This could be an indication that the changes in intercept*gradient capture changes in fluid saturation, whereas the changes in full stack amplitudes are more sensitive to compaction. However, this interpretation is not well supported by the rock physics study, and large uncertainties are associated with these results.

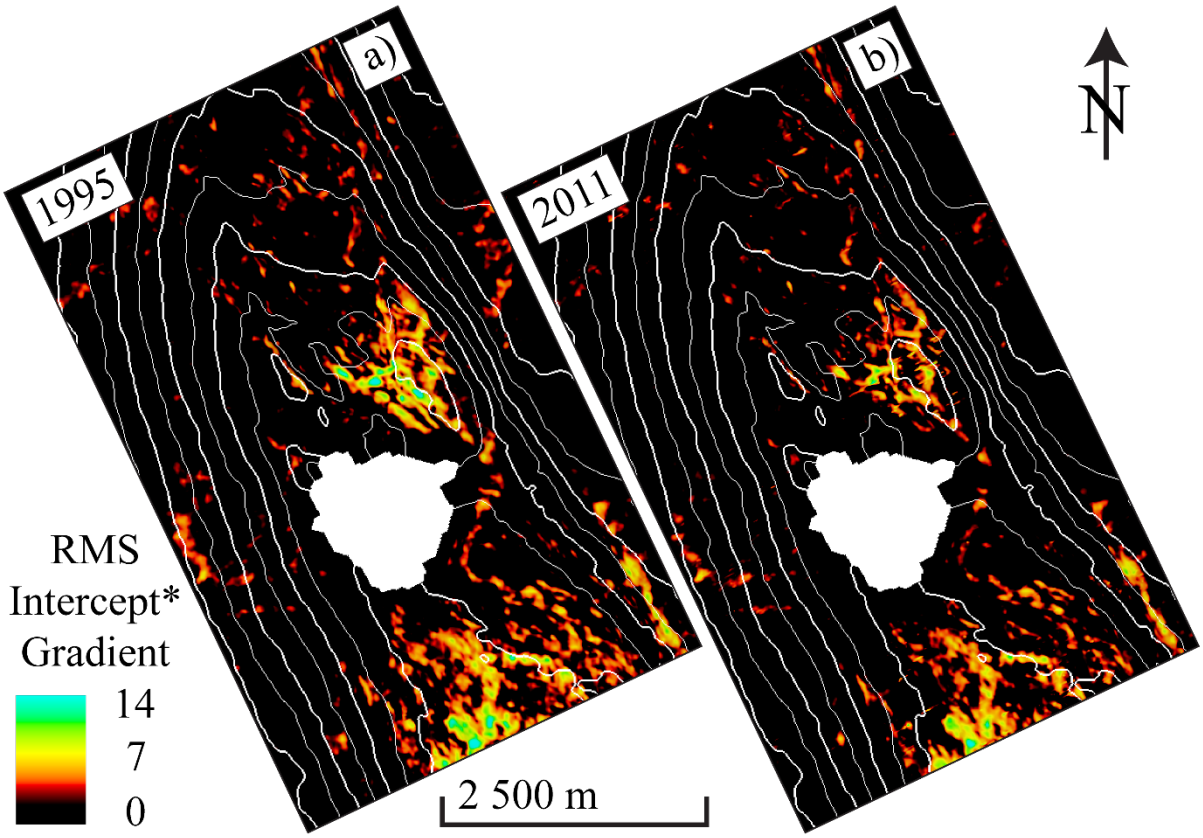


***Figure 6.34**: RMS of the intercept*gradient attribute of the 1995 (a) and 2011 (b) surveys extracted from the reservoir interval and displayed as surface attributes.*

When comparing the RMS of the difference in intercept*gradient from the reservoir interval between 1995 and 2005 with the same results between 1995 and 2011, it is difficult to detect large differences (Figure 6.35). Minor increases in difference are observed in the main production area for the 1995-2011 results. The small differences in these results support the interpretation that changes in intercept*gradient are not sensitive to compaction, as the increase in compaction is not captured. However, assuming that the results are sensitive to fluid saturation, it is expected to better identify the movement of fluid contacts between the time periods (i.e., 1995-2005 and 1995-2011).

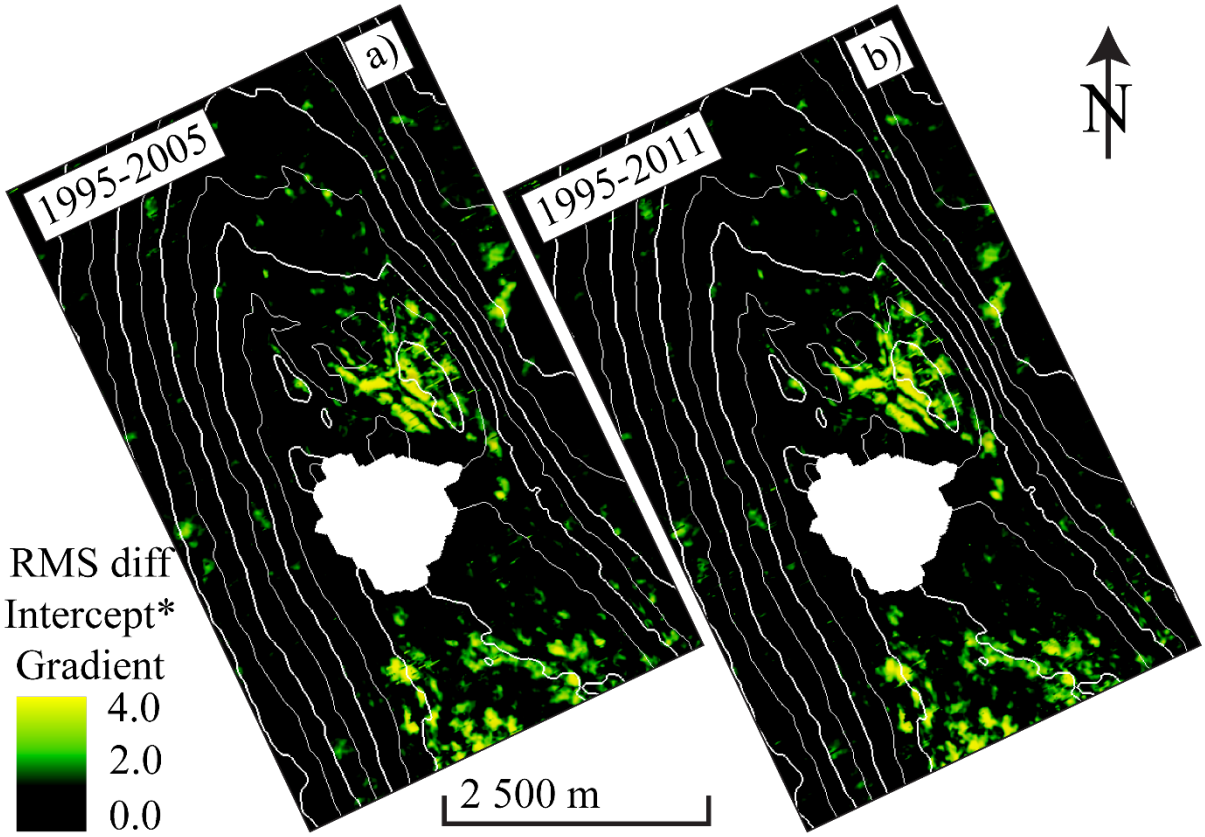


***Figure 6.35**: RMS of the difference in the intercept*gradient attribute of the 1995 and 2005 (a) and between 1995 and 2011 extracted from the reservoir interval.*

## 6.6 Coloured inversion

The result of the 1995 full stack coloured inversion is displayed in a seismic section in Figure 6.36. In addition, the difference in coloured inversion between 1995 and 2005, and between 1995 and 2011 is shown. As expected based on the previous amplitude analyses, the reservoir is identified as a soft event.

A clear hardening effect with time is observed, and the largest difference is between 1995 and 2011. This is in agreement with the amplitude analysis above and is interpreted to reflect compaction and/or increase in water saturation. The hardening is uniformly distributed, and no movement of fluid contacts can be identified. This indicates that the effect is highlighting compaction and decreased pressure, rather than changes in fluid saturation.

When studying the difference in coloured inversion results in map view, the largest hardening effect is observed for the main production area and some changes are also observed for the SSE part of the anticline. This is evident from the horizon probe in Figure 6.37, showing the hardening as a rendered volume of the reservoir interval.

By comparing the changes in coloured inversion with the ant tracking results, it is observed that the hardening effects are inconsistent across faults. This indicates that the faults act as fluid barriers, meaning that the oil accumulations are divided into different zones separated by sealing faults, where the fluids in each fault block move independently of each other.

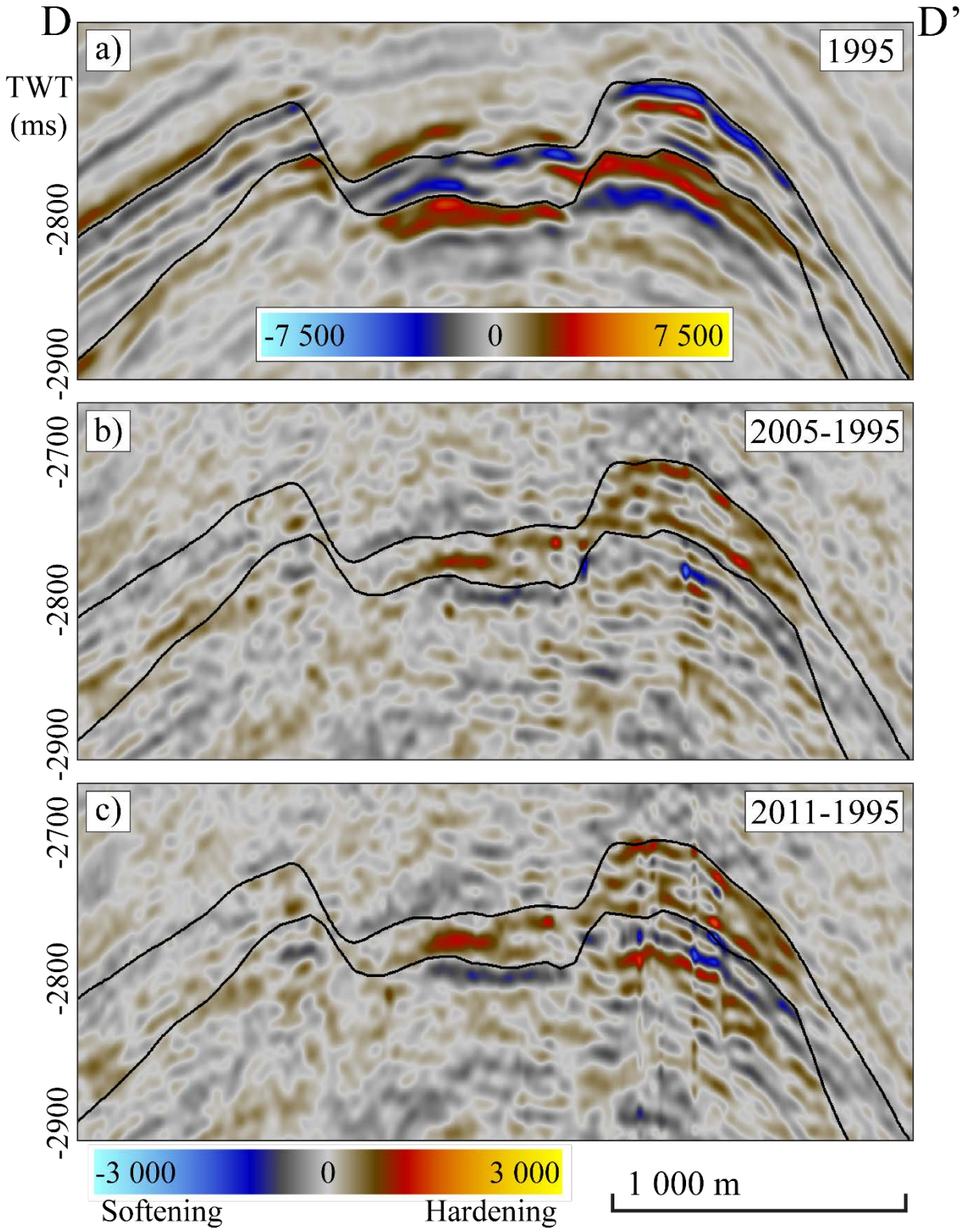


***Figure 6.36**: Seismic section D-D', showing the result of the coloured inversion of the 1995 full stack seismic (a), and difference in coloured inversion between 1995 and 2005 (b) and between 1995 and 2011 (c). The top and base reservoir interpretations (i.e., top Ekofisk and base Tor fms) are displayed in black for reference.*

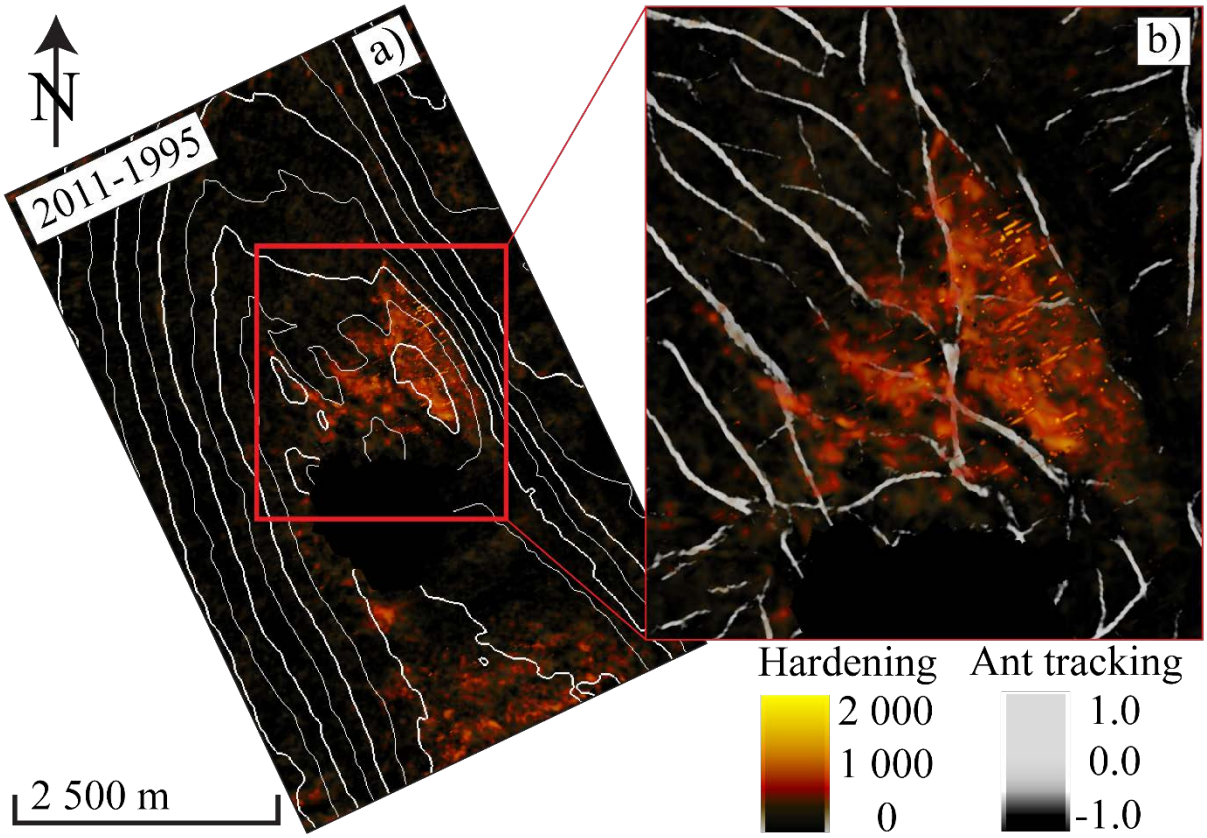


***Figure 6.37**: Horizon probe showing the hardening effect of the reservoir interval, displayed together with contour lines of the top reservoir map (a), and together with the ant tracking map (b).*

As discussed above, it is likely that the hardening effect is mainly caused by compaction and pressure changes, rather than changes in fluid saturation. This is however not in contradiction with the assumption of sealing faults, as the compaction, decrease in pressure, and increase in water saturation probably are linked. This means that the compaction occurs at different degrees across faults, possibly due to differences in depletion of the reservoir segments, as a result of fault sealing.

The hardening effect observed in Figure 6.37 correlates with compaction (Figure 6.22), supporting the interpretation that the coloured inversion differences are mainly sensitive to compaction. This assumption is further investigated by the comparison of the negative time-shift and hardening effect for the main production area in Figure 6.38. Note that the hardening effect is observed to start at the location of an injection well on the ENE flank, whereas the compaction extends deeper down the flank. This is an indication that the coloured inversion differences show changes in fluid saturation. However, the compaction in this area is low in magnitude, and a possible explanation is that a significant amount of compaction is needed in order to be captured by the coloured inversion differences.

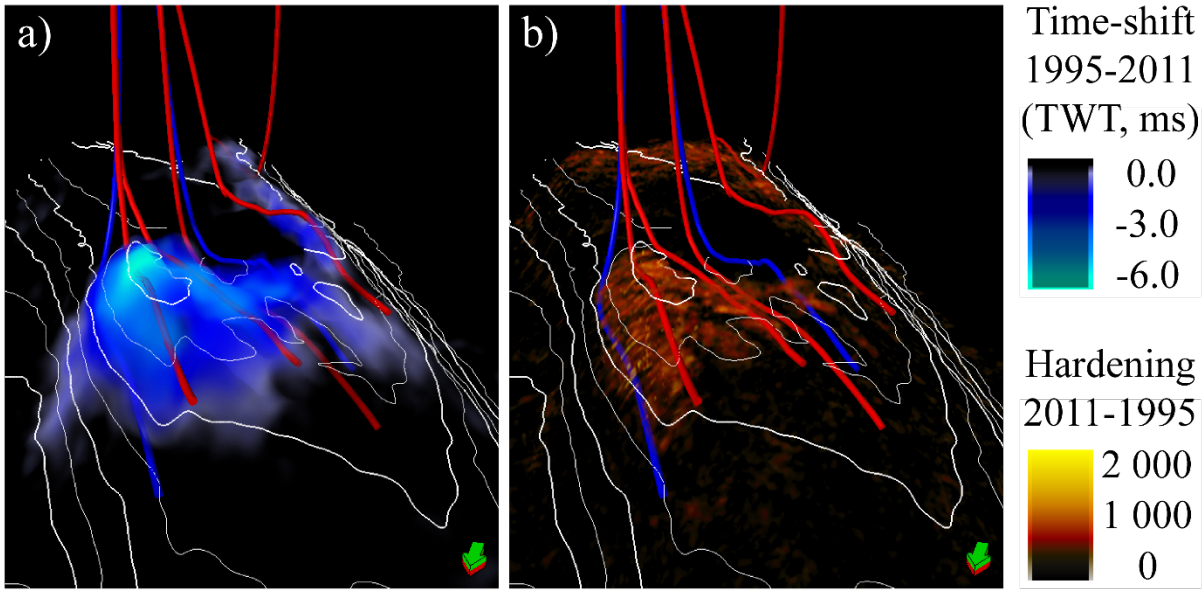


***Figure 6.38**: Horizon probes of the reservoir interval from the 1995-2011 time-shift (a) and the 1995-2011 difference in coloured inversion (b) displayed in 3D. The top reservoir contour lines are displayed for reference, production wells are displayed in red, and injection wells in blue.*

# 7. Discussion and conclusions

In this chapter, the results of this study are further discussed together with previous studies conducted on the field. A summary of the results separated by areas of the anticline is given in Table 7.1. The aim is to bring all the results together, and answer the questions presented in the objectives (i.e., how the reservoir structure is affected by oil production, and how the fluids migrate within the reservoir).

***Table 7.1**: Summary of the results for the different parts of the reservoir on the anticline, separated as the main production area (i.e., just north of the gas cloud), SSE (i.e., to the SSE away from the gas cloud), and NNW (i.e., to the NNW away from the main production area).*

| Property | Main production area | SSE | NNW |
|---|---|---|---|
| Reservoir thickness | Medium | Low | Large |
| Reservoir quality | High | Medium | Low |
| Compaction | Large | No/small | No |
| Fault reactivation | Yes | No | Yes |
| Amplitude anomaly (pre-production) | Yes | Yes | No |
| AVO anomaly (pre-production) | Yes | Yes | No |
| Full stack amplitude changes with time | Yes | No/small | No |
| AVO changes with time | Yes | No/small | No |
| Hardening based on coloured inversion | Yes | No/small | No |

## 7.1 Structural analysis – compaction and fault reactivation

As discussed above, compaction mainly affects an area of the reservoir with high porosities and low water saturation (i.e., the main production area), which results in low stiffness based on the elastic properties of the rocks. Vejbæk et al. (2005) suggested that the high porosities are caused by a combination of early oil invasion and overpressure. This could explain the correlation between water saturation and porosity observed in the well data. It may also explain why the compaction is observed only for the high porosity parts of the reservoir, as the porosity is preserved at a high level due to abnormally high pore pressure. During oil depletion, the pore pressure drops quickly, and the weight of the overburden can no longer be supported by the high porosity reservoir rocks.

The observation that the velocity of the reservoir increases with production time (chapter 6.4.1) is mainly explained by the compaction. However, several factors are affect the seismic velocity, as discussed in chapter 3.3.1. Effects that increase the seismic velocity include increase in water saturation and decrease in pore pressure due to oil extraction, and reduction in porosity caused by the compaction. The interpretation that the velocity increase in the reservoir is mainly attributed to compaction is supported by the correlation between compaction and the velocity increase.

Production-induced fault reactivation is also observed predominantly in the area with high porosities. A possible reason is that the high initial pore pressures in this area, allows fault reactivation more easily than the surrounding areas, where the pre-production pore pressures were probably significantly lower.

Fabricius et al. (2007) suggest that the difference in porosity between the wells Rigs-1 and Rigs-2 is a result of differences in pore-filling calcite cement (i.e., larger amount of calcite cement in Rigs-1 than Rigs-2), caused by chemical compaction. This suggests that the low-porosity zones of the reservoir contain larger volumes of pore-filling calcite cement, whereas this cementation does not occur to the same degree in the high-porosity zones. They also found that the two wells penetrate chalks containing clay minerals. Fabricius et al. (2008) suggest that porosity-preserving cementation has occurred for the high-porosity chalks of the South Arne field, and that the high porosities may be caused by hydrocarbons preventing chemical compaction. These results might indicate that the porosity-preserving cementation is formed by clay minerals, which could explain why high shale content is observed for the chalks yielding the highest porosity (i.e., the positive correlation between gamma ray values and porosity).

The interpretation of Fabricius et al. (2008) that hydrocarbons prevent chemical compaction, might indicate that the production-induced compaction discussed in this study is mainly a result of chemical compaction caused by increase in water saturation, rather than decrease in pore pressure. However, due to the discussed indications of high initial pore pressures, and the observation of fault reactivation, the decrease in pore pressure with production is likely to be the main effect causing the compaction. This is supported by the fact that no water flooding is observed in the seismic data, as interpreted from the difference in coloured inversion.

## 7.2 Fluid movements

The interpretation of changes in amplitudes, AVO effects, and coloured inversion forms the basis for analysing fluid movements within the reservoir. The main complicating factor in terms of identifying changes in fluid contacts in this study is to separate between changes in seismic response caused by compaction and by fluid saturation. Observations supporting the different interpretations are summarized in Table 7.2, in order to identify the main contributor to changes in seismic amplitudes, AVO, and coloured inversion.

As already discussed, the main observation indicating that the seismic responses are mostly sensitive to compaction, is the good correlation between these two effects. This is supported by the rock physics study, showing that acoustic impedance is more sensitive to porosity than water saturation. In addition, no identification of changes in oil-water contact is possible based on changes in coloured inversion, as the hardening effect is uniformly distributed within the reservoir.

On the other hand, the changes in seismic responses follow contour lines, which is probably the strongest indication that changes in fluid saturation are captured by the seismic data. In addition, the hardening effect of the main production area, obtained from difference in coloured inversion, start at the location of an injection well, indicating that this could also be the results of increase in water saturation.

The hardening of the reservoir is probably reflecting a combination of the two effects, in addition to the decrease in pressure. As discussed above, the high porosities of the reservoir rocks of the main production area are partly caused by early hydrocarbon invasion, which has resulted in this area having high oil saturation. This shows that the rocks mostly susceptible to production-induced compaction by decreased pressure (i.e., the high-porosity reservoir rocks) are also the rocks that has the largest potential for increase in water saturation during production.

That being said, the main fluid movements observed and interpreted, are influenced by partly sealing faults. This interpretation is based on different degrees of hardening effect observed on different sides of several faults in the main production area. Most likely, this is a result of reservoir compartmentalization, allowing the separated reservoir blocks to be depleted at different rates. This may also explain the different rates of compaction across several faults (i.e., fault reactivation), as the pressure drops differently based on the depletion rates.

***Table 7.2**: Separation of fluid effects and compaction based on changes in amplitudes, AVO response, and coloured inversion from different observations.*

| Observation | Indication |
|---|---|
| AI correlates better with porosity than water saturation | Compaction |
| Amplitude/AVO/coloured inversion changes correlate with compaction | Compaction |
| Amplitude/AVO/coloured inversion changes follow contour lines | Fluid |
| No identification of water flooding | Compaction |
| Inconsistent amplitude changes across faults | Compaction/fluid |
| Hardening effect in the main production area starts at an injector | Fluid |

## 7.3 Recommendations for future work

Based on the work of this study, there are some possibilities for further work in order to better understand the time dependent signal of the field:

- Better understanding of the observed AVO effects and what they actually show.
- Distinction between changes in saturation, pressure, and compaction based on time-lapse AVO inversion.
- Calibration of the time-lapse seismic results to production data.

# References


Aki, K., and Richards, P. G., 1980, Quantitative seismology, W. H. Freeman.

Andsbjerg, J., and Dybkjaer, K., 2003, Sequence stratigraphy of the Jurassic of the Danish Central Graben: Geological Survey of Denmark and Greenland Bulletin, v. 1, p. 265-230.

Astratti, D., Aarre, V., Vejbæk, O. V., and White, G., 2014, Mapping and time-lapse analysis of South Arne Chalk fault network using new developments in seismic dip computation: Geological Society, London, Special Publications, v. 406, p. 331-358.

Booth, A. D., Emir, E., and Diez, A., 2016, Approximations to seismic AVA responses: Validity and potential in glaciological applications: Geophysics, v. 81, no. 1, p. WA1-WA11.

Castagna, J. P., and Swan, H. W., 1997, Principles of AVO crossplotting: The Leading Edge, v. 16, no. 4, p. 337-342.

Chan, A. W., and Zoback, M. D., 2002, Deformation Analysis in Reservoir Space (DARS): A Simple Formalism for Prediction of Reservoir Deformation With Depletion, SPE/ISRM Rock Mechanics Conference.

Christensen, S. A., Dalgaard, T. E., Rosendal, A., Christensen, J. W., Robinson, G., Zellou, A. M., and Royer, T., 2006, Seismically Driven Reservoir Characterization Using an Innovative Integrated Approach: Syd Arne Field, SPE Annual Technical Conference and Exhibition: San Antonio, Texas, United States of America, Society of Petroleum Engineers.

Clausen, O. R., Korstgård, J. A., and Egebjerg, T. M., 1996, Quantitative strain analysis of strike-slip displacements across the Arne-Elin trend, the Danish Central Graben: Bulletin of the Geological Society of Denmark, v. 43, p. 99-113.

David, E. C., and Zimmermann, R. W., 2012, Pore structure model for elastic wave velocities in fluid-saturated sandstones: Journal of Geophysical Research, v. 117, no. B7.

Domenico, S. N., 1974, Effect of water saturation on seismic reflectivity of sand reservoirs encased in shale: Geophysics, v. 39, no. 6, p. 68-86.

Fabricius, I. L., Gommesen, L., Krogsboll, A., and Olsen, D., 2008, Chalk porosity and sonic velocity versus burial depth: Influence of fluid pressure, hydrocarbons, and mineralogy: AAPG Bulletin, v. 92, no. 2, p. 201-223.

Fabricius, I. L., Høier, C., Japsen, P., and Korsbech, U., 2007, Modelling elastic properties of impure chalk from South Arne Field, North Sea: Geophysical Prospecting, v. 55, no. 4, p. 487-506.

Fatti, J. L., Smith, G. C., Vail, P. J., Strauss, P. J., and Levitt, P. R., 1994, Detection of gas in sandstone reservoirs using AVO analysis: A 3-D seismic case history using the Geostack technique: Geophysics, v. 59, no. 9, p. 1362-1376.

Fossen, H., 2010, Structural Geology, Cambridge Unversity Press.

Garcia, A., and MacBeth, C., 2013, An estimation method for effective stress changes in a reservoir from 4D seismics data: Geophysical Prospecting, v. 61, no. 4, p. 803-816.

Guilbot, J., and Smith, B., 2002, 4-D constrained depth conversion for reservoir compaction estimation: Application to Ekofisk Field: The Leading Edge, v. 21, no. 3, p. 302-308.

Halland, E. K., Gjeldvik, I. T., Johansen, W. T., Magnus, C., Meling, I. M., Pedersen, S., Riis, F., Solbakk, T., and Tappel, I., 2011, $CO_2$ Storage Atlas, Norwegian North Sea.

Hamilton, E. L., 1956, Low Sound Velocity in High-Porosity Sediments: The Journal of the Acoustical Society of America, v. 28, no. 1.

Han, D., Nur, A., and Morgan, D., 1986, Effects of porosity and clay contenton on wave velocities in sandstones: Geophysics, v. 51, no. 11, p. 2093-2107.

Hatchell, P. J., and Bourne, S. J., 2005, Measuring reservoir compaction using time-lapse timeshifts SEG Technical Program Expanded Abstracts, p. 2500-2503.

Hatchell, P. J., Kawar, R. S., and Savitski, A. A., 2005, Integrating 4D seismic, geomechanics and reservoir simulation in the Valhall oil field, EAGE 67th Conference and Exhibition.

Herwanger, J. V., Schiøtt, C. R., Frederiksen, R., Vejbæk, O. V., Wold, R., Hansen, H. J., Palmer, E., and Koutsabeloulis, N., 2010, Applying time-lapse seismic to reservoir management and field development planning at South Arne, Danish North Sea, Lodnon, United Kingdom, Geological Society, Petroleum Geology: From Mature Basins to New Frontiers – Proceedings of the 7th Petroleum Geology Conference.

Hicks, W. G., and Berry, J. E., 1956, Application of continuous velocity logs in determination of fluid saturation of reservoir rocks: Geophysics, v. 21, no. 3, p. 739-754.

Japsen, P., Bruun, A., Fabricius, I. L., and Mavko, G., 2005, Identification of hydrocarbons in chalk reservoirs from surface seismic data: South Arne field, North Sea: Geological Survey of Denmark and Greenland Bulletin, v. 7, p. 13-16.

Japsen, P., Bruun, A., Fabricius, I. L., Rasmussen, R., Vejbæk, O. V., Pedersen, J. M., Mavko, G., Mogensen, C., and Høier, C., 2004, Influence of porosity and pore fluid on acoustic properties of chalk: AVO response from oil, South Arne Field, North Sea: Petroleum Geoscience, v. 10, no. 4, p. 319-330.

Korstgård, J. A., Lerche, I., Mogensen, T. E., and Thomsen, R. O., 1993, Salt and fault interactions in the northeastern Danish Central Graben: observations and inferences Bulletin of the Geological Society of Denmark, v. 40, p. 197-255.

Lancaster, S., and Whitcombe, D., 2000, Fast-track 'coloured' inversion, SEG Technical Program Expanded Abstracts 2000, Society of Exploration Geophysicists, p. 1572-1575.

Landrø, M., 2015, 4D Seismic, *in* Bjørlykke, K., ed., Petroleum Geoscience: From Sedimentary Environments to Rock Physics, p. 489-514.

Landrø, M., and Stammeijer, J., 2004, Quantitative estimation of compaction and velocity changes using 4D impedance and traveltime changes: Geophysics, v. 69, no. 4, p. 949-956.

Lindgreen, H., Fallick, A. E., Jakobsen, F., and Springer, N., 2012, The Tight Danian Ekofisk Chalk Reservoir Formation in the South Arne Field, North Sea: Mineralogy and Porosity Properties: Journal of Petroleum Geology, v. 35, no. 3, p. 291-309.

Lüthje, M., Stokkendal, J., Lindelow-Marsden, C. C., Johansen, K., and Jensen, L. J. K., 2013, Using 4D Seismic to Validate the Geomodel for the South Arne Chalk Field, SPE Reservoir Characterization and Simulation Conference and Exhibition: Abu Dhabi, United Arab Emirates, Society of Petroleum Engineers.

Mackertich, D. S., and Goulding, D. R. G., 1999, Exploration and appraisal of the South Arne Field, Danish North Sea: Geological Society, London, Petroleum Geology Conference series, v. 5, p. 959-974.

Marion, D. P., 1990, Acoustical, mechanical, and transport properties of sediments and granular materials [PhD: Stanford University.

Møller, J. J., and Rasmussen, E. S., 2003, Middle Jurassic – Early Cretaceous rifting of the Danish Central Graben: Geological Survey of Denmark and Greenland Bulletin, v. 1, p. 247-264.

Nickel, M., and Sønneland, L., 1999, Non-rigid matching of migrated time-lapse seismic: SEG Technical Program Expanded Abstracts, p. 872-875.

Rutherford, S. R., and Williams, R. H., 1989, Amplitude-versus-offset variations in gas sands: Geophysics, v. 54, no. 6, p. 680-688.

Røste, T., Stovas, A., and Landrø, M., 2005, Estimation of layer thickness and velocity changes using 4D prestack seismic data, EAGE 67th Annual Conference and Exhibition.
Settari, A., 2002, Reservoir Compaction: Society of Petroleum Engineers.
Sheriff, R. E., and Geldart, L. P., 1995, Exploration Seismology, Cambridge University Press.
Shuey, R. T., 1985, A simplification of the Zoeppritz equations: Geophysics, v. 50, no. 4, p. 609-614.
Simm, R., and Bacon, M., 2014, Seismic Amplitude: An Interpreter's Handbook, Cambridge University Press.
Smith, G. C., and Gidlow, P. M., 1987, Weighted stacking for rock property estimation and detection of gas: Geophysical Prospecting, v. 35, no. 9, p. 993-1014.
Staples, R., Brain, J., Hunt, K., Behrens, M., Charreyron, Y., and Cook, A., 2007, 4D Driving Developments at Gannet E & F, 69th EAGE Conference and Exhibition incorporating SPE EUROPEC 2007.
Streit, J. E., and Hillis, R. R., 2002, Estimating Fluid Pressures That Can Induce Reservoir Failure During hydrocarbon Depletion: Society of Petroleum Engineers.
Tosaya, C., Nur, A., Vo-Thanh, D., and Prat, G. D., 1987, Laboratory Seismic Methods for Remote Monitoring of Thermal EOR SPE Reservoir Engineering, v. 2, no. 2, p. 235-242.
Vejbæk, O. V., Rasmussen, R., Japsen, P., Bruun, A., Pedersen, J. M., Marsden, G., and Fabricius, I. L., 2005, Modelling seismic response from North Sea chalk reservoirs resulting from changes in burial depth and fluid saturation, London, United Kingdom, Geological Society, Petroleum Geology: North-West Europe and Global Perspectives—Proceedings of the 6th Petroleum Geology Conference.
Wang, Y., 1999, Approximations to the Zoeppritz equations and their use in AVO analysis: Geophysics, v. 64, no. 6, p. 1920-1927.
Wang, Z., and Nur, A., 1988, Effect of Temperature on Wave Velocities in Sands and Sandstones With Heavy Hydrocarbons: SPE Reservoir Engineering, v. 3, no. 1, p. 158-164.
Yin, H., Han, D. H., and Nur, A., 1988, Study of velocity and compaction on sand-clay mixtures: Stanford Rock and Borehole Project, v. 33.
Ziegler, P. A., 1975, The Geological Evolution of the North Sea Area in the Tectonic Framework of North Western Europe: Norges Geol Unders, v. 316, p. 1-27.
Zoback, M. D., and Zinke, J. C., 2002, Production-induced Normal Faulting in the Valhall and Ekofisk Oil Fields: Pure and Applied Geophysics, v. 159, no. 1-3, p. 403-420.
Zoeppritz, K., 1919, VII b. Über Reflexion und Durchgang seismischer Wellen durch Unstetigkeitsflächen: Nachrichten von der Gesellschaft der Wissenschaften zu Göttingen, Mathematisch-Physikalische Klasse, v. 1919, p. 66-84.
Ødegaard, E., and Avseth, P., 2004, Well log and seismic data analysis using rock physics templates: First Break, v. 22, no. 10, p. 37-43.